

Electrochemical Impedance Spectroscopy using Adjustable Nanometer-Gap Electrodes

by

Hongshen Ma

Bachelor of Applied Science in Engineering Physics
University of British Columbia, 2001

Master of Science in Media Arts and Sciences
Massachusetts Institute of Technology, 2004

Submitted to the Department of Electrical Engineering and Computer Science in Partial
Fulfillment of the Requirements for the Degree of
Doctor of Philosophy in Electrical Engineering and Computer Science

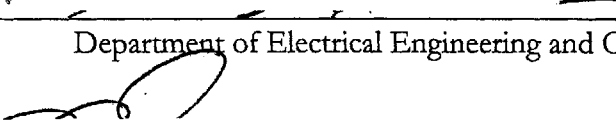
at the

MASSACHUSETTS INSTITUTE OF TECHNOLOGY

September 2007

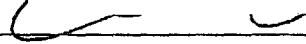
© 2007 Massachusetts Institute of Technology. All rights reserved.

Signature of Author

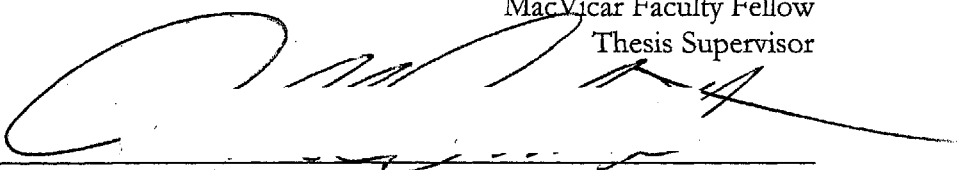

Department of Electrical Engineering and Computer Science

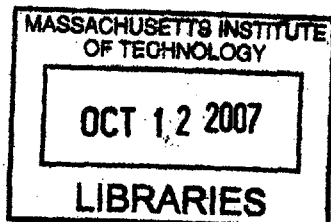
August 31, 2007

Certified by


Alexander H. Slocum, Ph.D.
Neil and Jane Pappalardo Professor of Mechanical Engineering
MacVicar Faculty Fellow
Thesis Supervisor

Accepted by


Arthur C. Smith, Ph.D.
Chairman, Committee on Graduate Students
Department of Electrical Engineering and Computer Science



ARCHIVES

Electrochemical Impedance Spectroscopy using Adjustable Nanometer-Gap Electrodes

by

Hongshen Ma

Submitted to the Department of Electrical Engineering and Computer Science
on August 15, 2007, in partial fulfillment of the
requirements for the degree of
Doctor of Philosophy

Abstract

Electrochemical Impedance Spectroscopy (EIS) is a simple yet powerful chemical analysis technique for measuring the electrical permittivity and conductivity of liquids and gases. Presently, the limiting factor for using EIS as a portable chemical detection technology is the lack of absolute accuracy stemming from uncertainties in the geometrical factor used to convert measurable quantities of capacitance and conductance into the intrinsic parameters of permittivity and conductivity. The value of this geometrical conversion factor can be difficult to predict since it is easily affected by fringing electric fields, manufacturing variations, and surface chemistry. Existing impedance test cells typically address this problem using a calibration liquid with known permittivity and conductivity, however, this correction is not feasible in many applications since the calibration liquid may irreversibly contaminate the test electrodes.

This thesis presents a technique for accurately measuring the permittivity and conductivity of liquids and gases without requiring the use of calibration liquids. This technique is made possible by precisely controlling the separation between two spherical electrodes to measure capacitance and conductance of the sample medium as a function of electrode separation. By leveraging the geometrical accuracy of the spherical electrodes and precise control of the electrode separation, the permittivity and conductivity of the sample can be determined without wet calibration. The electrode separation is adjusted using a flexure stage and a servomechanical actuator, which enables control the electrode separation with 0.25 nm resolution over a range of 50 μm . The nanometer smooth surfaces of the spherical electrodes also enable electrode gaps of less than 20 nm to be created.

The technique for measuring permittivity and conductivity presented in this thesis could eventually be adapted to make miniaturized disposable impedance test cells for chemical analysis. Such systems could take advantage of conductivity assays to determine the presence and concentration of specific substances. The adjustable nanometer electrode gap can also be used to study the properties of chemical and biological systems in highly confined states. These studies are fundamentally important for understanding biochemical processes in natural systems where reactions often take place inside confined structures such as cells, organelles, and the intercellular matrix.

Thesis Supervisor: Alexander H. Slocum

Title: Neil and Jane Pappalardo Professor of Mechanical Engineering, MacVicar Faculty Fellow

Acknowledgements

The work presented in this thesis could not have been possible without the help of many people. First and foremost, I would like to thank my research advisor Alex Slocum for giving me both the freedom and the support to pursue this project. Thank you so much for always being positive and always believing in me. The level of enthusiasm and creativity that you bring to a project is truly infectious and I hope to do the same in my own work in the future. In addition to being a great advisor, I want to thank you for being a great friend and for always reminding me to have fun, that 100 mile bike ride to Lake Winnepesaukee is one of my favorite memories.

I would like to thank my thesis committee members, Profs. Jeff Lang, Alan Grodzinsky, and Don Sadoway, for mentoring me through this process. I want to especially acknowledge Jeff for meeting with me many times in the last year. These meetings were pivotal for keeping me on track and for moving this research forward.

The two people that have been vital in the design and fabrication of the apparatuses developed in this thesis are Kurt Broderick of Microsystems Technology Laboratory and Mark Belanger of the Edgerton Student Machine Shop. There were many times when problems that required weeks of work would be reduced to one or two days because of the resourcefulness and ingenuity of Kurt and Mark. To you I am deeply indebted.

I would like to thank Prof. George Verghese for his enthusiastic help with the data analysis; Prof. David Trumper for early discussions on the design of the mechanism; and my master's advisor, Prof. Joe Paradiso for first introducing me to the subject of sensors and electronics.

I would like to thank Dr. James White for initially introducing me to the Nanogate project and MEMS research.

I would like to thank Dr. Ari Benbasat for working with me on my thesis and presentation.

I would like to thank Maureen Lynch for helping me with many things, both administrative and personal, as well as for being a great friend and a hilarious officemate.

I would like to thank the tremendous group of undergraduates that I have had the pleasure to work with: Wey-Jiun Lin, Ed Summers, Shane Colton, and Melanie Hoehl. I am proud of your accomplishments and thankful for the wonderful enthusiasm that you brought to your work.

I would like to thank my fellow members of the Precision Engineering Research Group: John Hart, Alexis Webber, Onnik Yaglioglu, Zachary Trimble, Nevan Hanumara,

and many others whom were always willing to help me with my experiment and inspired me to work hard with their wonderful work.

I would like to thank the Center for Bits and Atoms at MIT, the Cambridge-MIT Institute, and the National Science and Engineering Research Council of Canada for their financial support.

I would like to thank my many friends at MIT and elsewhere for making the last few years wonderful in so many ways. From fun times at the GSC ski trip, to driving a moped around Oahu, to paddling a raft up the Charles for the 4th, to roaming around the underbelly of New York City during Midnight Madness – these are the memories of a lifetime.

Finally, and most importantly, I would like to thank my girlfriend, Kaity Ryan, and my mom and dad, Shufen Hou and Yilun Ma, for their wonderful love and support, without which, none of this would have been possible.

Contents

Abstract	3
Acknowledgements	5
Contents	7
List of Figures	9
List of Tables	13
Nomenclature and Abbreviations	15
1. Introduction	17
1.1 Introduction.....	17
1.2 Case Study: The Diethylene Glycol Poisoning Tragedy	20
1.3 Electrochemical Impedance Spectroscopy and Its Challenges	21
1.4 Current Miniaturized Impedance Test Cells	24
1.5 Permittivity and Conductivity Measurements without Wet Calibration.....	26
1.6 Optimization of Impedance Test Cells with Adjustable Cell Constant	28
1.7 Electrical Measurements across Electrodes Separated by Nanometer Gaps	29
1.8 Thesis Outline	31
2. Design	35
2.1 Impedance Test Cell	35
2.1.1 Electrode	35
2.1.2 Electrode Mounting Shaft.....	38
2.1.3 Sample Chamber	39
2.2 Positioning Mechanism.....	40
2.2.1 General Orientation.....	40
2.2.2 Coarse Adjustor	41
2.2.3 Fine Adjustor	43
2.2.4 Metrology Frame	45
2.2.5 Mechanism Evaluation and Error Analysis	45
2.3 Instrumentation	48
2.3.1 Impedance Measurement	48
2.3.2 Temperature Control System	50
2.3.3 Data Acquisition System.....	51
3. Modeling	55
3.1 Electrostatic Model	55
3.1.1 Capacitance and Conductance between Spheres	55
3.1.2 Errors due to Electrode Geometry	57
3.1.3 Errors due to Mechanical Alignment.....	58
3.2 Electrochemical Model	61
3.2.1 The Gouy-Chapman-Stern Model.....	61

3.2.2	Equivalent Circuit Model.....	64
3.2.3	Interpretation of the Measured Impedance	69
4.	Analysis	75
4.1	Simple Least Squares Fitting	75
4.2	Weighted Least Squares (WLS) Fitting.....	79
4.3	Non-Linear (NL1) Fitting	85
4.4	Errors Caused by the Electrode Mounting Shaft	87
4.5	Sensitivity to Noise	91
4.5.1	Sensitivity to Capacitance Noise	91
4.5.2	Sensitivity to Electrode Position Noise.....	93
4.5.3	Comparison of Noise Sensitivity	96
4.6	Summary of Data Analysis Techniques.....	97
5.	Results	99
5.1	Permittivity of Nitrogen Gas.....	100
5.2	Permittivity of Methanol.....	109
5.3	Additional Permittivity Measurements	117
5.4	Conductivity of Potassium Chloride Solutions.....	119
5.5	Frequency Dependence Measurements.....	127
5.6	Nanometer Electrode Gaps in Air.....	133
5.6.1	Measurement of Nanometer Electrode Gaps in Air.....	134
5.6.2	Surface Roughness Model	137
6.	Conclusions and Future Directions	143
6.1	Contributions.....	143
6.2	Implications and Future Directions.....	146
	References	151
	Appendix A: Mechanical Drawings	155
	Appendix B: MATLAB Code	165
	Appendix C: Visual Basic Code.....	175

List of Figures

Figure 1.1: Design of a microfabricated impedance test cell based on interdigitated electrodes.	25
Figure 1.2: Design of a microfabricated impedance test cell based on oxide etching.	25
Figure 1.3: Photograph of Wu’s apparatus developed at NIST [16] for measuring the absolute specific conductivity of KCl solutions.	27
Figure 1.4: Illustration of the apparatus developed by Shiefelbien [10].	27
Figure 2.1: Photograph of silicon-nitride spheres (Source: Cerbec Saint-Gobain Ceramics).	36
Figure 2.2: Surface profile of a silicon-nitride sphere. Surface roughness $R_a \approx 2$ nm; peak-to-valley ≈ 50 nm.	37
Figure 2.3: Surface profile of a polished silicon wafer. Surface roughness $R_a \approx 1$ nm; peak-to-valley ≈ 20 nm.	37
Figure 2.4: Surface profile of a silicon-nitride sphere with a 5 nm chrome layer and a 50 nm platinum layer. Surface roughness $R_a \approx 2$ nm; peak-to-valley ≈ 50 nm.	37
Figure 2.5: Cross section of the impedance test cell.	39
Figure 2.6: Impedance test cell with capacitance probes and target electrodes.	39
Figure 2.7: Overview of the positioning mechanism.	41
Figure 2.8: Detail of the flexure mechanism design including coarse actuator, capacitance probe, and clamps for constraining the electrode mounting shaft.	42
Figure 2.9: Measurement of the transmission ratio from the servomechanical actuator and the top electrode.	46
Figure 2.10: Parasitic displacement along the y- and z-axes and the frame distortion measured by the bottom probe. Parasitic displacement along the y-axis is attenuated by the wobble pin.	47
Figure 2.11: Simplified circuit diagram of the auto-balancing bridge technique used in the Agilent 4284A LCR meter [41].	49
Figure 2.12: Electrical connection of the electrodes and sample chamber.	49
Figure 2.13: Picture of the flexure and actuator with the radiator system inside the thermal isolation chamber.	51
Figure 2.14: Schematic of the data acquisition system.	52
Figure 2.15: Screenshot of the Visual Basic .NET 2005 program used to control the entire experiment.	53
Figure 3.1: Electrostatic model of two spheres.	56

Figure 3.2: Electrode profiles and field lines modified by the mounting shaft.	58
Figure 3.3: Lateral alignment error.	59
Figure 3.4: Angular alignment error.	60
Figure 3.5: Equivalent circuit of a uniformly polarizable interelectrode medium.....	61
Figure 3.6: Gouy-Chapman-Stern model of the electrode-electrolyte interface.....	64
Figure 3.7: Equivalent circuit of the combined bulk and interfacial model.	65
Figure 3.8: Bode plot for the combined bulk and interfacial model.....	68
Figure 4.1: Simulated data set of $C(x)$	76
Figure 4.2: Transformed data set of $y(x)$ where ϵ_r can be determined from the inverse of the slope.	78
Figure 4.3: Simple and weighted least squares fitting on noisy data. C_e is distributed uniformly with an amplitude of 5×10^{-16} F.....	83
Figure 4.4: Weighted residue plot from weighted least squares fitting.	83
Figure 4.5: Variation of RMS fit error as a function of x_0 for simulated noiseless data. .	86
Figure 4.6: Least squares fitting to the transformed domain using simulated, noiseless data.	87
Figure 4.7: WLS analysis of simulated noiseless data with errors caused by the electrode mounting shaft.	89
Figure 4.8: Residue from WLS fitting of simulated noiseless data with errors caused by the electrode mounting shaft.	90
Figure 4.9: NL1 analysis of simulated noiseless data with errors caused by the electrode mounting shaft.	90
Figure 4.10: The value of ϵ_r as a function of data range determined using WLS and NL1 analysis.....	91
Figure 4.11: Determination the relative permittivity using WLS and NL1 techniques from 40 sets of simulated noisy impedance data. Noise on the impedance data is simulated as a normal distribution where $\sigma_C = 3 \times 10^{-16}$ F. The range of the simulated data is $15 \mu\text{m}$ collected in steps of $0.5 \mu\text{m}$	92
Figure 4.12: Estimated standard deviation of the previous relative permittivity measurements by WLS and NL1 techniques.	93
Figure 4.13: Determination of the relative permittivity using WLS and NL1 techniques from 40 sets of simulated noisy data. Noise on the electrode position, x , is simulated as a normal distribution with zero mean and $\sigma_x = 2 \text{ nm}$. No noise is assumed on the capacitance measurement.....	95
Figure 4.14: The estimated standard deviation of each simulated data set. Noise on the electrode position, x , is simulated as a normal distribution with zero mean and $\sigma_x = 2 \text{ nm}$. No noise is assumed on the capacitance measurement.	95

Figure 4.15: Standard deviation of ϵ_r from 40 data sets with simulated capacitance noise. The capacitance noise is normally distributed with standard deviation, σ_C plotted along the x-axis.....	96
Figure 4.16: Standard deviation of ϵ_r from 40 data sets with simulated electrode position noise. The position noise is normally distributed with standard deviation, σ_C plotted along the x-axis.....	97
Figure 5.1: Resistance versus electrode position in nitrogen gas.	102
Figure 5.2: Capacitance versus electrode position in nitrogen gas.....	102
Figure 5.3: Permittivity of nitrogen gas analyzed using WLS analysis.....	104
Figure 5.4: Relative permittivity determined by WLS versus data range from measured data for nitrogen gas.....	104
Figure 5.5: Weighted residue from the permittivity of nitrogen gas measurement.	105
Figure 5.6: Permittivity of nitrogen gas measurement analyzed using NL1. Data points from smaller electrode gaps that are not used for fitting are located beyond the top right boundaries of the graph. These data points have been omitted for clarity.	106
Figure 5.7: Optimization for x_0 using the RMS fitting error for NL1 analysis of nitrogen gas data.....	106
Figure 5.8: Permittivity of nitrogen gas from repeated measurements determined using both WLS and NL1 analysis.	108
Figure 5.9: Zoomed view of Figure 5.3 show the behavior at small electrode gaps.	108
Figure 5.10: Example resistance versus electrode position plot for methanol.	112
Figure 5.11: Example capacitance versus electrode position plot for methanol.....	113
Figure 5.12: The relative permittivity of 99.9% pure methanol measured at 15.4°C and 120 kHz. The relative permittivity has been determined using WLS analysis.....	113
Figure 5.13: Relative permittivity determined by WLS versus data range from measured data for methanol.	114
Figure 5.14: Relative permittivity of 99.9% pure methanol at 15.4°C and 120 kHz from repeated measurements determined using WLS analysis.	115
Figure 5.15: Measured relative permittivity from repeated experiments analyzed using WLS with -1% correction.	116
Figure 5.16: Measured relative permittivity from repeated experiments analyzed using NL1.	116
Figure 5.17: Repeated measurements of the relative permittivity of 2-propanol at 17.6°C.	117
Figure 5.18: The permittivity of 2-propanol as a function of temperature after compensation.	118
Figure 5.19: Repeated measurements of the permittivity of 0.1 mM KCl solution at 18.0°C.	118

Figure 5.20: Temperature dependence of the permittivity of 0.1 mM KCl solution after compensation.	119
Figure 5.21: An example resistance versus electrode position plot from 10 mM KCl solutions.	122
Figure 5.22: An example capacitance versus electrode position plot from 10mM KCl solutions.	122
Figure 5.23: An example dataset from conductivity measurements using WLS analysis.	124
Figure 5.24: Results from conductivity of 10mM KCl solutions at 11.4 °C from repeated 20 times; κ determined using WLS analysis.	124
Figure 5.25: Conductivity versus temperature for 10 mM KCl solutions. The data points indicated by squares is measured after the chamber had previous been used to measure lower molarity solutions. The data points indicated by diamonds is measured on a newly assembled impedance test cell.	126
Figure 5.26: Arrhenius plot for 10 mM KCl solutions.	127
Figure 5.27: Relative permittivity measurements of 0.1 mM KCl solution at 240, 24, and 7 kHz.	129
Figure 5.28: Conductivity measurements of 0.1 mM KCl solution at 240, 7, and 1.5 kHz.	130
Figure 5.29: Relative permittivity spectra of 0.1 mM KCl solution.	130
Figure 5.30: Conductivity spectra of 0.1 mM KCl solution.	131
Figure 5.31: Theoretical Nyquist diagram of the equivalent circuit in Figure 3.7.	132
Figure 5.32: Experimental Nyquist diagram of 1 mM KCl solution.	132
Figure 5.33: Experimental Nyquist diagram of 0.1 mM KCl solution.	133
Figure 5.34: Tolerable versus problem defects.	135
Figure 5.35: Nanometer electrode gaps measured in air. The deviation from the fitting line between 20 and 40 nm could be explained by surface roughness. The deviation from the fitting line below 20 nm is likely a result of surface-bound water.	136
Figure 5.36: Small gap measurements repeated using several different excitation voltages, showing that the measured electrode gap is independent of excitation voltage.	137
Figure 5.37: Distribution function used to formulate the surface roughness model.	138
Figure 5.38: The surface roughness model superimposed on to the small electrode gap data from Figure 5.35.	141
Figure 6.1: A possible design of an injection-molded impedance test cell.	147
Figure 6.2: Preliminary results (from Melanie Hoehl) of a conductivity assay developed to detect diethylene glycol.	148
Figure 6.3: Illustration of the experiment for measuring nanoparticle mobility in gap.	149

List of Tables

Table 1.1: Comparison of common chemical analysis technique with approximate price and volume of existing instruments and challenges in developing an equivalent miniaturized or portable system.....	18
Table 5.1: Constants used in equation (5.1) for predicting the relative permittivity of pure methanol.....	109
Table 5.2: Constants used in equation (5.3) for predicting the conductivity of KCl solutions.	120
Table 5.3: Conductivities for various concentrations of KCl calculated using equation (5.3).	120

Nomenclature and Abbreviations

C	Measured capacitance
C_0	Constant term from the capacitance between two closely spaced spheres
C_1	Capacitance error due to electrode geometry
C_E	Simulated error term
C_p	Capacitance of the electrode-electrolyte interface
C_s	Capacitance of the bulk liquid
G	Measured conductance (inverse of R)
r	Sphere radius
R	Measured resistance (inverse of G)
R_p	Resistance of the electrode-electrolyte interface
R_s	Resistance of the bulk liquid
S_e	Standard error
S_{xx}, S_{xy}, S_{yy}	Standard statistical parameters
x	Displacement of the sphere
x_0	Offset distance between x and ξ
y	Transformed variable according to equation (4.7), proportional to $\frac{dx}{dC}$ or $\frac{dx}{dG}$
y and z in Chapter 2	Parasitic displacement perpendicular to x
z	Probabilistic model of surface roughness
Z	Measured impedance
ϵ_0	Vacuum permittivity
ϵ_r	Relative permittivity

κ	Conductivity
κ_0	Conductivity factor used in the Arrhenius equation
ζ	Distance measured between the nearest points from two spheres
σ	Standard deviation
ω	Frequency of the excitation signal
AFM	Atomic force microscope
DEG	Diethylene glycol
EIS	Electrochemical impedance spectroscopy
GCS	Gouy-Chapman-Stern model
KCl	Potassium chloride
NL1	Non-linear fitting used to determined relative permittivity and conductivity from capacitance and conductance
STM	Scanning tunneling microscope
WLS	Weighted least squares fitting used to determine relative permittivity and conductivity from capacitance and conductance

Chapter 1

Introduction

1.1 Introduction

Miniaturized chemical analysis systems, sometimes known as Micro Total Analysis Systems or Lab-on-a-Chip, aim to reduce the size of the apparatuses required for performing chemical and biological analyses in order to reduce cost, increase speed, and improve accessibility of specialized laboratory techniques. These devices include both on-chip analysis systems fabricated using semiconductor manufacturing techniques, as well as, small portable devices fabricated using traditional manufacturing techniques. The development of these devices could benefit a wide range of areas. In chemical analysis and environmental monitoring applications, inexpensive portable device can provide real-time analysis and eliminate the need to ship samples for testing in external laboratories. Medical research and drug discovery can take advantage of the small sample volume and high throughput capabilities of miniaturized systems in order to perform massively parallel experiments that are unfeasible in the traditional setting. Miniaturized chemical analysis systems can also be used to develop point-of-care healthcare products that can dramatically improve expand access to health diagnosis and lower the cost of healthcare.

While microfluidic research in recent years has produced many technologies for precisely metering and manipulating small volumes of liquid [1], research in detection and readout technologies has not seen the same level of advances. In fact, as summarized in Table 1.1, many existing chemical detection technologies are expensive, bulky, and cannot be easily reduced to a small form-factor. As a result, new chemical detection technologies and new methods of integrating existing technologies into a small form-factor has become a major area of research.

Technique	Detection Parameter	App. Cost	Mechanism Volume	Challenges in developing miniaturized or portable systems
Mass Spectrometry	Mass/charge ratio	\$25k	1 m ³	Complexity; high power density
Fluorescence Detection	Autofluorescence or a fluorophore labeling molecule	\$25k	1 m ³	Small scale imaging optics; Specific binding with a fluorophore molecule; not a quantitative technique
UV-Vis Spectroscopy	Optical absorption spectrum	\$3k	0.1 m ³	Small scale optical spectrometer
Raman Spectroscopy	Molecular vibrational and rotational modes	\$25k	1 m ³	Laser excitation source; small scale optical spectrometer
Infrared Spectroscopy	Optical absorption spectrum	\$25k	1 m ³	Infrared source; small scale optical spectrometer
Atomic Absorption	Optical absorption of atomic elements	\$25k	1 m ³	High power source for vaporization or volatilization of sample into atomic form; small scale optical spectrometer
NMR	Nuclear spin	>\$500k	100 m ³	High magnetic field; high power RF signal

Table 1.1: Comparison of common chemical analysis technique with approximate price and volume of existing instruments and challenges in developing an equivalent miniaturized or portable system.

This thesis focuses on electrochemical impedance spectroscopy (EIS), a simple yet powerful chemical analysis technique that uses an electric field to measure the

permittivity and conductivity of sample liquids and gases. EIS is particularly interesting for miniaturized chemical analysis systems because of its favorable detection limits and its all-electrical measurement, which makes it simple to integrate within miniaturized and portable systems. A major problem in current EIS systems, however, is the lack of absolute accuracy and repeatability owing to the geometrical uncertainties of the sample chamber. Consequently, current devices require calibration procedures that are unfeasible to perform in a miniaturized system.

The main contribution of this thesis will thus be to develop a technique for making accurate measurements of permittivity and conductivity that can also be applied in miniaturized systems. Specifically, the explorations in this thesis will revolve around measurements using a small adjustable electrode gap between spherical electrodes, which enhances the accuracy of this measurement and eliminates the need for wet calibration. The target accuracy of this work is to be within 1% of the established values of permittivity and conductivity, using devices that do not require wet calibration procedures. A further contribution of the mechanism developed in this thesis is the capability for creating adjustable nanometer electrode gaps, which can potentially be used to study the properties of liquids in highly confined geometries and to investigate how they differ from bulk environment.

The rest of this chapter will present the motivation and background for EIS studies in miniaturized chemical analysis systems. Section 1.2 will illustrate the motivation for miniaturized chemical analysis devices by presenting a case study where such devices are critically needed. Section 1.3 will review the application of EIS and the challenges in obtaining absolute accuracy. Section 1.4 will review examples of EIS

measurement devices designed for miniaturized chemical analysis systems. Section 1.5 will discuss prior art in making highly accurate EIS measurements. Section 1.6 describes the approach taken in this thesis to develop accurate EIS measurements that is also compatible with miniaturized systems. Section 1.7 describes the background of devices for electrical measurements across nanometer electrode gaps. Finally, Section 1.8 will outline the organization of this thesis.

1.2 Case Study: The Diethylene Glycol Poisoning Tragedy

A compelling case study that illustrates the need for miniaturized chemical analysis systems is the recent mass poisoning incident in Panama where pharmaceutical grade glycerin was replaced with toxic diethylene glycol (DEG) and resulted in the death of at least 100 people [2]. Glycerin is a sweet-tasting syrup often found in food, drugs, and toothpaste. DEG is an industrial solvent commonly used in antifreeze. DEG looks, tastes, and behaves like glycerin, but when ingested, it causes kidney failure, paralysis, and in most cases, death. In the Panama case, a chemical trader in China used DEG to substitute for the more expensive glycerin and provided fake certifications. The counterfeit glycerin then passed through trading companies in China, Spain, and Panama before Panamanian government officials unwittingly mixed it into 260,000 bottles of cough and antihistamine syrup. The source of the poison was not discovered until many months later – after the medicine had already been widely distributed and at least 100 had died. In fact, DEG was identified as the culprit only after samples of the tainted cough syrup were sent to the Center for Disease Control and Prevention in the U.S. for testing.

The Panama case is not an isolated incident of DEG mass poisoning. Over the past two decades DEG counterfeiting as glycerin has been linked to mass poisonings in Haiti, Bangladesh, Argentina, Nigeria, China, and India [2, 3]. The estimated total number of deaths range from thousands to tens of thousands. Recently, DEG has been discovered in some brands of toothpaste distributed in the United States prompting a large scale investigation [4].

The sequence of events that led to the DEG mass poisoning in Panama indicate the need for more frequent chemical testing with multiple levels of redundancy. It is particularly tragic to consider that the shipment of chemicals exchanged hands on three different continents and yet no one bothered to confirm the contents of the label. While future regulations may require testing each time such products are sold, a simple device with the capability to identify DEG could dramatically lower the threshold for testing. Imagine a cell phone-sized device costing perhaps \$25 that could be used by chemical traders, pharmaceutical manufacturers, and government inspectors for on-the-spot analysis without having to send samples to a specialized lab. For consumers, it could also mean that products, such as cough syrup and toothpaste, suspected of DEG contamination can be quickly tested and reported. This type of device could also be used in hospitals for analyzing patients' blood for DEG contamination so that life-saving treatment could be delivered before it is too late.

1.3 Electrochemical Impedance Spectroscopy and Its Challenges

Electrochemical Impedance Spectroscopy is a chemical analysis technique for measuring the permittivity and conductivity of liquids or gases. The permittivity is

indicative of the electrical polarizability of the material, while conductivity is indicative of the density and mobility of charged ions. In solutions, permittivity is primarily dependent on the makeup of the solvent while conductivity is primarily dependent on the density and mobility of the solute. Since solute concentrations can vary over many orders of magnitudes, conductivity is typically the more highly varied parameter. As a result, conductivity is more often used as a sensing parameter than permittivity. Currently, conductivity measurements are applied to a wide range of industrial, scientific, and medical applications. In low conductivity liquids, conductivity is often used in quality control applications such as monitoring the purity and contaminant concentration for water in power plants [5, 6], groundwater [7], chemical production [8], and lubrication fluids [9]. In electrochemical devices such as batteries and electrolysis cells, accurate measurements of the electrolyte conductivity provide important parameters that could be used in the design and optimization of these systems [10]. In medical devices, permittivity and conductivity are used to measure a number of physiological parameters such as red blood cell count [11] and blood osmolarity [12].

As a chemical detection technology in micro chemical analysis, the direct application of EIS lacks inherent selectivity. Chemical selectivity can be obtained using conductivity assays that specifically react with target compounds to produce a proportional conductivity change. In the DEG poisoning case study, products that are suspected of DEG contamination could be added to a conductivity assay containing an enzyme that specifically reacts with DEG. The differential conductivity between the enzyme assay and a control assays can then be used to establish the presence and

concentration of DEG. Accurate and repeatable EIS measurements are absolutely critical in these scenarios.

A key problem in EIS measurements is the extraction of the intrinsic values of permittivity and conductivity, ϵ and κ , from measurable quantities of capacitance and conductance, C and G . These quantities are related by the geometrical factor of the cell constant, or K_{cell} and the fringing field capacitance and conductance, C_0 and G_0 , according to the following equations,

$$C = \frac{\epsilon}{K_{cell}} + C_0. \quad (1.1)$$

$$G = \frac{\kappa}{K_{cell}} + G_0. \quad (1.2)$$

Since C_0 and G_0 are artifacts of the electrode geometry and the manufacturing process, contributions from these terms cannot be easily predicted. As a result, it is very difficult to determine ϵ and κ based on direct geometrical calculations of K_{cell} . Techniques such as guard electrodes can reduce the value of C_0 and G_0 , but not eliminate them completely. While other effects, such as absorption on electrode surfaces, exacerbated the errors by altering the effective size of the impedance test cell.

Existing conductivity meters typically address this problem by periodically calibrating the impedance test cell using a standard solution with established values of ϵ and κ . This correction is of limited value since the contribution from C_0 and G_0 can also be dependent on the value of ϵ and κ . As a result, the calibration is only valid if ϵ and κ of the sample and calibration fluid are similar [9, 10]. In miniaturized impedance test cells, the use of calibration liquids is often impractical since the calibration liquid may

irreversibly contaminate the impedance test cell, and the extensive cleaning procedures used in conventional systems are not available.

Accordingly, a key contribution of this work is the development of an accurate technique for measuring ϵ and κ without requiring the use of calibration liquids, which is also compatible with miniaturized chemical analysis systems. Since current portable impedance test cells are specified to be accurate to within 1% after wet calibration, this level of accuracy is deemed as an appropriate target for this work without wet calibration.

1.4 Current Miniaturized Impedance Test Cells

The geometrical uncertainties in macroscale impedance test cells are exaggerated in miniaturized impedance test cells because of constraints in materials and fabrication methods. Examples of two miniaturized impedance test cells, shown in Figure 1.1 and Figure 1.2, are discussed in order to illustrate these issues. Figure 1.1 shows one common design where interdigitated electrodes of alternating polarity are patterned on a silicon or glass substrate and encapsulated in a thin channel. The cell constant is controlled by the length, width, and separation of the electrodes. Since the electric field in this impedance test cell is concentrated at the edges of the electrode, the measured impedance will be highly dependent on geometrical imperfections of the electrodes. Therefore, calibration using a standard liquid is required in order to make accurate measurements. Since the electric field traverses through both the sample liquid and the substrate as shown in figure, the effect of the parasitic capacitance and resistance will be dependent on permittivity and conductivity of the sample liquid. Therefore, the calibration is valid only if the properties of the calibration liquid are similar to that of the sample liquid.

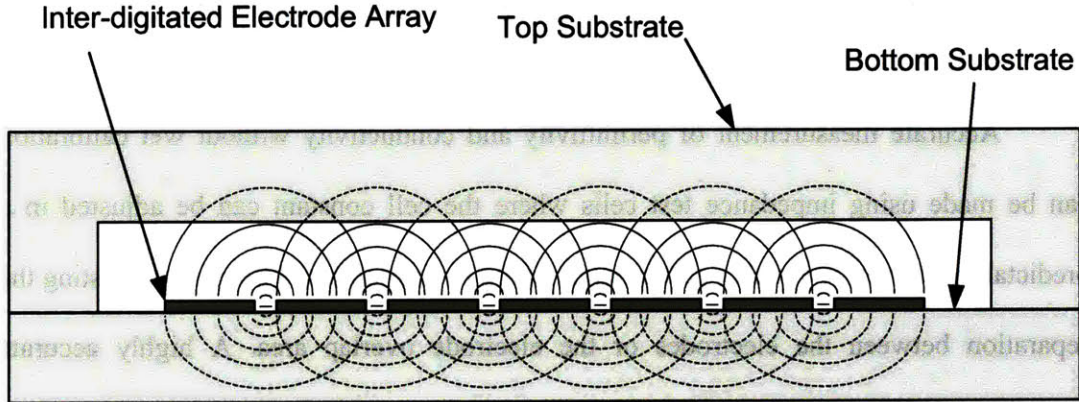


Figure 1.1: Design of a microfabricated impedance test cell based on interdigitated electrodes.

Figure 1.2 shows the impedance test cell developed by Oh [13], which uses a parallel plate geometry to create a small gap between highly doped silicon and polysilicon electrodes with a thin silicon dioxide separator between the electrodes. This design is subject to the similar errors as the interdigitated electrode design since the measuring electric field traverses the both the sample and the oxide layer. Furthermore, the microfabrication processes required to remove the oxide layer are subject to large uncertainties in the area oxide layer.

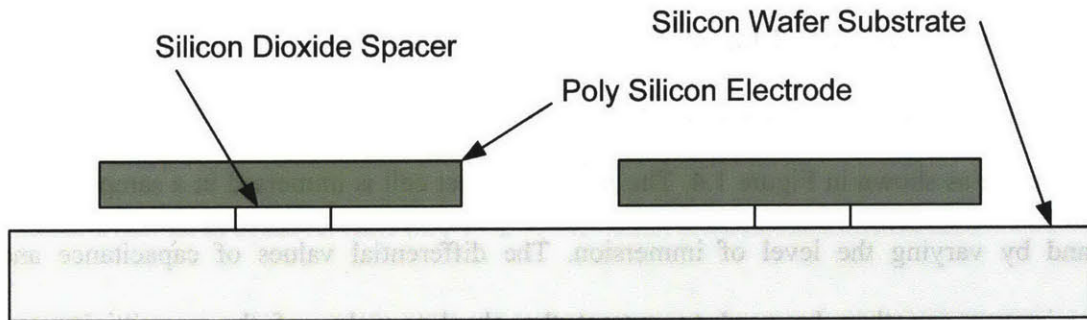


Figure 1.2: Design of a microfabricated impedance test cell based on oxide etching.

1.5 Permittivity and Conductivity Measurements without Wet Calibration

Accurate measurement of permittivity and conductivity without wet calibration can be made using impedance test cells where the cell constant can be adjusted in a predictable manner. A variable cell constant could be implemented by either adjusting the separation between the electrodes or the electrode overlap area. A highly accurate realizations of the former scheme has been developed by Barthel [14, 15] at the University of Regensburg in Germany and Wu [16] at the National Institute of Standards and Technology (NIST), and have been used to obtain standard reference values for permittivity and conductivity [17, 18]. A picture of the Wu device is shown in Figure 1.3 where the sample media is encapsulated in a glass cylinder with platinum electrodes mounted on the end of the cylinder. The cylinder has a removable section of a precisely measured length. The differential capacitance and conductance measured with and without the middle section are used to compute the absolute permittivity and conductivity.

A simpler method for adjusting the cell constant was developed by Shiefelbein [10], which consists of an inner rod electrode concentric with an outer cylindrical electrode as shown in Figure 1.4. The impedance test cell is immersed in a sample liquid and by varying the level of immersion. The differential values of capacitance and resistance can then be used to extract the absolute value of the permittivity and conductivity. This apparatus enabled measurements of the conductivity of KCl solutions within 1% of standard reference values.

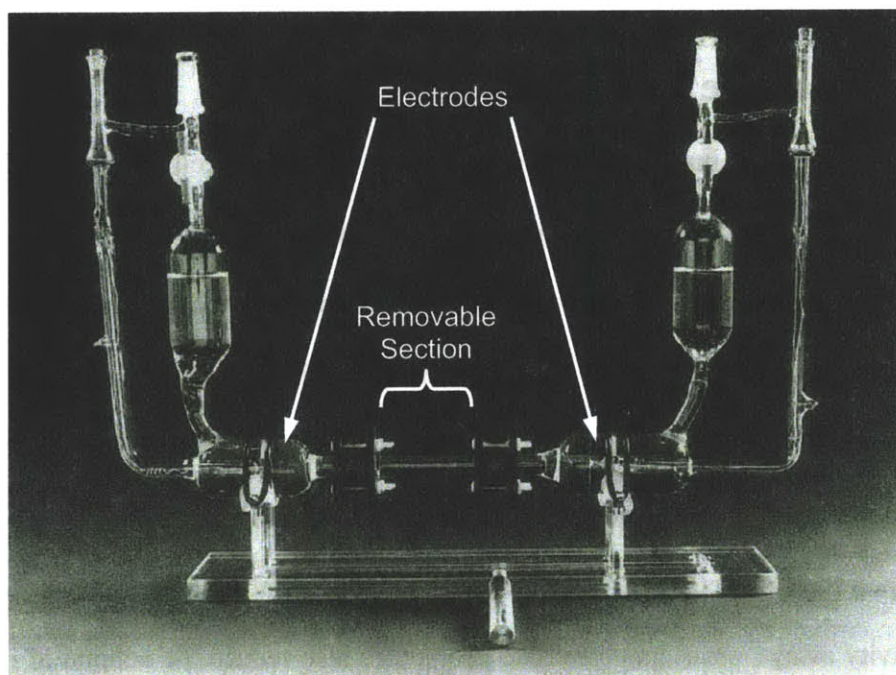


Figure 1.3: Photograph of Wu's apparatus developed at NIST [16] for measuring the absolute specific conductivity of KCl solutions.

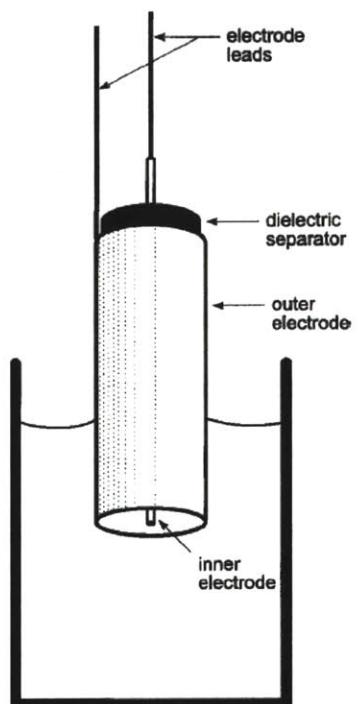


Figure 1.4: Illustration of the apparatus developed by Shiefelbien [10].

1.6 Optimization of Impedance Test Cells with Adjustable Cell Constant

The design of impedance test cells with an adjustable cell constant highlights a fundamental tradeoff between varying the cell constant over a sufficient range in order to make an accurate estimate of the permittivity and conductivity, while minimizing the variation of parasitic capacitance and conductance. This tradeoff is optimized at small electrode separations because small modulations of the electrode separation result in large variations of the cell constant, while the corresponding variations of parasitic capacitance and conductance are minimal. In micro chemical analysis systems that utilize conductivity assays, small gap electrode geometries also reduce the volume of reactants, and therefore the total cost of analysis.

The design of impedance test cells with small, adjustable electrode separations between planar electrodes can be fraught with practical challenges since parallelism errors between the electrodes can produce large offsets in the measured result. The parallelism problem can be avoided using spherical electrodes since the nearest points between two spheres, or a sphere and a plane, are by definition tangential. Spherical geometries are also very simple to manufacture, where precision machining and polishing processes can produce spheres with high diametrical accuracy and low surface roughness. In fact, it is common to see spheres with sub-micrometer diametrical tolerances and surface roughness R_a 's of a few nanometers. Leveraging these two parameters enables accurate measurement of permittivity and conductivity.

1.7 Electrical Measurements across Electrodes Separated by Nanometer Gaps

The nanometer smooth surfaces of spheres enable the electrodes to be brought extremely close to one another without touching to create an extremely small electrode gap. The minimum electrode separation is limited only by the surface roughness of the electrodes, which can have peak-to-valley ranges from 10 to 20 nm. The ability to create nanometer gaps between electrodes presents an interesting opportunity for studying the electrical properties of nanoscale systems. In the past decade, methods for creating nanometer electrode gaps has gathered considerable attention as an apparatus for studying electrical conductivity in nanoscale systems. Current techniques for creating these devices typically involve either scanning probes such as STMs [19] and conducting AFMs [20]; or microfabricated microwire junctions created using techniques such as mechanical fracture [21, 22], electromigration [23], electrochemical deposition [24], focused ion-beam etching [25], double-angled evaporation [26], and evaporation using a carbon nanotube mask [27]. While these devices have demonstrated promising capability, precise control of the separation and surface roughness of the electrodes remain a difficult task. Additionally, these devices encounter problems from fringing electric field lines outside of the nanogap. As these fabrication processes restrict the electrode gap to a small region of the overall electrode structure, the fringing field contribution will easily overwhelm the signal from the nanogap. Consequently, measured electrical conductivity values reported by different groups widely disagree [28].

The nanogap impedance test cell created using spherical electrodes differs from existing approaches in that the electrode gap is created between nanometer smooth macroscopic electrodes rather than atomically sharp conductors. The geometrical

certainty of this approach enables better measurement certainty than the current approach of using atomically sharp electrodes. The macroscopic lateral electrode dimensions in combination with the small electrode gap tightly constrain the excitation electric field within the interelectrode region, and thus minimizing error signals from fringing fields. Thus, a separate, but equally important goal of this thesis is to develop a method for creating adjustable nanometer electrode gaps for electrical measurements of nanoscale systems.

An important prior art relating to the generation of adjustable small gaps is the *Surface Force Apparatus* (SFA) of Tabor and Israelachvili that was developed to study the mechanical and rheological properties of thin liquid films [29-31]. The SFA traps liquids between crossed cylinders mounted on calibrated flexure springs to accurately measure the force-displacement curves of nanometer thin liquid films. The effect of surface roughness is minimized by wrapping the cylinders in a layer of atomically smooth mica, typically 2-4 μm thick. The separation between the cylinders is measured optically via a semitransparent layer of silver thin film, deposited on the back of the mica layers. The thin silver films create interference patterns that allow the surface separation distance to be determined with sub-nanometer accuracy using a video camera.

The primary use of the SFA has been for measuring the force-displacement curves of nanometer-thin liquid films. Only a few studies have touched upon the corresponding electrical properties. Franz and coworkers developed a technique to measure capacitance using the silver films as electrodes to measure separation and adhesion hysteresis between mica surfaces [32, 33]. Cho and Granick further applied this technique to measure the surface alignment, confinement, and shear field of *4-n-pentyl-4'*-

cyanobiphenyl, a common type of liquid crystal [34]. These works provided initial glimpses of the tight coupling between electrical and mechanical properties of nanometer thin liquid films. One shortfall of these experiments is that the silver electrodes were deposited on the back of the mica layers rather than on the front. Therefore, both capacitance and resistance measurements were obstructed by the insulating mica layers.

Georges and Tonck, and later, Restagno [35-37] constructed variants of the SFA, where one cylinder is replaced by a sphere, with a metal outer layer, and the second cylinder is replaced with a highly conductive planar surface. These two surfaces can be used as electrodes to measure capacitance and resistance as they are brought into contact with one another. This device has been used to study the electron tunneling during electrical contact [38], and the effect of surface roughness [39]. However, published literature does not indicate that this device had been used to measure permittivity and conductivity through nanometer-thin films of liquids and gases.

The findings of the SFA and its derivatives provide clues that the nanoscale properties of liquids may diverge far from bulk properties. The measurement of electrical properties in small gaps may be combined with the results from these studies to develop a comprehensive theory of liquids confined to within nanometer-thin films.

1.8 Thesis Outline

Chapter 2 will describe the design of the mechanism for creating an adjustable small electrode gap. The major components include the fabrication of the spherical electrode, the design of the impedance test cell, the mechanism for adjusting electrode position, and the means for measuring electrode displacement. The performance of the

mechanism is evaluated by its resolution and parasitic displacement errors. The supporting experimental apparatus, including the impedance measurement system, the temperature control system, and the data acquisition system, will also be described.

Chapter 3 describes the electrostatic and electrochemical model of the impedance test cell. The electrostatic section will describe the solution to Laplace's equation between two spherical surfaces and the associated errors that result from deviations from the ideal geometry and ideal mechanism. The electrochemical section will describe the Gouy-Chapman-Stern model of electrolytes and the equivalent circuit that describes the measured impedance. The measurable impedance as a function of frequency will be thoroughly analyzed with the aim of determining the optimal frequency range for measuring permittivity and conductivity.

Chapter 4 is a rigorous study of the data analysis techniques for extracting the most accurate values of permittivity and conductivity from capacitance versus displacement and conductance versus displacement datasets. The analysis techniques of weighted least squares fitting and non-linear fitting are investigated thoroughly and evaluated based on their sensitivity to systematic errors and random errors.

Chapter 5 presents the results intended to verify the designs, models, and analyses presented in previous chapters. Measurements of permittivity are demonstrated using both nitrogen gas and methanol. Measurements of conductivity are demonstrated using potassium chloride-solutions. Results from impedance measurements as a function of frequency are also presented. The last part of Chapter 5 presents measurements of very small electrode gaps, down to less than 20 nm. Models of surface roughness, which help to describe some of the measured results at nanometer electrode gaps, are also presented.

Chapter 6 summarizes the findings of this thesis and proposals for future work, which include a proposal to make disposable versions of the impedance test cell, as well as proposals for future experiments for studying nanometer properties of liquids.

Chapter 2

Design

The design of the apparatus for measuring electrical impedance using adjustable small gaps between spherical electrodes will be presented in three sections. The first section describes the design of the impedance test cell including the electrode, the electrode mounting apparatus, and the sample chamber. The second section describes the design of the position mechanism including the coarse adjustor, the fine adjustor, the metrology frame, and the results of the experiments evaluating the performance of the mechanism. The final section describes the design of the supporting instrumentation including the impedance measurement system, the temperature control system, and the data acquisition system.

2.1 Impedance Test Cell

2.1.1 Electrode

The spherical electrodes are fabricated using a silicon-nitride sphere, shown in Figure 2.1, as a substrate for a thin platinum electrode film. Originally produced for low-friction bearings and precision alignment equipment, silicon-nitride spheres have exceptional dimensional accuracy, mechanical stiffness, and surface quality.

The spheres used to fabricate the electrode have a diameter of 9.525 mm with a tolerance of ± 130 nm (Cerbec Saint Gobain Ceramics: Grade 5 spheres). The surface quality of the spheres was analyzed using a whitelight profilometer scans (Zygo) as shown in Figure 2.2. After subtracting the spherical shape, the Ra surface roughness is 2 nm and the peak-to-valley range of approximately 50 nm. For comparative purposes, the profile of a polished silicon wafers is shown in Figure 2.3, and have a surface roughness Ra of 1 nm and a peak-to-valley range of 20 nm.

The electrode film consists of a 50 nm platinum layer and a 5 nm chromium adhesion layer. The metal films are deposited on one hemisphere of the silicon-nitride spheres using electron-beam deposition. The surface profile shown in Figure 2.4 confirms that the electrode films coat the silicon-nitride spheres conformally and did not change the overall surface roughness profile. Based on the equations for the cell constant between spherical electrodes, the cell constant varies from 7.30 m^{-1} to 12.7 m^{-1} for electrode separations from $1 \text{ }\mu\text{m}$ and $50 \text{ }\mu\text{m}$.

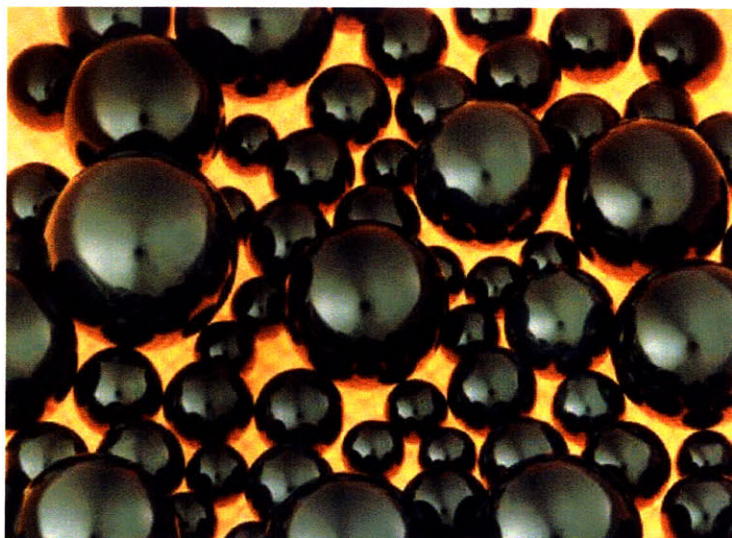


Figure 2.1: Photograph of silicon-nitride spheres (Source: Cerbec Saint-Gobain Ceramics).

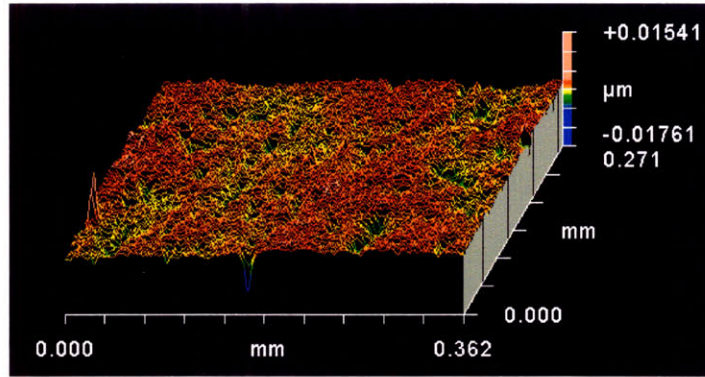


Figure 2.2: Surface profile of a silicon-nitride sphere. Surface roughness $R_a \approx 2$ nm; peak-to-valley ≈ 50 nm.

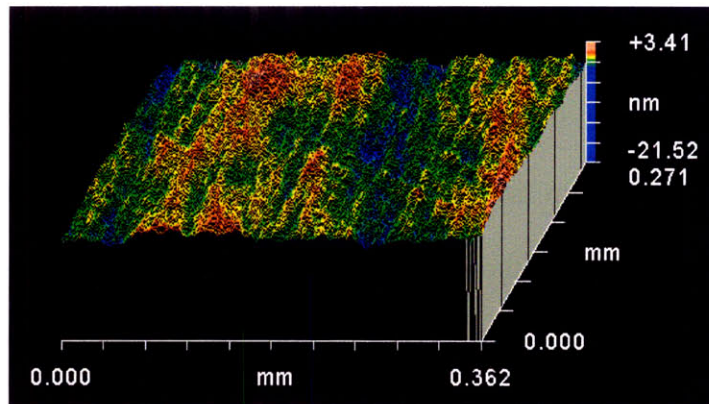


Figure 2.3: Surface profile of a polished silicon wafer. Surface roughness $R_a \approx 1$ nm; peak-to-valley ≈ 20 nm.

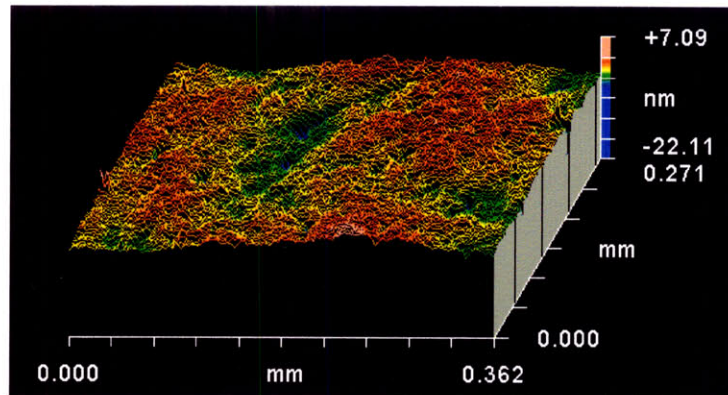


Figure 2.4: Surface profile of a silicon-nitride sphere with a 5 nm chrome layer and a 50 nm platinum layer. Surface roughness $R_a \approx 2$ nm; peak-to-valley ≈ 50 nm.

2.1.2 Electrode Mounting Shaft

The electrode mounting shaft is designed to mechanically constrain the electrodes while providing an electrical contact to the platinum film. The electrode mount consists of a 12.7 mm diameter cylindrical shaft where one end has been bored out for the electrode sphere. A ring nut holds the electrode sphere inside the bore with only a small region protruding as shown in Figure 2.5. Two dimples on the ring nut allow it to be tightened using a special wrench. When tightened, the ring nut bends slightly and applies a mechanical preload to the electrode to ensure that the electrode and shaft are tightly bound together. Mechanical contact between the ring nut and the electrode also serves as the electrical contact between the platinum film and the mounting shaft. Therefore, the mounting shaft becomes part of the electrode for measuring impedance.

The capacitance and conductance between the two mounting shafts is the primary contributor of parasitic capacitance and conductance. Based on a simple parallel-plate capacitance model, the stray signal from this source is expected to contribute approximately 30% of the measured signal for C. However, since the separation between the mounting shaft is significantly greater than the separation between the spheres, variation of the stray signal is considerably smaller. Detailed analysis of this error will be discussed in Section 3.1.2.

The electrode separation is modulated by precise adjustment of the position of the BMS using a flexural stage. Both mounting shafts are along an aligned axis along the flexure mechanism, and are electrically isolated via a 50 μm layer of polyimide film (McMaster: 2271K72). The position of each mounting shaft along its axial direction is measured using a commercial capacitance probe (Lion precision) as shown in Figure 2.6.

The measurement of the x -coordinate is therefore the sum of the two capacitance probes. In order to prevent the capacitance probe from interfering with the impedance measurement, grounded target electrodes are epoxied to the outer edge of each shaft.

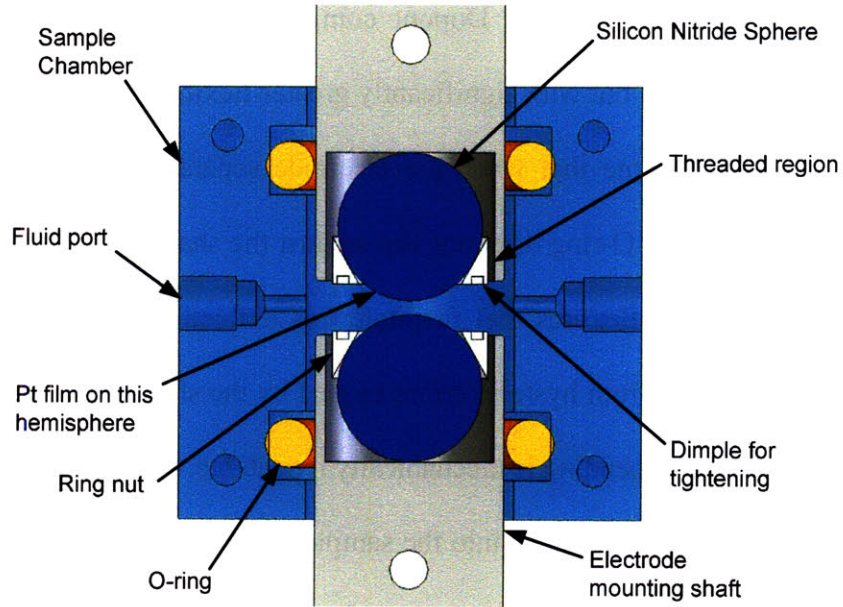


Figure 2.5: Cross section of the impedance test cell.

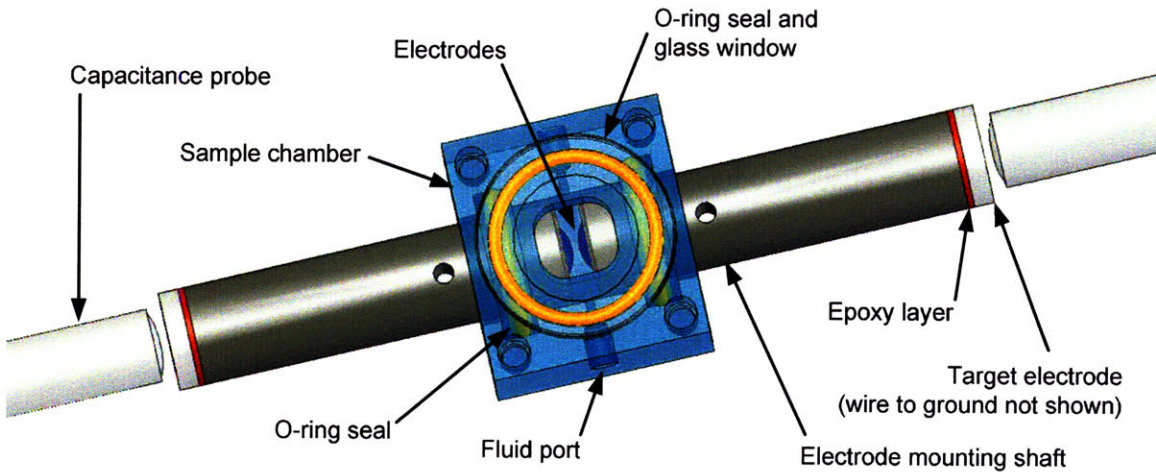


Figure 2.6: Impedance test cell with capacitance probes and target electrodes.

2.1.3 Sample Chamber

The sample chamber is designed to constrain the sample fluid between the electrodes while allowing small modulations of the electrode separation. As shown in

Figure 2.5, the sample chamber consists of a stainless steel cube with dimensions of 27.9 mm x 30.5 mm x 25.4 mm. The mounting shafts slide through a central bore of 13.7 mm. A liquid seal is established between each mounting shaft and the sample chamber via a Kalrez O-ring (#206 Dupont compound 4079), which offers similar solvent resistance to Teflon, but with significantly greater flexibility.

It is important to note that when the electrode separation is adjusted over the limited range of 50 μm , the O-ring does not slip against the shaft of the sample chamber. Rather, the O-rings act as flexures that facilitate this deflection by shearing. Unlike a sliding contact that suffers from hysteric errors caused by the sliding friction between the two surfaces, deflection by bending is mechanically repeatable.

Liquid samples are introduced into the sample chamber via fluidic ports for 1/16-inch OD tubing (Upchurch: M-644-03), connected to a standard syringe. The inlet port is located near the bottom of the chamber while the outlet port is located near the top in order to prevent air bubbles from accumulating in the chamber. The chamber also contains a window for debugging purposes. This window is covered with a 3 mm thick round Pyrex window (Esco products: P705125) and is sealed by another Kalrez O-ring.

2.2 Positioning Mechanism

2.2.1 General Orientation

The positioning mechanism, as shown in Figure 2.7, is an aluminum monolith consisting of three main functional groups: coarse adjustor; fine adjustor; and metrology frame. The electrode mounting shafts are constrained to the aluminum monolith using a semicircular clamp as shown in Figure 2.8. The top shaft is connected with a symmetric

dual beam flexure, which is part of the fine actuator. The bottom shaft is not rigidly clamped when the coarse adjustor is active, but once the desired position has been reached, this shaft is similarly fixed via a semicircular clamp.

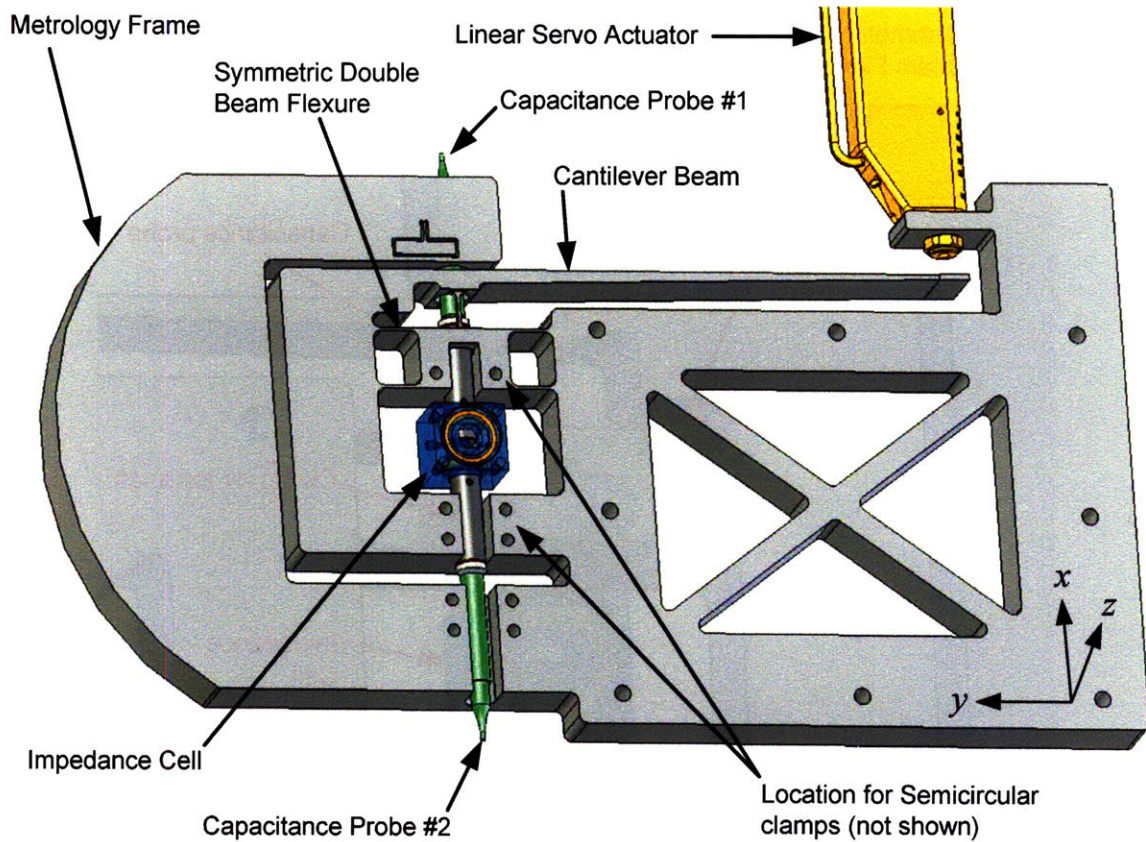


Figure 2.7: Overview of the positioning mechanism.

2.2.2 Coarse Adjustor

The coarse adjustor sets the initial separation of the electrodes to within range of the fine adjustor. This mechanism consists of an ultra fine thread lead screw (Thorlabs: ¼"-80 screw FS25AB200), shown in Figure 2.8, that advances the bottom mounting shaft. The positioning accuracy is enhanced by an anti-backlash bushing which applies a consistent preload to the screw. Assuming 1° angular resolution is achievable by hand, the position of the electrode can be advanced with a resolution of 0.3 μm. In order to

prevent the lead screw from deforming the flat surface, a steel puck with one flat and one conical surface is added to the interface between the spherical tip on the lead screw and the flat surface of the mounting shaft.

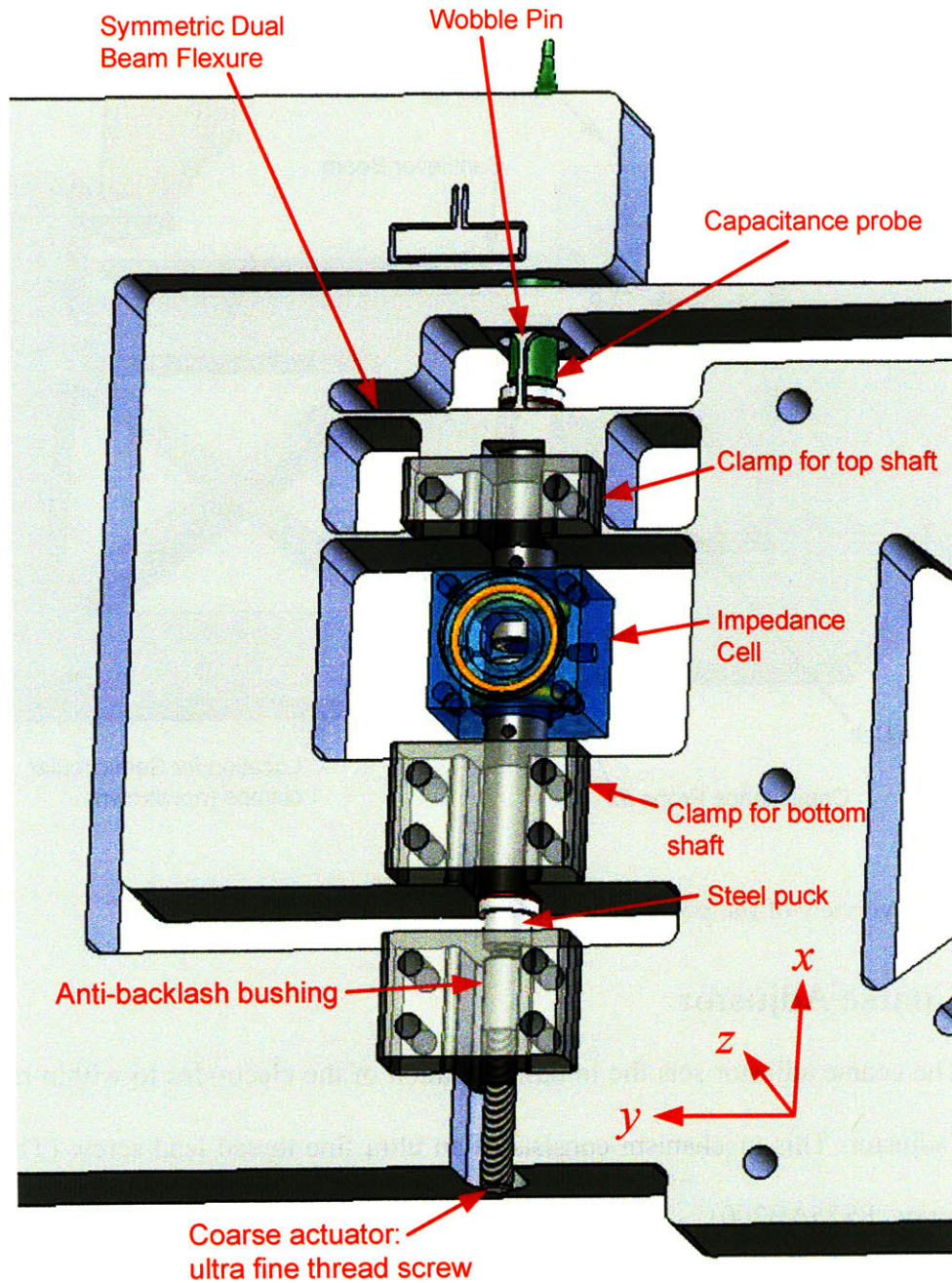


Figure 2.8: Detail of the flexure mechanism design including coarse actuator, capacitance probe, and clamps for constraining the electrode mounting shaft.

The coarse adjustor is mounted on a separate aluminum block that can be detached from the main frame. Once the desired electrode position has been reached, the bottom mounting shaft can be rigidly clamped to the frame. The coarse adjustor can then be retracted and replaced by a capacitance probe that measures the displacement of the bottom mounting shaft. The removable coarse adjustor reduces the complexity of sensing and displacing the same surface.

2.2.3 Fine Adjustor

The fine adjustor is designed to control the position of the top electrode mounting shaft with nanometer accuracy from a servomechanical actuator. As indicated in Figure 2.7, there are four main components in this mechanism: symmetric dual beam flexure, wobble pin, cantilever beam, and the linear servo actuator.

The symmetric dual beam flexure constrains the displacement of the top shaft along the vertical direction with high mechanical impedance. The ratio of the stiffness of this flexure relative to that of the cantilever beam acts to de-magnify the displacement of the actuator with a high transmission ratio. The stiffness of this flexure is controlled by the length and width of the flexure beams. These dimensions are chosen to maintain maximum stiffness while staying within the load capabilities of the actuator.

A common problem in many mechanisms with high transmission ratio is the presence of parasitic displacement along orthogonal axes. In order to constrain displacement of the top shaft along the x -axis, while reducing parasitic displacement along the y - and z -axes, a wobble pin is used to transfer displacement from the cantilever beam to the symmetric dual beam flexure. Unlike traditional designs that use a single rounded pin [40], the wobble pin here is monolithic with the rest of the flexure and

consists of two thin flexure beams. The two-prong design provides the flexibility desired in a wobble pin with the capability to add a capacitance probe at the center. The two-prong flexure beams are manufactured by first drilling a center hole in the flat aluminum stock, and then machining a small amount of material away from the other surfaces, before using the waterjet to make the shape of the flexure beam.

The cantilever beam reduces the displacement from the actuator to the symmetric dual beam flexure. A tapered single-beam design efficiently distributes stress along the length of the beam. The transmission ratio is set by the relative stiffness of the symmetric dual beam flexure and the stiffness of the cantilever beam. These values are optimized using finite element analysis to set a transmission ratio of 200:1. The maximum deflection of the cantilever beam is designed to be 50% of the yield stress of 6061-T6 aluminum, which limits maximum deflection to be approximately 10 mm. This range is enforced by the distance from the bottom edge of the cantilever beam to the main body of the flexural mechanism.

The linear actuator advances the electrode position by deflecting the tip of the cantilever beam. The actuator is a servomechanical leadscrew with feedback from an optical rotary encoder (Newport: LTA-HL). This actuator has a minimum incremental step of 50 nm and a 7 nm encoder resolution. Based on the designed 200:1 transmission ratio, this mechanism can be positioned in increments of 0.25 nm

The tip of the actuator is a non-rotating sphere, 6mm in diameter. In order to ensure consistent contact between the actuator and the cantilever beam and prevent plastic deformation of the beam, a polished tungsten-carbide flat is added to the interface between the tip of actuator and the tip of the cantilever beam. The polished tungsten-

carbide flat was a triangular lathe insert, and it is epoxied to the tip of the cantilever beam.

The maximum stress of the flexure is designed to be no more than 50% of yield strength for 6061-T6 aluminum, the maximum range of this mechanism is 10 mm, which corresponds to a fine positioning range of 50 μ m. The maximum displacement range is enforced by the spatial constraints both above and below the cantilever beam.

2.2.4 Metrology Frame

The displacements of both electrode mounting shafts are measured via capacitance probes (Lion Precision) as shown in Figure 2.7. These capacitance probes are specified with an RMS resolution of 0.2 nm and a bandwidth of 100 Hz. These probes are mounted in a metrology frame that is structurally isolated from the rest of the mechanism. The metrology frame is C-shaped, as opposed to an ideal closed shape. However, this is compensated by its robust size and integration with the aluminum monolith from which the entire device is constructed. The top probe reaches through a hole between the two flexures of the wobble pin. The diameter of the hole is greater than the diameter of the probe in order to prevent the motion of the cantilever beam from displacing the probe. The bottom capacitance probe measures the displacement of the bottom mounting shaft resulting from slight bending of the frame. Accurate measurement of the total electrode displacement can be obtained by adding the results from both probes.

2.2.5 Mechanism Evaluation and Error Analysis

The design of the fine adjuster is validated by measuring its transmission ratio, TR , and the error motions along orthogonal axes. The TR is defined as the ratio between

the displacement of the actuator and the displacement at the top electrode. These quantities are plotted against each other in Figure 2.9, where the x -axis is the actuator position and the y -axis is the electrode displacement. The TR , the inverse of the slope of the graph, is 188.8 with a standard deviation of 0.077. Since the minimum incremental displacement of the actuator is 50 nm, this means that the minimum incremental displacement of the electrode is correspondingly, 0.265 nm. The differences between the predicted and actual value for TR most likely come from machining inaccuracies in the size and shape of the symmetric dual beam flexure. The TR is especially sensitive to the radii at the corners where the flexure beams joins the main aluminum body.

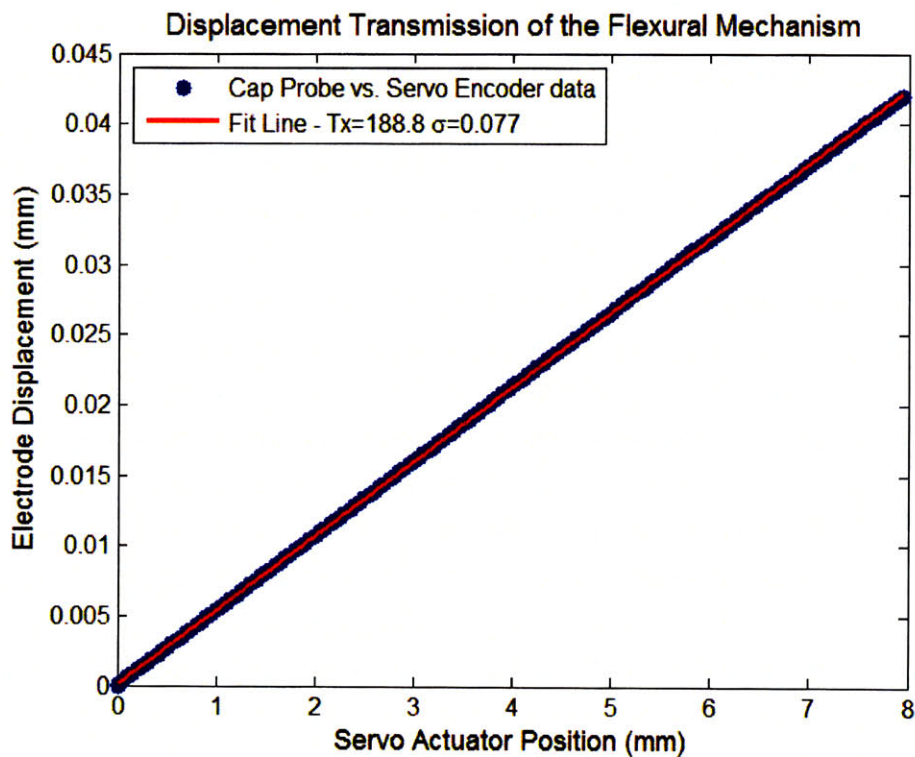


Figure 2.9: Measurement of the transmission ratio from the servomechanical actuator and the top electrode.

The parasitic displacements of the top electrode along the y - and z -axes are measured using additional capacitance probes. The measured displacements of the y - and

z-axes, along with the displacement of the bottom mounting shaft are plotted as a function of actuator displacement in Figure 2.10. As expected, the parasitic displacement along the y-axis is smaller than the z-axis, since the flexural wobble pin in this design is significantly more effective at attenuating parasitic displacement along the y-axis than the z-axis. Parasitic displacements along the y- and z-axes of the top electrode also show regular variations with a 1 mm period, which is likely due to a regular unevenness in the gear mechanism in the actuator. The effect of the parasitic displacements on impedance measurements will be studied in detail in Section 3.1.3.

The graph in Figure 2.10 further indicates that displacement of the bottom shaft is smaller than the top shaft by a factor 50:1. This value may become even lower when the electrode surfaces approach each other and begins provide a counter force.

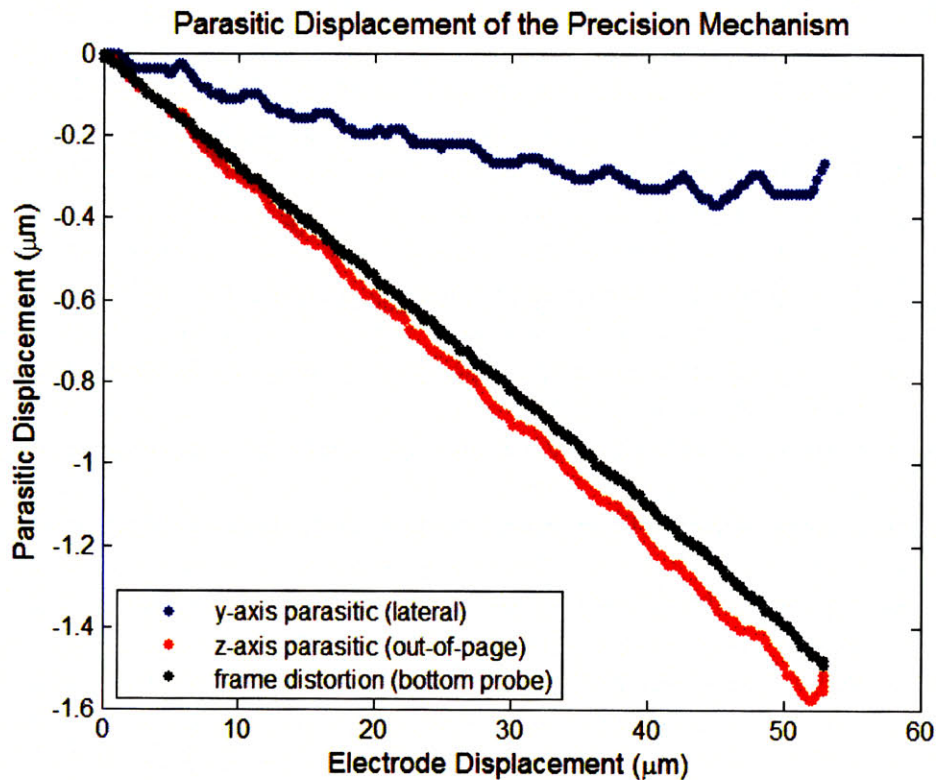


Figure 2.10: Parasitic displacement along the y- and z-axes and the frame distortion measured by the bottom probe. Parasitic displacement along the y-axis is attenuated by the wobble pin.

2.3 Instrumentation

The instrumentation around the impedance test cell and position mechanism consists of impedance measurement, temperature control, and data acquisition systems.

2.3.1 Impedance Measurement

The interelectrode sample impedance is measured using an Agilent 4284A LCR meter. The 4284A measures the complex impedance across a two-terminal device from a sinusoidal excitation. The frequency of the excitation signal can range from 20 Hz to 1 MHz; the amplitude can range from 5 mV_{RMS} to 20 V_{RMS}. The accuracy of the measurement typically ranges from 0.01% to 0.1% depending on the impedance measured.

The 4284A measures impedance using an auto-balancing bridge as shown by the simplified circuit in Figure 2.11. One terminal of the test impedance, Z_X , is connected to an oscillatory source at H with amplitude V_1 . The second terminal is connected to the virtual ground of an operational amplifier in the inverting configuration at L. The operational amplifier outputs a voltage across the feedback resistor such that no current flows into its input at L. Consequently, the sinusoidal current through the test impedance is converted into a sinusoidal voltage V_2 of the same phase. The complex impedance of Z_X is determined from the ratio of the amplitude and phase difference between V_1 and V_2 .

As discussed in Chapter 1, impedance measurements are vulnerable to stray impedances detected by fringing electric field. The amount of stray impedance can be reduced by using guard electrodes to alter the shape of the electric field. For an auto-balancing bridge, guard electrodes should be connected to ground, but electrically isolated the virtual ground at the node L. In the sample chamber, the top mounting shaft

is connected to H, while the bottom mounting shaft is connected to L. The sample chamber is electrically isolated from the two mounting shafts and connected to ground as a guard. As shown in Figure 2.12, electric field lines originating from the top electrode and ending on the bottom electrode is part of the measured impedance, while electric field lines originating from the top electrode and ending on the sample chamber has no impact on the measurement.

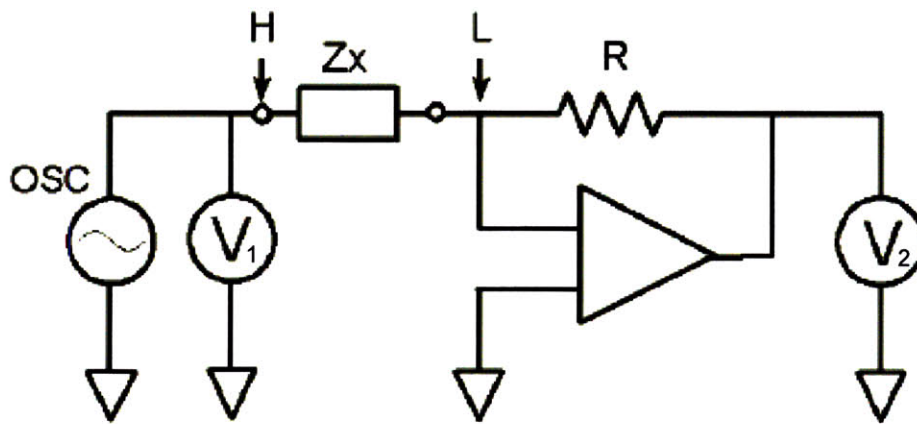


Figure 2.11: Simplified circuit diagram of the auto-balancing bridge technique used in the Agilent 4284A LCR meter [41].

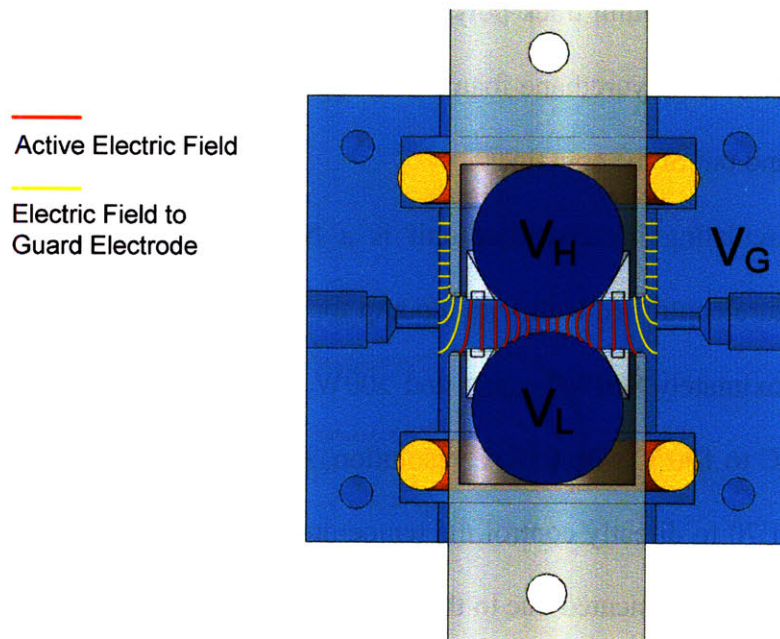


Figure 2.12: Electrical connection of the electrodes and sample chamber.

The specified accuracy of the Agilent 4284A LCR meter is approximately 0.1%. The impedance is measured as an in-phase component and an out-of-phase component. When the measured impedance is overly reactive or overly resistive, the complementary component is greatly diminished. As a result, the accuracy of the complementary component is compromised.

2.3.2 Temperature Control System

Temperature regulation is important for controlling the temperature of the sample chamber, as well as limiting errors caused by thermal expansion of the mechanism. This task is made specifically difficult since the servo actuator generates heat while moving and thus causing unpredictable thermal expansion and contraction. A high capacity temperature control system is developed in order to counteract this heat source.

The temperature control system consists of a thermal isolation chamber, a re-circulating heater-chiller, and a radiator. The thermal isolation chamber is an insulated shipping container with 50mm thick polyurethane walls. The opening of this container is capped with a flexible polyurethane foam, allowing electrical wiring and radiator tubing to be passed in and out of the container.

The recirculating heater-chiller unit is a NESLab RTE70 which integrates a precise temperature controlled bath with a pump for circulating the liquid. The RTE70 is capable of approximately 800W heating and 500W cooling power. It has a temperature range from -20°C to 100°C with 0.01°C resolution. An external thermometer can be used to allow the RTE70 to directly control the temperature at a specified location. However, this feature was not implemented due to the late delivery of the external thermometer.

The radiator facilitates thermal exchange between the cooling fluid and the flexure and the servomotor. The radiator is made of flexible cooper tubing bent to the shape of the flexure and actuator. The radiator is clamped to the flexure with thermal paste to enhance thermal conduction. A small fan circulates air in the chamber to equilibrate chamber temperature. A picture of the radiator and the flexure inside the thermal isolation chamber is shown in Figure 2.13.

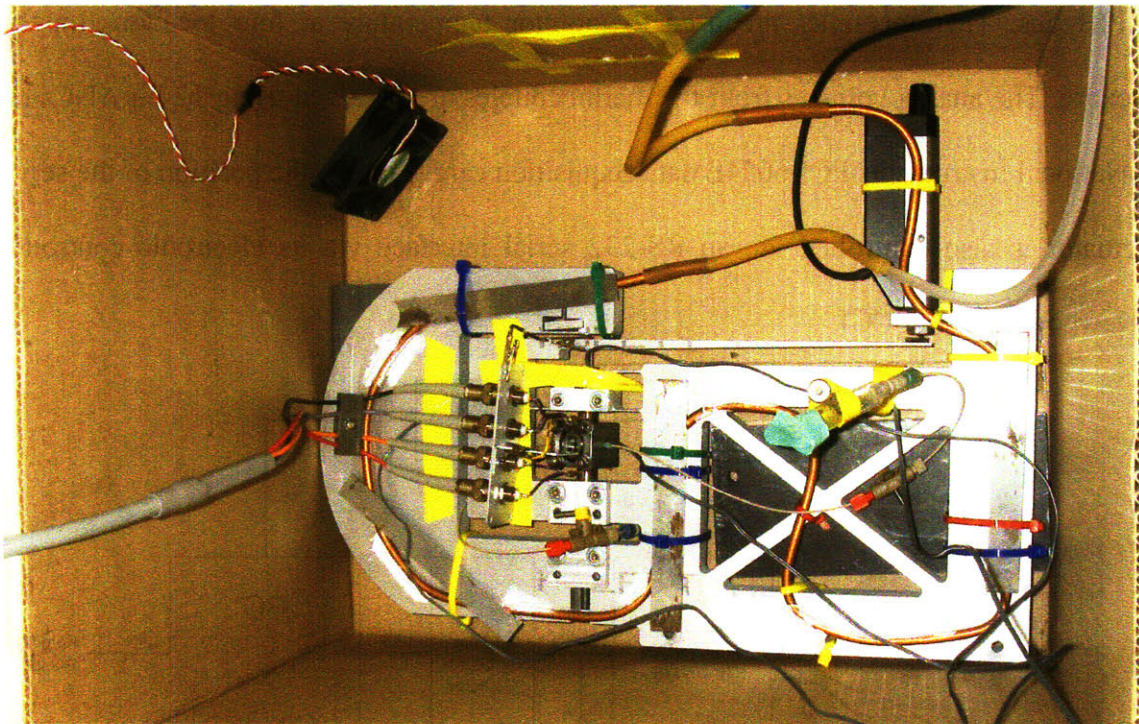


Figure 2.13: Picture of the flexure and actuator with the radiator system inside the thermal isolation chamber.

2.3.3 Data Acquisition System

A PC-based data acquisition system controls and automates the functions of the instruments and actuators used in impedance measurements. This system is designed to measure impedance as the electrode separation is adjusted via the servo actuator while monitoring the parameters of electrode position and temperature.

The logical flow of measurement information is shown in Figure 2.14. Impedance measurement is made via a four-point probe from the Agilent 4284A with appropriate guarding. The data is sent via a GPIB interface, through a GPIB-LAN gateway (Agilent: E5810A) to the host PC. The positions of the top and bottom electrodes are measured using two capacitance probes which output a precise analog voltage. The voltages are digitized via two Agilent 34401A multimeters that also transmit its information via the GPIB bus. Thermocouples are used to monitor temperature at four locations on the flexure. The analog voltages from the thermocouples are digitized using 12-bit ADCs on a National Instruments PCI-6024E data acquisition card. Finally, the position of the servo actuator is also controlled via an RS-232 serial interface via its electronic controller (Newport: SMC100CC).

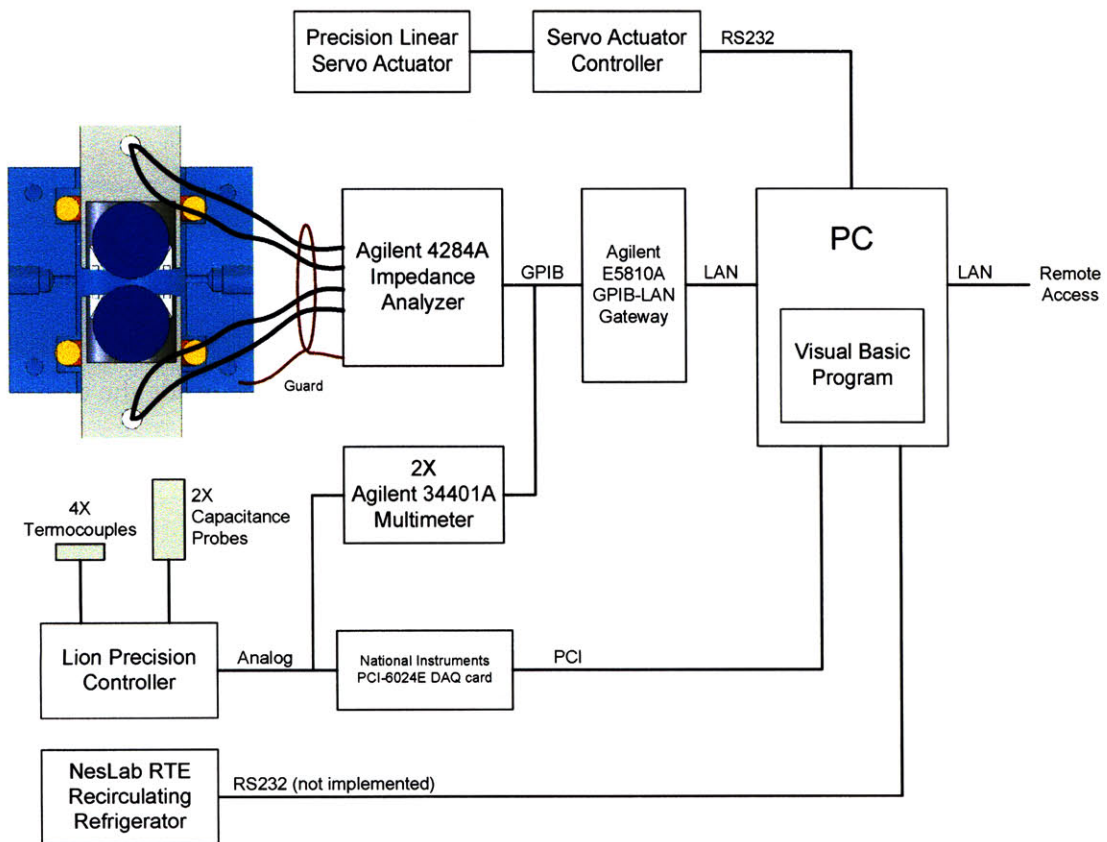


Figure 2.14: Schematic of the data acquisition system.

Computer control of all instruments and actuators are handled by a Visual Basic .NET 2005 program. This program automates data collection for many different conditions and records data into permanent memory. Windows XP Remote Desktop enables access to this program via the Internet, and thus greatly reducing the overhead time required for running experiments. A screenshot of this program is shown in Figure 2.15. The Visual Basic program is shown in its entirety in Appendix C.

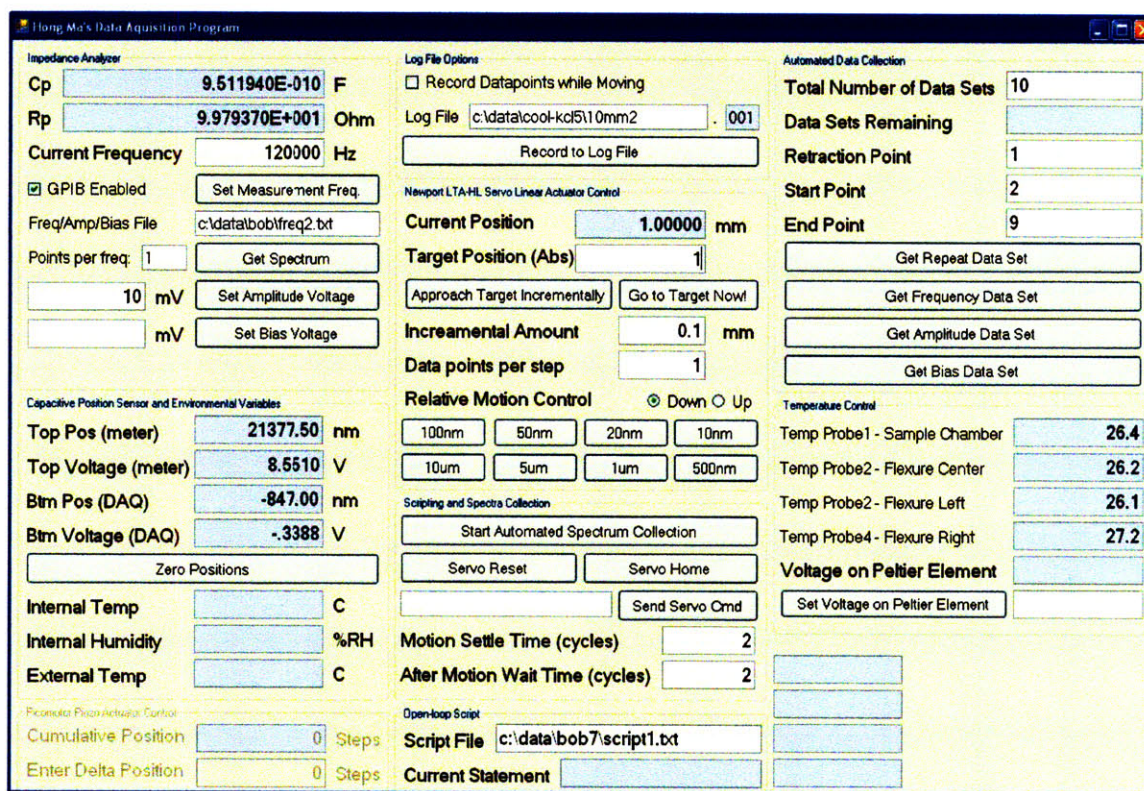


Figure 2.15: Screenshot of the Visual Basic .NET 2005 program used to control the entire experiment.

Chapter 3

Modeling

This chapter describes the modeling of the impedance test cell in two parts. The first part describes the electrostatic model of the spherical electrodes assuming that the intervening medium is uniformly polarizable. Errors resulting from geometrical shape and mechanical alignment are also studied. The second part describes the electrochemical model of the intervening material to show its frequency dependence. This model is used to determine the frequency regions for which the uniformly polarizable assumption is valid.

3.1 Electrostatic Model

3.1.1 Capacitance and Conductance between Spheres

The capacitance between two perfectly conducting spheres separated by a distance ξ measured from their nearest points, as shown in Figure 3.1, can be calculated by a series expression of the form,

$$C = 2\pi r \epsilon_r \epsilon_0 \sinh(\alpha) \sum_{n=1}^{\infty} \frac{1}{\sinh(n\alpha)} \quad (3.1)$$

$$\cosh(\alpha) = 1 + \xi/2r, \quad (3.2)$$

where r is the radius of the spheres, ϵ_0 is the vacuum permittivity, and ϵ_r is the relative permittivity. When electrodes are extremely close together, *i.e.* $x \ll r$, an approximate solution, as shown by Boyer [42], has the simpler form:

$$C = \pi r \epsilon_r \epsilon_0 \ln \left(\frac{2r}{\xi} \right) + C_0, \quad (3.3)$$

where C_0 is a constant. This expression has the characteristic that the spatial derivative of C is inverse-linear with ξ such that,

$$\left(\frac{dC}{d\xi} \right)^{-1} = -\frac{\xi}{\pi r \epsilon_r \epsilon_0}. \quad (3.4)$$

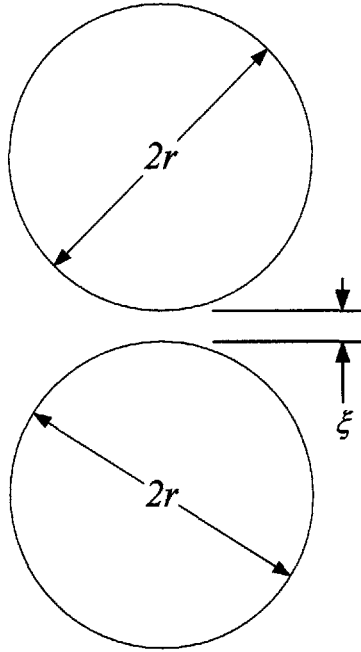


Figure 3.1: Electrostatic model of two spheres.

The conductance between two spheres follows a similar model, where the conductance, G , and conductivity, κ , between spherical electrode are related as,

$$G = \pi r \kappa \ln \left(\frac{2r}{\xi} \right) + G_0, \quad (3.5)$$

and

$$\left(\frac{dG}{d\xi}\right)^{-1} = -\frac{\xi}{\pi r \kappa}. \quad (3.6)$$

3.1.2 Errors due to Electrode Geometry

As discussed in Section 2.1.2, each spherical electrode is mounted on the end of a cylindrical mounting shaft, and it is constrained by a ring nut. The ring nut is stainless steel has the additional function of making electrical contact between the platinum film and the shaft. The mounting shaft alters the shape of the electrode from two spheres to the profile shown in Figure 3.2. Because of this shape difference the total measured capacitance is greater than the case of two isolated spheres. This error is somewhat compensated by the fact that the sample chamber is a guard electrode that is connected to ground, as described in Section 2.3.1, which effectively removes electric field lines emanating from the side of the high electrode. The magnitude of this geometrical error can be estimated by modeling the mounting shafts as an additional parallel plate capacitor adding a new term C_1 to equation (3.3),

$$C = \pi r \epsilon \ln\left(\frac{2r}{\xi}\right) + C_0 + C_1, \quad (3.7)$$

where C_1 is defined as,

$$C_1 = \frac{\epsilon_r \epsilon_0 A_1}{d_0 + x}. \quad (3.8)$$

The values for the frontal area A_1 and starting separation distance d_0 determined from the mechanical design as $9.1 \times 10^{-5} \text{ m}^2$ and 2 mm respectively. Since the plate separation varies with the separation between the spheres, this term and will contribute an

error to the measurement of permittivity and conductivity. However, since the average plate separation is much greater than the separation between the tip of the spheres, this error is expected to be a small contribution. The contributions from this error will be carefully studied in the next chapter.

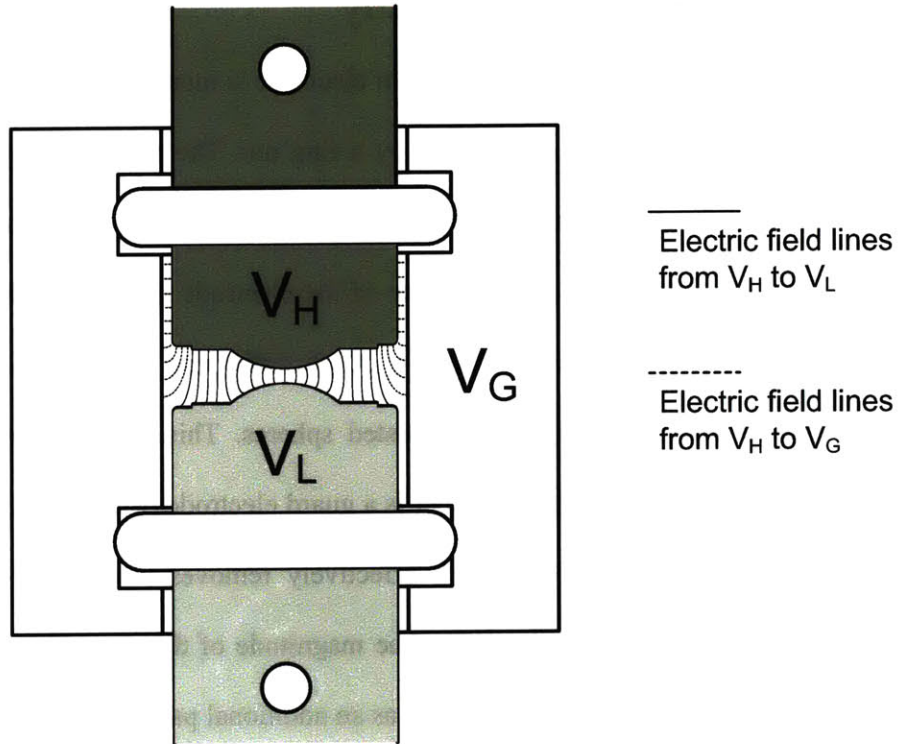


Figure 3.2: Electrode profiles and field lines modified by the mounting shaft.

3.1.3 Errors due to Mechanical Alignment

There are two types of alignment errors caused by the flexure mechanism. The first type is a lateral offset of the sphere centers as shown in Figure 3.3. Assuming the axis of displacement and the axis of displacement measurement are exactly parallel and the sphere centers are offset by the distance a , the actual electrode separation, ξ , and the apparent electrode separation, x , is related as,

$$\xi = \sqrt{a^2 + (2r + x)^2} - 2r. \quad (3.9)$$

The resulting error can be interpreted as a scale factor determined by

$$\frac{d\xi}{dx} = \frac{(2r+x)}{\sqrt{a^2+(2r+x)^2}}. \quad (3.10)$$

The upper bound for this error occurs at $x = 0$. Therefore, for the radius of 4.7625 mm and a reasonable alignment tolerance of 25 μm , $d\xi/dx = 0.999986$, or equivalently, an error of -0.0014%.

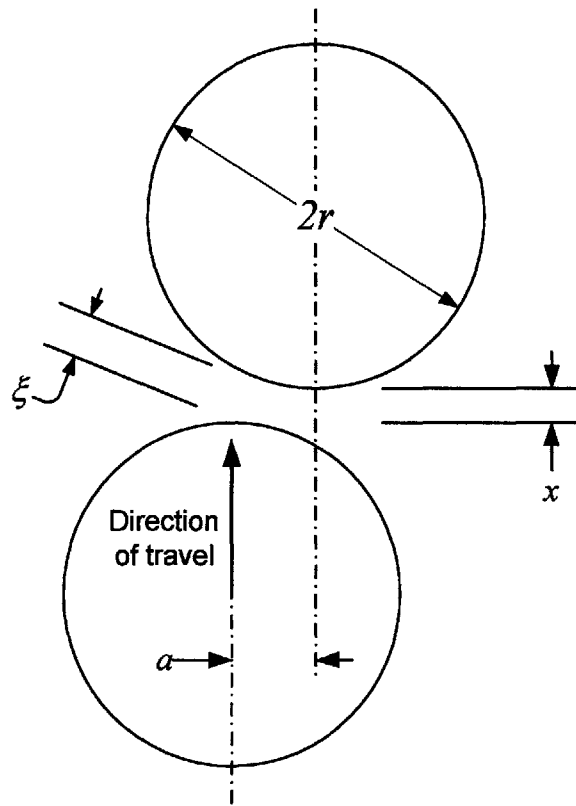


Figure 3.3: Lateral alignment error.

The second type of alignment error is the directional misalignment between the axis of measurement and the axis of displacement, as shown in Figure 3.4. The axis of measurement is determined by the angle of the capacitance probes, while the axis of displacement is determined by the motion of the fine adjustor and its associated parasitic

displacement. This type of alignment error also produces a scale factor error between the actual and apparent electrode separation, ξ and x , described by

$$\frac{\xi}{x} = \cos(\alpha), \quad (3.11)$$

where α is the angular error between the two axes. Using an generous estimate of $\alpha = 1^\circ$, the scale factor error, $d\xi/dx = 0.99984$, or equivalently -0.02%.

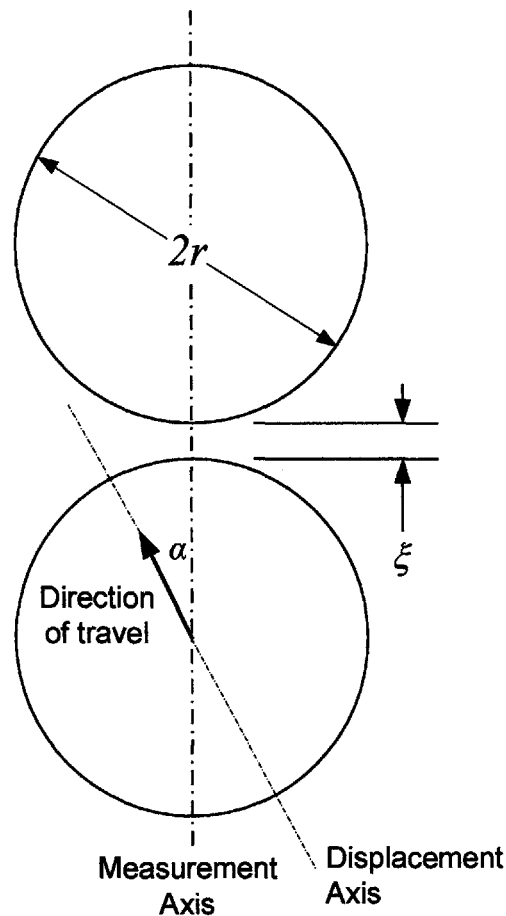


Figure 3.4: Angular alignment error.

The analysis of errors resulting from both lateral offset and angular misalignment using generous estimates of mechanical tolerance indicate that compensation is unnecessary for either types of errors.

3.2 Electrochemical Model

3.2.1 The Gouy-Chapman-Stern Model

The electrostatic model presented in the previous section is derived with the assumption of a uniformly polarizable media in the interelectrode gap. This assumption implies that the electrical load measured by the impedance analyzer can be represented as a simple parallel capacitor and resistor as shown in Figure 3.5.

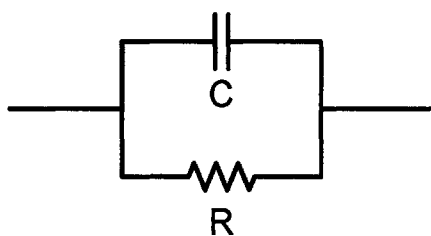


Figure 3.5: Equivalent circuit of a uniformly polarizable interelectrode medium.

The uniformly polarizing assumption is not true in most liquids as charge carriers are mobile and can move in response to an applied electric field. When the electrodes become charged, charge carriers will migrate towards electrodes of the opposite polarity forming a wall of charge that screens the bulk electrolyte and increases the overall capacitance of the system. In EIS literature, the charge carrier redistribution phenomenon is known as electrode polarization.

The physical chemistry of the interfacial region between the electrode and the electrolyte is an active area of research [43-46]. Its complexity lies in an aggregate of overlapping effects involving both specific and non-specific adsorption of ions and solvent molecules on the surface of the electrode. For situations where there is no electron transfer between the electrode and media, *i.e.* there is no oxidation or reduction reactions at the electrode-electrolyte interface, the presently accepted model of the

interfacial electrode charging phenomenon is the Gouy-Chapman-Stern (GCS) model [47]. This model separates the charge accumulation on the surface of the electrodes into a region where ions are specifically adsorbed on the surface of the electrode, known as the *Helmholtz layer* (*compact layer* and *Stern layer* are also terms used in literature); and a region of non-specifically adsorbed layer where the charge density fall off as an exponential with a characteristic length of the Debye length. Charge accumulation in the interfacial region can be modeled as two capacitors in series shown in Figure 3.6. Charge accumulation in the Helmholtz layer is independent of the applied voltage and is a function of the molecular composition of the solvent, solute, and the electrode. The capacitance, C_H , can be determined by,

$$C_H = \frac{\epsilon_0 \epsilon_r A}{d_{OHP}} \quad (3.12)$$

where A is the area of the electrode; and d_{OHP} is the thickness of the Outer Helmholtz Plane, which typically ranges from 1.5 to 7.5 angstroms [48].

Charge accumulation in the diffuse layer arises from the interplay between the tendency of the electrodes to attract the charge carrier and the tendency of thermal processes to randomize them. The resulting charge distribution can be obtained by solving the *Poisson-Boltzmann equation*, which yields an exponential charge distribution around each electrode with a characteristic length, L_D , known as the Debye length, given by,

$$L_D = \sqrt{\frac{\epsilon_0 \epsilon_r k_B T}{2n^0 z^2 q^2}} \quad (3.13)$$

where n^0 is the bulk number density of the ions in the solution, z is the charge of the ion, q is the elementary charge, and k_B is the Boltzmann constant.

The capacitance can then determined by,

$$C_D = \frac{\varepsilon_0 \varepsilon_r \cosh\left(\frac{zq\phi}{2k_B T}\right)}{L_D} \quad (3.14)$$

where ϕ is the potential across the diffuse layer.

The Helmholtz and diffuse capacitor can be combined into one double layer capacitor, C_p where,

$$\frac{1}{C_p} = \frac{1}{C_H} + \frac{1}{C_D} \quad (3.15)$$

The double layer capacitor is also presumed to be accompanied with an interfacial resistor, R_s , which should be significantly smaller than the bulk resistance owing to the elevated concentration of charge carriers in the Helmholtz and diffuse layers. Since it is assumed that no electrons enter or leave the electrode, the impedance near the electrode is entirely capacitive. Therefore, the interfacial capacitor and resistor is assumed to in series.

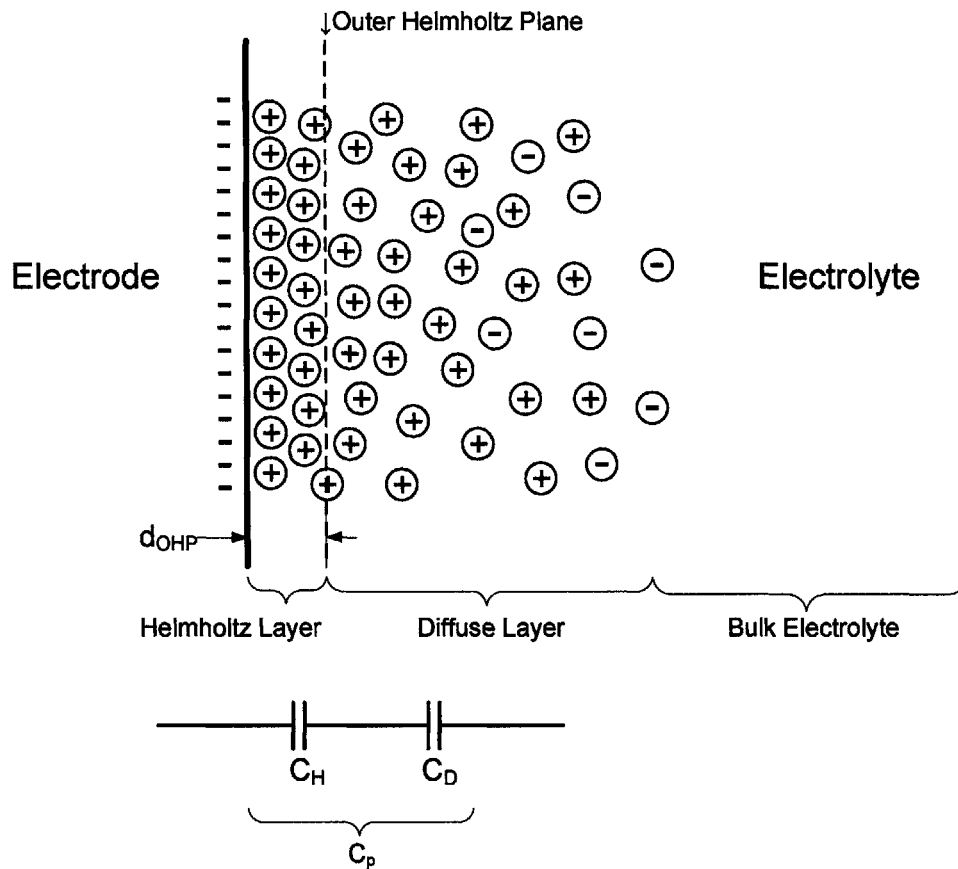


Figure 3.6: Gouy-Chapman-Stern model of the electrode-electrolyte interface.

3.2.2 Equivalent Circuit Model

The combination of the interfacial and bulk impedance can be described by the equivalent circuit shown in Figure 3.7. Intuitively, at low frequencies, the interfacial impedance of C_p and R_p is dominant and the measured capacitance and resistance is relatively constant as a function of electrode separation. At higher frequencies, the bulk impedance of C_s and R_s is dominant and the interfacial impedance can be subtracted as a constant offset. In this case, differential permittivity and conductivity measurements can simply assume a uniformly polarizable media.

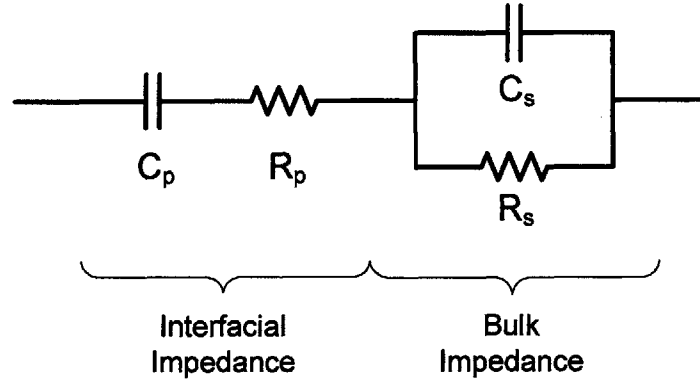


Figure 3.7: Equivalent circuit of the combined bulk and interfacial model.

A more rigorous version of the above argument can be obtained by analyzing the overall, or the measurable, impedance of the circuit shown in Figure 3.7. This impedance is described by the expression

$$Z = \frac{R_s}{1 + j\omega R_s C_s} + R_p + \frac{1}{j\omega C_p}. \quad (3.16)$$

Combining three terms into one fraction, the measured impedance becomes

$$Z = \frac{-\omega^2 R_s C_s R_p C_p + j\omega (R_s C_s + R_p C_p + R_s C_p) + 1}{j\omega C_p (1 + j\omega R_s C_s)}, \quad (3.17)$$

which can be expressed as

$$Z = \frac{R_s C_s R_p C_p (j\omega + \omega_1)(j\omega + \omega_2)}{j\omega C_p (1 + j\omega R_s C_s)}, \quad (3.18)$$

This expression has a pole at the origin, a pole at high frequency, and two zeros at intermediate frequencies. A bode plot of this impedance is shown in Figure 3.8. The location of the high frequency pole is fixed by the intrinsic properties of the sample material. Since, by definition,

$$C_s = \frac{\epsilon}{K_{cell}}, \quad (3.19)$$

$$R_s = \frac{K_{cell}}{\kappa}. \quad (3.20)$$

The product of C_s and R_s is thus,

$$R_s C_s = \frac{\varepsilon}{\kappa}. \quad (3.21)$$

For water-based solutions, the value of ε is expected to be approximately $80\varepsilon_0$ and the value of κ is expected to range between $10^{-6} S/m$ and $0.1 S/m$. The range of ε/κ is thus approximately ranges from $10^{-9} s$ and $10^{-4} s$.

In order to accurately determine C_s and R_s , the locations of the two zeros must also be known. Since the values of C_p and R_p cannot be predicted directly using the GCS model, unambiguous measurement of C_s and R_s requires finding a frequency where the effect of C_s and R_s are dramatically attenuated. Therefore, the location of the lower frequency zero is critical because below this frequency, the impedance is dominated by the interfacial capacitance C_p , and above this frequency, the impedance is dominated by the sample impedance formed by C_s and R_s . The locations of the zeros can be determined by the roots of the numerator in equation (3.17) using the quadratic formula, such that

$$\omega_{1,2} = \frac{(R_s C_s + R_p C_p + R_s C_p) \mp \sqrt{(R_s C_s + R_p C_p + R_s C_p)^2 - 4R_s C_s R_p C_p}}{2R_s C_s R_p C_p}. \quad (3.22)$$

The lower frequency zero, located at ω_1 , is given by the negative term of this expression while the higher frequency zero, located at ω_2 , is given by the positive term of this expression. An intuitive sense of the location of ω_1 can be developed by approximating the expression in (3.22) by its dominant terms. Noticing repetitions in the equation, the expression for ω_1 can be rewritten as

$$\omega_1 = \frac{p - \sqrt{p^2 - 2q}}{q} \quad (3.23)$$

where

$$p = R_s C_s + R_p C_p + R_s C_p \quad (3.24)$$

$$q = 4R_s C_s R_p C_p. \quad (3.25)$$

Manipulating equation (3.23) further, one can obtain

$$\omega_1 = \frac{p}{q} \left(1 - \sqrt{1 - \frac{2q}{p^2}} \right). \quad (3.26)$$

This expression can be replaced by the series expansion

$$(1 + \alpha)^n = 1 + n\alpha + \frac{n(n-1)}{2!} \alpha^2 + \dots \quad (3.27)$$

where

$$\alpha = -\frac{2q}{p^2}. \quad (3.28)$$

Taking the first two terms of the series allows ω_1 to be approximated as

$$\omega_1 \approx \frac{p}{q} \left(\frac{q}{p^2} \right) = \frac{1}{p}, \quad (3.29)$$

which gives the result:

$$\omega_1 \approx \frac{1}{(R_s C_s + R_p C_p + R_s C_p)}. \quad (3.30)$$

This expression is a rather intuitive result, which says that the value of ω_1 is determined by the time constant of the bulk impedance, the time constant of the interfacial impedance, and the time constant that describes the interaction between these two parts.

An approximate expression can also be derived for ω_2 , which is the positive term in equation (3.22). Since it can be shown that

$$(R_s C_s + R_p C_p + R_s C_p)^2 \gg 4R_s C_s R_p C_p, \quad (3.31)$$

the second term under the square root in equation (3.22) can be neglected. The expression for ω_2 can thus be approximated as

$$\omega_2 \approx \frac{(R_s C_s + R_p C_p + R_s C_p)}{R_s C_s R_p C_p}. \quad (3.32)$$

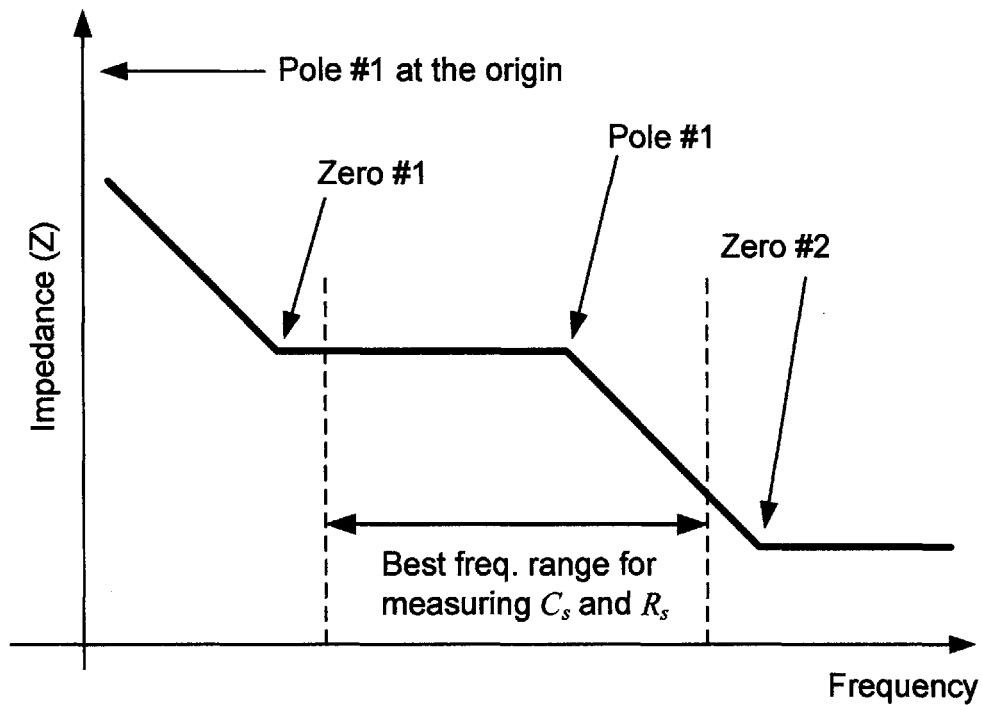


Figure 3.8: Bode plot for the combined bulk and interfacial model.

The expression for ω_1 and ω_2 can be further simplified by comparing the terms of $R_s C_s + R_p C_p + R_s C_p$. If the electrode separation is greater than the Debye length, which is typically no more than 100 nm, it can be assumed that $R_s \gg R_p$ and therefore, $R_p C_p + R_s C_p \approx R_s C_p$. The assumption of having an electrode separation greater than the

Debye length further implies that $C_p \gg C_s$ and therefore, $R_s C_s + R_s C_p \approx R_s C_p$. Finally, the expressions for ω_1 and ω_2 can be written as,

$$\omega_1 \approx \frac{1}{R_s C_p}, \quad (3.33)$$

$$\omega_2 \approx \frac{1}{C_s R_p}. \quad (3.34)$$

It is important to note that in situations where the electrode separation is less than or approximately equal to the Debye length, these assumptions no longer hold, and more sophisticated models are required to interpret the measured impedance.

The ideal frequency range for measuring the bulk impedance formed by the parallel combination of R_s and C_s , can be identified by inserting the simplified expression for ω_1 and ω_2 back into equation (3.18) for the overall impedance, which results in the expression

$$Z = \frac{R_s C_s R_p C_p \left(j\omega + \frac{1}{R_s C_p} \right) \left(j\omega + \frac{1}{C_s R_p} \right)}{j\omega C_p (1 + j\omega R_s C_s)}. \quad (3.35)$$

3.2.3 Interpretation of the Measured Impedance

The measured impedance of equation (3.35) is interpreted as a parallel combination of a capacitor and a resistor. The frequency dependence of measured values of capacitance can be determined by setting this expression equaling the impedance of a parallel capacitor and resistor such that

$$\frac{R}{(1 + j\omega RC)} = \frac{R_s C_s R_p C_p \left(j\omega + \frac{1}{R_s C_p} \right) \left(j\omega + \frac{1}{C_s R_p} \right)}{j\omega C_p (1 + j\omega R_s C_s)}. \quad (3.36)$$

This equation is analyzed at four different frequency ranges:

i. Very low frequencies: $\omega \rightarrow 0$

As $\omega \rightarrow 0$, only the pole at the origin contributes to the measured impedance.

Expression (3.36) can thus be simplified as

$$\frac{R}{(1 + j\omega RC)} = \frac{1}{j\omega C_p}. \quad (3.37)$$

Thus, in this limit, the measured impedance is dominated by the interfacial capacitance.

ii. Very high frequencies: $\omega \rightarrow \infty$

As $\omega \rightarrow \infty$, all the poles and zeros contribute to the measured impedance.

Expression (3.36) can thus be simplified as

$$\frac{R}{(1 + j\omega RC)} = R_p. \quad (3.38)$$

Thus, in this limit, the measured impedance is dominated by the interfacial resistance.

iii. Intermediate frequencies: $\omega > \omega_1$ and $\omega < \omega_2$

For frequencies between the zeros at ω_1 and ω_2 , expression (3.36) can be simplified as

$$\frac{R}{(1 + j\omega RC)} = \frac{R_s}{(1 + j\omega R_s C_s)}. \quad (3.39)$$

Within this frequency range, the measured impedance exactly corresponds to the bulk capacitance and resistance such that

$$C = C_s, \quad (3.40)$$

$$R = R_s. \quad (3.41)$$

Therefore, this is the ideal range for measuring the bulk properties of the liquid.

iv. Accounting for the zero at ω_1 :

The frequencies around ω_1 are interesting because the measured impedance transitions from the bulk impedance to the interfacial capacitance. Analysis of the measured impedance in this region that properly accounts of the zero at ω_1 , could help confirm the validity of the GCS model and estimate parameter such as C_p and R_p . One version of this result was derived by Schwan [49] using rather tenuous assumptions. A new derivation using fewer assumptions is presented here.

Accounting for the zero at ω_1 , the expression (3.36) can be simplified as

$$\frac{R}{(1 + j\omega RC)} = \frac{R_s \left(j\omega + \frac{1}{R_s C_p} \right)}{j\omega (1 + j\omega R_s C_s)}. \quad (3.42)$$

Conjugating both fractions to make the denominator real yields an intermediate expression

$$\frac{R(1 - j\omega RC)}{(1 + (\omega RC)^2)} = \frac{R_s \left(\omega - \frac{j}{R_s C_p} - j\omega^2 R_s C_s - \frac{\omega C_s}{C_p} \right)}{\omega (1 + (\omega R_s C_s)^2)}. \quad (3.43)$$

The expression for the measured capacitance can be found by equating only the imaginary part of equation (3.43), which yield the expression

$$\omega RC = \left(\frac{R_s}{R} \right) (1 + (\omega RC)^2) \frac{\left(\frac{1}{R_s C_p} + \omega^2 R_s C_s \right)}{\omega (1 + (\omega R_s C_s)^2)}. \quad (3.44)$$

This expression can be simplified as

$$C = C_s \left(1 + \frac{1}{\omega^2 R_s^2 C_s C_p} \right) \left(\frac{R_s}{R} \right)^2 \frac{(1 + (\omega RC)^2)}{(1 + (\omega R_s C_s)^2)}. \quad (3.45)$$

It can generally be assumed that the factor $\frac{(1+(\omega RC)^2)}{(1+(\omega R_s C_s)^2)}$ has a value of 1 since the value of $(\omega RC)^2$ and $(\omega R_s C_s)^2$ are approximately equal at large electrode separation. Furthermore, as shown by equation (3.21), the value of $(\omega RC)^2$ and $(\omega R_s C_s)^2$ are both smaller than 1 for the measurable frequency range of the impedance analyzer.

$$C = C_s \left(1 + \frac{1}{\omega^2 R_s^2 C_s C_p} \right) \left(\frac{R_s}{R} \right)^2. \quad (3.46)$$

This expression indicates that the measured capacitance will be magnified at low frequencies. Furthermore, the characteristic frequency, ω_c , below which the increase in the measured capacitance begins to take effect, is determined by

$$\omega_c = \frac{1}{R_s \sqrt{C_s C_p}}. \quad (3.47)$$

At large electrode separation, the value of the R_s/R factor is approximately 1 and will not affect the measured value of C . At small electrode separation, R_s can be much smaller than R , and this factor will attenuate the measured capacitance. This attenuation is counterbalanced by the magnification caused by the frequency dependent term, since the value of $R_s^2 C_s$ will decrease with increasing frequency.

The expression for the measured resistance could be determined by equating only the real part, which yields an implicit expression for R where

$$R = R_s \left(1 - \frac{C_s}{C_p} \right) \frac{(1+(\omega RC)^2)}{(1+(\omega R_s C_s)^2)}. \quad (3.48)$$

Assuming $(\omega RC)^2$ and $(\omega R_s C_s)^2$ have approximately the same value as before, this expression can be simplified down to

$$R = R_s \left(1 - \frac{C_s}{C_p} \right). \quad (3.49)$$

At large electrode gaps, $C_s \ll C_p$, and $R \approx R_s$. At small electrode gaps, however, C_s can be quite large. Therefore, the measured value of R becomes attenuated by the ratio of C_s and C_p . If the GCS model and the equivalent circuit in Figure 3.7 are correct, then this relationship may be an effective way to measure the value of C_p .

Chapter 4

Analysis

This chapter presents analysis techniques for extracting permittivity from capacitance versus electrode-displacement datasets. Since the equations describing permittivity and conductivity are exactly parallel, the techniques described here can be applied to determine of conductivity from conductance versus electrode-displacement datasets. The first three sections of this chapter describe three methods for determining the permittivity, using 1) simple least squares fitting, 2) weighted least squares fitting, and 3) non-linear fitting. The next three sections present a thorough evaluation of the robustness of the latter two techniques, in the presence of systematic and random errors, using simulated data. These evaluations enable the optimal technique to be selected based on the level of systematic and random error from experimental data.

4.1 Simple Least Squares Fitting

From the electrostatic model outlined in the previous chapter, the capacitance between spherical electrodes are described by

$$C = \pi r \epsilon_r \epsilon_0 \ln\left(\frac{2r}{\xi}\right) + C_0, \quad (4.1)$$

where ζ is the distance between nearest points on the spherical electrodes. Experimentally, ζ is determined to within an offset since only the displacement of the electrode, x , is measured. Thus, x and ζ are related by

$$\zeta = x - x_0, \quad (4.2)$$

where x_0 is the constant offset. The measured capacitance as a function of x is therefore

$$C = \pi r \epsilon_r \epsilon_0 \ln \left(\frac{2r}{x - x_0} \right) + C_0. \quad (4.3)$$

Figure 4.1 shows a simulated data set of $C(x)$ in vacuum. As discussed previously, dx/dC varies linearly with x such that,

$$-\pi r \epsilon_0 \frac{dx}{dC} = \frac{x - x_0}{\epsilon_r}. \quad (4.4)$$

Given known constants ϵ_0 , π , and r , the value of the relative permittivity, ϵ_r , can therefore be determined from a linear regression of dx/dC versus x .

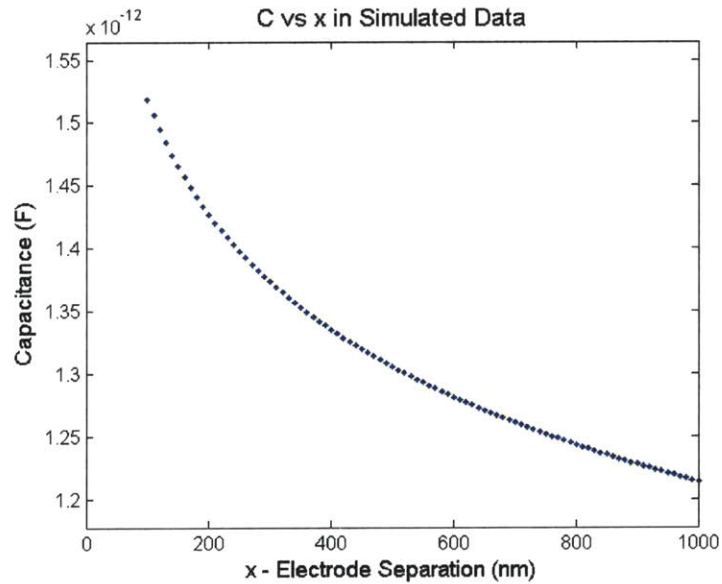


Figure 4.1: Simulated data set of $C(x)$.

The value for dx/dC can be estimated using the secant approximation,

$$\frac{dx}{dC} \approx \frac{x_{n+1} - x_n}{C_{n+1} - C_n} = \frac{\Delta x}{\Delta C}, \quad (4.5)$$

where dx/dC is evaluated at $x = (x_{n+1} + x_n)/2$. Inserting this expression into (4.4) and appropriately shifting the values of x gives,

$$-\pi r \varepsilon_0 \left(\frac{\Delta x}{\Delta C} \right) = \frac{x_n + \Delta x/2 - x_0}{\varepsilon_r}. \quad (4.6)$$

At this point, it is convenient to define the left hand side expression as a new variable y ,

$$y \equiv -\pi r \varepsilon_0 \left(\frac{\Delta x}{\Delta C} \right). \quad (4.7)$$

The relationship between y and x can thus be described by the equation,

$$y = \frac{x_n + \Delta x/2 - x_0}{\varepsilon_r}. \quad (4.8)$$

The variable y has units of length. In fact, when $\varepsilon_r = 1$, y is exactly equal to $\xi + \Delta x/2$. Since $\Delta x/2$ is known, the absolute electrode separation, ξ , can be determined. Figure 4.2 shows the plot of y versus x for a simulated $C(x)$ dataset where $\varepsilon_r = 1$. The value of ε_r is the inverse slope of this plot and can be determined using a linear least squares fit to the equation

$$y = a + bx. \quad (4.9)$$

From the parameters b and a , the value of ε_r and x_0 are determined by

$$\varepsilon_r = \frac{1}{b}, \quad (4.10)$$

$$x_0 = \frac{\Delta x}{2} - a \cdot \varepsilon_r. \quad (4.11)$$

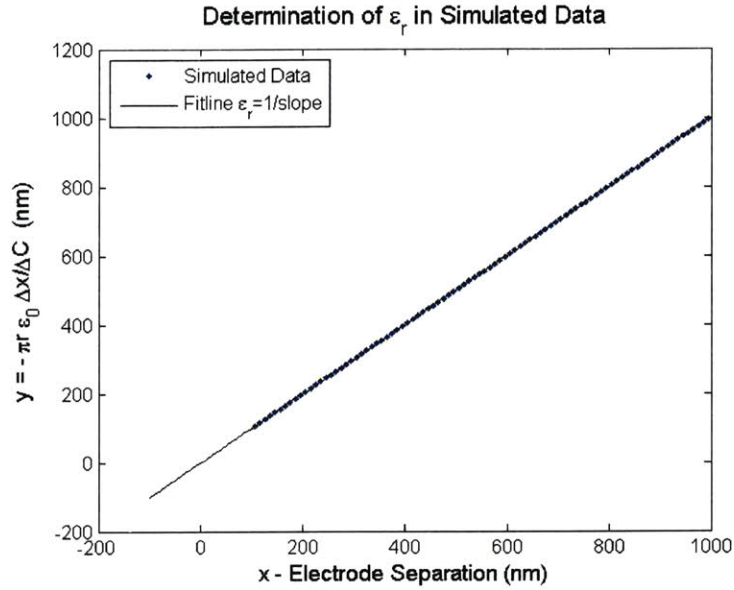


Figure 4.2: Transformed data set of $y(x)$ where ϵ_r can be determined from the inverse of the slope.

The fitting procedure described above completes a basic level analysis for determining the relative permittivity. There are two important observations from this analysis: The first is that the determination of permittivity is independent of scale factors of x . Since the variable x is found on both sides of equation (4.6), constant multipliers of x do not affect the measured slope. Therefore, provided that the measurement of x is itself linear, the determination of the permittivity is calibrated by the radius of the sphere, which is known to high accuracy. This arrangement illustrates the determination of the absolute permittivity based on calibration by the radius of a spherical electrode.

The second observation is that the expression for y presents an interesting method for measuring the absolute separation between two spheres or a sphere and a plane with high accuracy. If the value of ϵ_r is known, ξ can be determined from y without offset. Therefore, the value of the absolute separation can be determined exactly by a controlled modulation of the electrode separation. This technique can potentially be applied to

determine the absolute separation between precision surfaces, which can be used for feedback control of air bearings and levitating platforms.

4.2 Weighted Least Squares (WLS) Fitting

One of the underlying assumptions of least squares fitting is that the standard deviation of the error is constant for all data points. This assumption does not hold for y since y is a function of the differential values of x and C . At larger electrode separations, ΔC is relatively small, and the standard deviation of the error in C is relatively large. Conversely, at small electrode separations, ΔC is relatively large, and the standard deviation of the error in C is relatively small.

The effect of non-constant standard deviation can be compensated using weighted least squares (WLS) fitting, where a weight function to give more weight to data points with greater certainty, or smaller standard deviation, σ_y , and less weight to data points with less certainty. Specifically, the weight function is defined as

$$w = 1/\sigma_y^2. \quad (4.12)$$

The standard deviations of y , or σ_y are related to the standard deviation of Δx and ΔC , *i.e.* $\sigma_{\Delta x}$ and $\sigma_{\Delta C}$, by their partial derivatives as

$$\sigma_y^2 = \left(\frac{\partial y}{\partial \Delta C} \right)^2 \sigma_{\Delta C}^2 + \left(\frac{\partial y}{\partial \Delta x} \right)^2 \sigma_{\Delta x}^2. \quad (4.13)$$

Assuming the random errors of x and C are uncorrelated:

$$\sigma_{\Delta C}^2 = 2\sigma_C^2 \quad (4.14)$$

$$\sigma_{\Delta x}^2 = 2\sigma_x^2. \quad (4.15)$$

The partial derivatives of y from Equation (4.7) can be computed as,

$$\frac{\partial y}{\partial \Delta C} = \frac{\pi r \epsilon_0}{(\Delta C)^2} = -\frac{y}{\Delta C} \quad (4.16)$$

$$\frac{\partial y}{\partial \Delta x} = -\frac{\pi r \epsilon_0}{\Delta C} = \frac{y}{\Delta x}. \quad (4.17)$$

Therefore,

$$\sigma_y^2 = 2y^2 \left(\left(\frac{\sigma_C}{\Delta C} \right)^2 + \left(\frac{\sigma_x}{\Delta x} \right)^2 \right). \quad (4.18)$$

This equation confirms that the variance of y is a composite of the variance of ΔC and the variance of Δx . Since Δx is kept constant in a typical measurement, the second term inside the parentheses is constant while ΔC varies with electrode separation. Since the ΔC increases with increasing electrode separation, the first term inside the parentheses is expected to dominate at larger separations, while the second term is expected to dominate at small electrode separations. The threshold value of ξ , or ξ^* , when the contributions from these two terms are equal can be determined by setting the first and second terms equal to one another:

$$\frac{\sigma_C}{\Delta C} = \frac{\sigma_x}{\Delta x}. \quad (4.19)$$

Using the model for C from equation (4.3), ΔC can be expanded as

$$\Delta C = C(x_{n+1}) - C(x_n) = \pi \epsilon_0 r \ln \left(\frac{x_{n+1} - x_0}{x_n - x_0} \right) = \pi \epsilon_0 r \ln \left(1 + \frac{\Delta x}{x_n - x_0} \right). \quad (4.20)$$

This expression can be further simplified by taking the first term of the series expansion for $\ln(1 + \alpha)$,

$$\Delta C \approx \pi \epsilon_0 r \left(\frac{\Delta x}{x_n - x_0} \right). \quad (4.21)$$

The expression in (4.19) thus becomes

$$\frac{\sigma_C (x_n - x_0)}{\pi \epsilon_0 \epsilon_r r \Delta x} = \frac{\sigma_x}{\Delta x} \quad (4.22)$$

Since $\xi = x - x_0$, the threshold value of ξ^* has the expression

$$\xi^* = \pi \epsilon_0 \epsilon_r r \frac{\sigma_x}{\sigma_C}, \quad (4.23)$$

The value of ξ^* can be estimated for the apparatus presented in Chapter 2, where known constants include: $r = 4.7625 \times 10^{-3} m$ and $\epsilon_0 = 8.85 \times 10^{-12} F \cdot m^{-1}$. The specified σ_x for the capacitance probes is 0.2 nm, although, thermal fluctuations will likely increase this value. For the purpose of this calculation, the value of σ_x will be estimated at 1 nm. The specification for σ_C from the impedance analyzer is 0.1% of C , which for air where $\epsilon_r = 1$ and $C \approx 10^{-12} F$, the value of σ_C will approximately be $10^{-15} F$. The value for ξ^* is thus

$$\xi^* = 132 nm. \quad (4.24)$$

Since the value of ξ^* is relatively small, it can be concluded that the contribution from the first term inside the parentheses are dominant over the second term, *i.e.*

$$\left(\frac{\sigma_C}{\Delta C} \right)^2 \gg \left(\frac{\sigma_x}{\Delta x} \right)^2. \quad (4.25)$$

Therefore, σ_y can simply be determined from

$$\sigma_y^2 = 2 \left(\frac{y}{\Delta C} \right)^2 \sigma_C^2 \quad (4.26)$$

and the weight function is thus,

$$w_i = \frac{1}{2\sigma_C^2} \left(\frac{\pi\epsilon_0 r \ln \left(\frac{x_{n+1} - x_0}{x_n - x_0} \right)}{y} \right)^2. \quad (4.27)$$

Since the value of x_0 is initially unknown, an initial guess for x_0 can be obtained by from the result of a simple linear regression. Improved estimates of x_0 can then be obtained by iterative application of the weighted least squares fit. Typically three iterations are enough to converge on a value of x_0 to within 1 nm.

WLS fitting only makes sense in the presence of noise. This effect can be included in simulated capacitance and displacement data by adding random variables, C_E and x_E . Both random variables have Gaussian distributions with zero mean and standard deviations, σ_C and σ_x . The expression for the measured capacitance is therefore,

$$C = \pi r \epsilon \ln \left(\frac{2r}{\xi} \right) + C_0 + C_E. \quad (4.28)$$

where

$$\xi = x - x_0 + x_E, \quad (4.29)$$

A WLS fit to simulated noisy data compared to a simple least squares fit is shown in Figure 4.3, where the fitted line shows significantly better estimate of the slope. In order to ensure the validity of the weight function, the weighted residue from the fitting is shown in Figure 4.4, where the weighted residue is defined as,

$$R_e = \frac{\sum_i \sqrt{w_i} (y_i - \hat{b}x_i)}{\sum_i \sqrt{w_i}}. \quad (4.30)$$

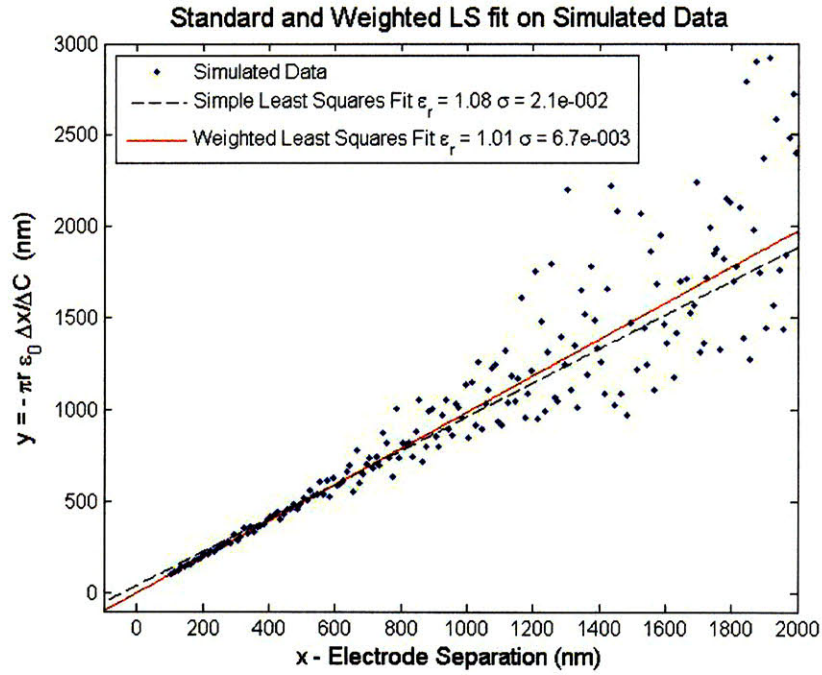


Figure 4.3: Simple and weighted least squares fitting on noisy data. C_e is distributed uniformly with an amplitude of 5×10^{-16} F.

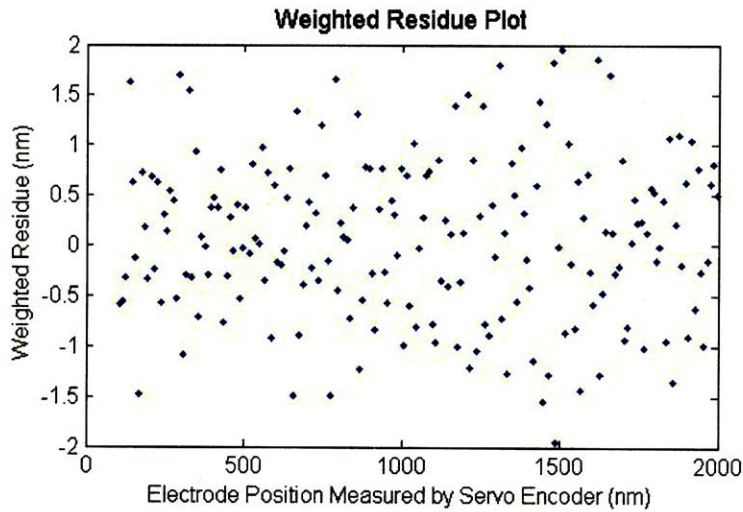


Figure 4.4: Weighted residue plot from weighted least squares fitting.

The accuracy of the fitting for ϵ_r and x_0 can be estimated using standard statistical formulae with modifications for the weight function. Starting with the formula for the estimated standard deviation of the slope, b ,

$$\widehat{\sigma}_b = \frac{s_e}{\sqrt{S_{xx}}}. \quad (4.31)$$

The value of the standard error S_e can be estimated using,

$$s_e = \sqrt{\frac{SSE}{n-2}} \quad (4.32)$$

$$SSE = S_{yy} - S_{xy}^2 / S_{xx} \quad (4.33)$$

$$S_{xx} = \frac{\sum w_i x_i^2}{\sum w_i} - \frac{(\sum x_i \sqrt{w_i})^2}{n \sum w_i} \quad (4.34)$$

$$S_{xy} = \frac{\sum w_i x_i y_i}{\sum w_i} - \frac{(\sum x_i \sqrt{w_i})(\sum y_i \sqrt{w_i})}{n \sum w_i} \quad (4.35)$$

$$S_{yy} = \frac{\sum w_i y_i^2}{\sum w_i} - \frac{(\sum y_i \sqrt{w_i})^2}{n \sum w_i} \quad (4.36)$$

Since ε_r and the slope of y versus x , b are related as,

$$\varepsilon_r = \frac{1}{b}. \quad (4.37)$$

The standard deviation of the estimated relative permittivity is therefore,

$$\widehat{\sigma}_{\varepsilon_r} = \frac{\widehat{\sigma}_b}{b^2} = \frac{s_e}{b^2 \sqrt{S_{xx}}}. \quad (4.38)$$

The standard deviation of the estimate for the intercept, a , is

$$\widehat{\sigma}_a = \frac{\widehat{s}_e}{\sqrt{n}}, \quad (4.39)$$

Therefore, since

$$x_0 = -\frac{a}{b} = -a\varepsilon_r, \quad (4.40)$$

the standard deviation of x_0 can therefore be estimated as,

$$\widehat{\sigma}_{x_0} = \sqrt{\widehat{\sigma}_a \varepsilon_r + \widehat{\varepsilon}_r a} = \sqrt{\frac{s_e^2 \varepsilon_r}{n} + \frac{s_e^2 a}{b^4 S_{xx}}}. \quad (4.41)$$

4.3 Non-Linear (NL1) Fitting

One of the inaccuracies of the previous analyses is the estimate of dx/dC using the secant approximation. This inaccuracy can be avoided by using an exact expression for the difference between C_n and C_m . From Equation (4.3), this expression becomes

$$C_n - C_m = \pi r \varepsilon_0 \varepsilon_r \left[\ln \left(\frac{2r}{x_n - x_0} \right) - \ln \left(\frac{2r}{x_m - x_0} \right) \right], \quad (4.42)$$

which simplifies to

$$C_n - C_m = \pi r \varepsilon_0 \varepsilon_r \ln \left(1 + \frac{x_m - x_n}{x_n - x_0} \right). \quad (4.43)$$

In order to determine ε_r , pairs of x_n and x_m are transformed as the right hand side of equation (4.43) (without the ε_r term) and then, plotted against corresponding pairs of C_n and C_m . The value of ε_r can then be determined from a standard least squares fit for the slope. The value of x_0 cannot be simply determined from the intercept as before. Instead, the value of x_0 is optimized to produce the minimum fitting error. Starting from an initial guess for x_0 , this optimization involves applying the fitting procedure repeatedly over a range of x_0 values until a minimum is found. The plot of the RMS fitting error versus the values for x_0 for a simulated dataset is shown in Figure 4.5. Once the optimum value of x_0 has been determined, the fitting procedure is applied again to determine the value of ε_r as shown in Figure 4.6.

This approach for determining ε_r is equivalent to a non-linear fitting of $C(x)$ to Equation (4.3), that optimizes for the parameters x_0 and ε_r . The parasitic capacitance, C_0 , is assumed to be constant between x_n and x_m . The choice of m and n has important consequences for the accuracy of the fitted result. If minimum systematic errors are desired then m and n should be selected as close as possible in order to limit the error caused by the variation of C_0 . In this case, m and n should be selected as consecutive values. If minimum random errors are desired, then, m and n should be kept farther apart. Since this work is more concerned with systematic errors, the first technique will be discussed further in the following sections. From here on, this method shall be known as the method NL1.

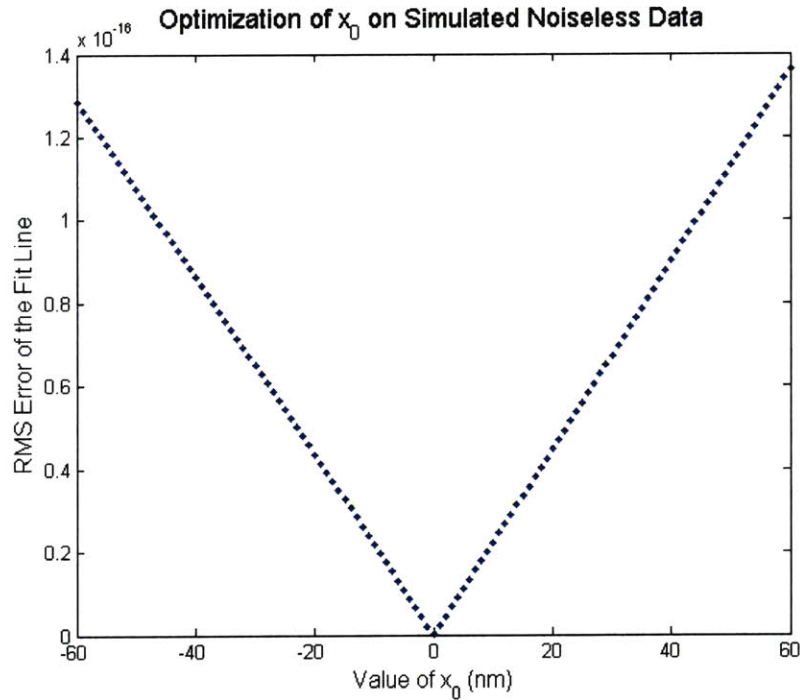


Figure 4.5: Variation of RMS fit error as a function of x_0 for simulated noiseless data.

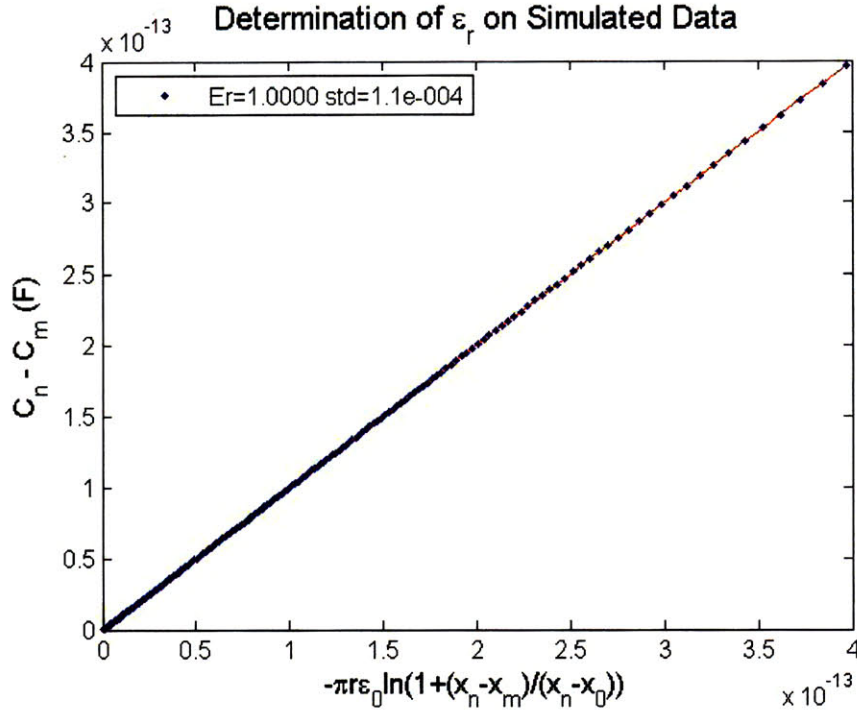


Figure 4.6: Least squares fitting to the transformed domain using simulated, noiseless data.

4.4 Errors Caused by the Electrode Mounting Shaft

The error produced by the shape of the electrode mounting shaft can be modeled as an additional parallel-plate capacitor as shown in Section 3.1.2 from equations (3.7) and (3.8). The surface area of the electrode is approximately 46 mm^2 . The distance between the parallel-plate electrodes is approximately 2.5 mm and is modulated with the change in electrode separation. The effect of this error signal on the determination of ϵ_r from both WLS and NL1 analysis will be discussed in this section.

Qualitatively, since the capacitance between the mounting shafts is significantly smaller than the capacitance between spherical electrodes, the effect of the mounting shaft is expected to play a larger role at larger electrode gaps. Since ϵ_r is estimated from a range of capacitance and displacement values, the error in ϵ_r is expected to be larger if data points are collected over a wider range of electrode gaps.

The effect of the mounting shaft on noiseless data is simulated using equation 3.7 and 3.8 for $\varepsilon_r = 1$ and electrode separations ranging from 1 μm to 35 μm incremented in steps of 0.5 μm . The WLS fitting algorithm is applied to the simulated data and obtained an ε_r value of 1.010 as shown in Figure 4.7. Although it is difficult to see the error from this figure, the simulated data show a slight droop from the fitting line at larger electrode separations. The residue plot indicate this error more clearly in Figure 4.8 as the difference between data and the fit line becomes increasingly negative at larger electrode gaps. It is interesting to note that at smaller electrode gaps, the residual error between data and the fit line becomes positive. This phenomenon is a result of the secant approximation for the derivative which produces a larger error at smaller gaps as $C(x)$ becomes more curved.

The NL1 fitting algorithm has also been applied to the same noiseless data set with results shown in Figure 4.9. The relative permittivity determined by NL1 show significantly smaller errors than the WLS case. This result is surprising since neither NL1 nor WLS analysis takes into account the shape of the electrode mounting shaft. The likely explanation for the error reduction is that NL1 analysis applies even more weight on data points from smaller gaps than larger gaps, as shown by the distribution of data points in Figure 4.9. Consequently, errors from the electrode mounting shaft, which are more pronounced at larger electrode gaps, are suppressed. The consequence of a fitting algorithm that is more heavily weighted towards smaller electrode gaps is its sensitivity to errors in those data points. This point will be discussed in more detail in the next two sections.

The value of ϵ_r determined using both WLS and NL1 analysis, as a function of data range is shown in Figure 4.10. The simulated noiseless datasets are generated with a starting electrode separation of 1 μm and data points spaced every 0.5 μm . The final value of the electrode separation ranges from 5 μm to 35 μm . The result of NL1 analysis show very little error compared to that of WLS analysis. The value of ϵ_r determined using WLS behaved predictably with the error increasing at larger data ranges eventually reaching a 1% error at 35 μm separation. This curve can be used to compensate for the errors from experimental data.

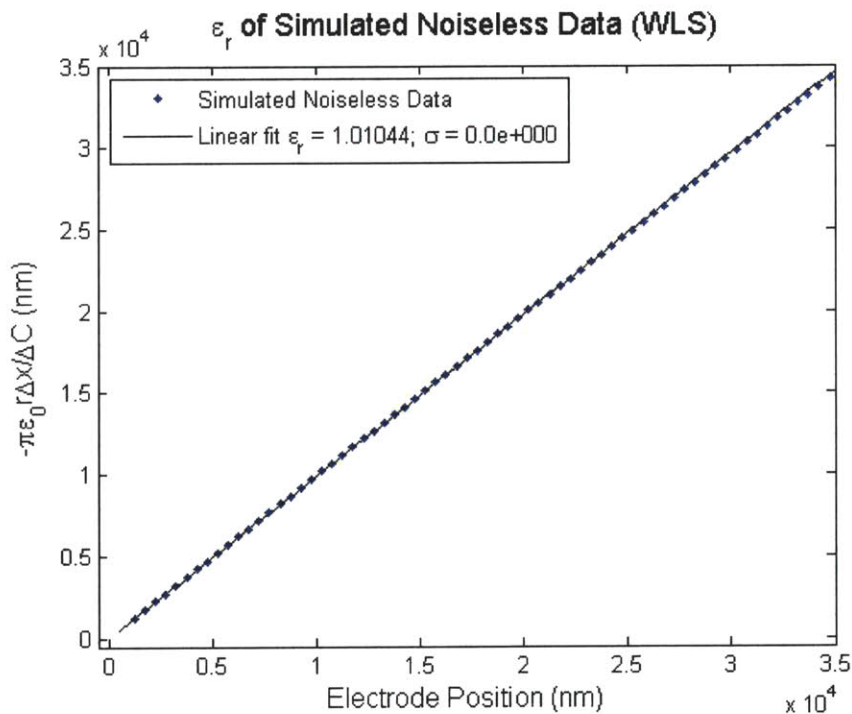


Figure 4.7: WLS analysis of simulated noiseless data with errors caused by the electrode mounting shaft.

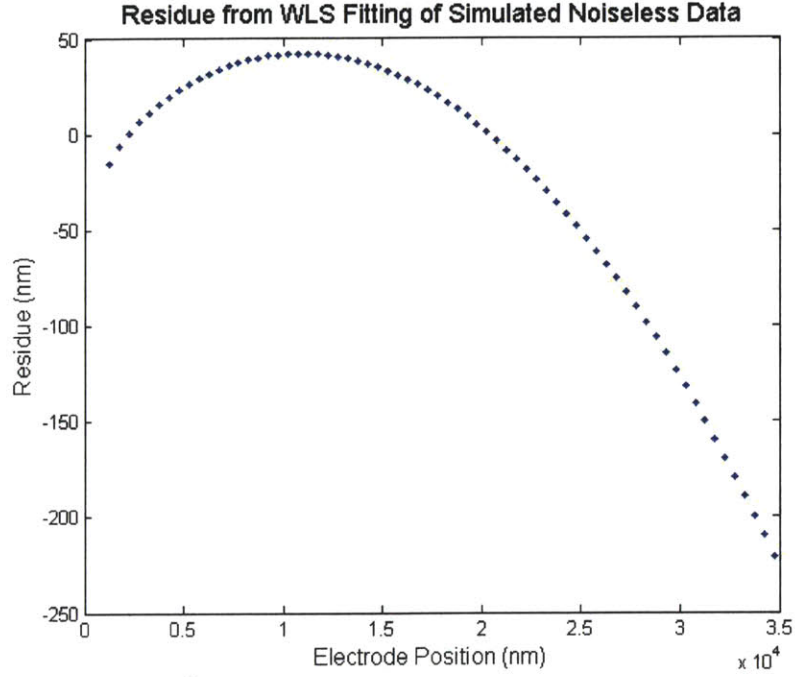


Figure 4.8: Residue from WLS fitting of simulated noiseless data with errors caused by the electrode mounting shaft.

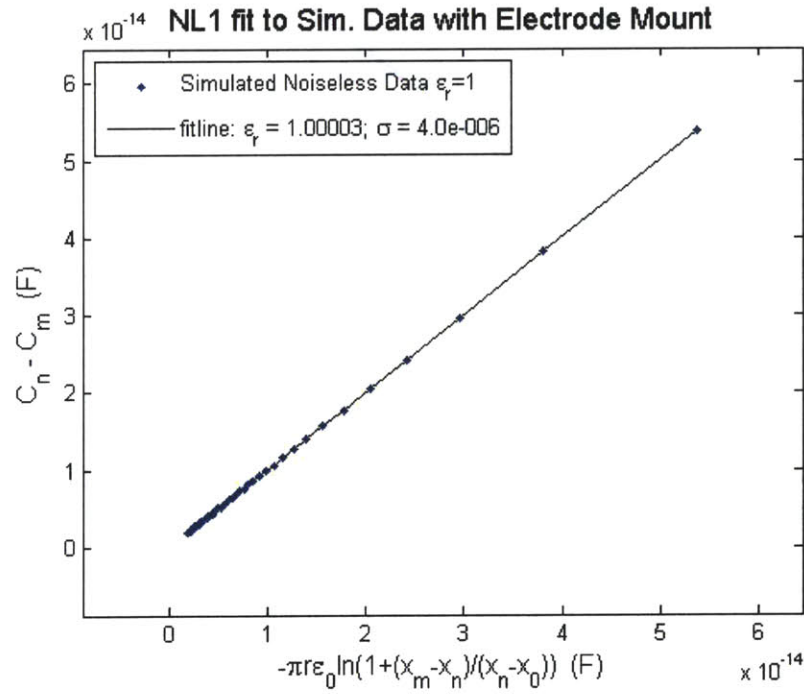


Figure 4.9: NL1 analysis of simulated noiseless data with errors caused by the electrode mounting shaft.

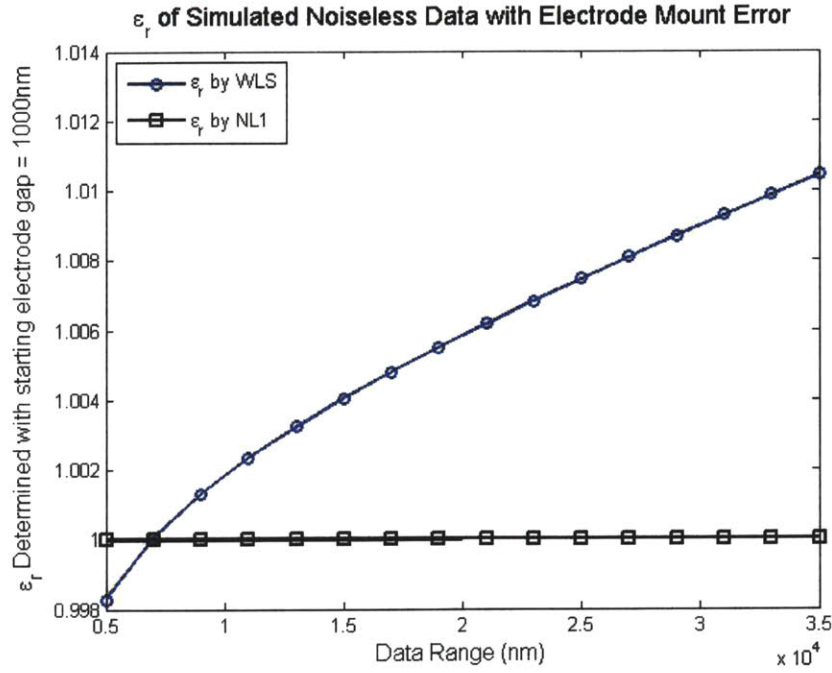


Figure 4.10: The value of ϵ_r as a function of data range determined using WLS and NL1 analysis.

4.5 Sensitivity to Noise

4.5.1 Sensitivity to Capacitance Noise

The sensitivity of both WLS and NL1 analysis to capacitance measurement noise is studied using simulated data. The simulated dataset, $C(x)$, is generated using the equation

$$C = \pi r \epsilon_0 \epsilon_r \ln\left(\frac{2r}{x}\right) + C_E. \quad (4.44)$$

In this simulation, $\epsilon_r = 1$ and the value of x has a range 35 μm with one data point every 0.5 μm . The C_E term is a simulated Gaussian noise source with zero mean and a standard deviation, $\sigma_C = 1 \times 10^{-16}$ F. WLS and NL1 analyses are applied to 40 randomly generated datasets, where the values of ϵ_r are plotted in Figure 4.11. The mean for ϵ_r from

both analysis techniques is approximately 1.00 as expected. The standard deviation from WLS analysis is 9.7×10^{-4} , while the standard deviation from NL1 analysis is approximately twice as high at 2.5×10^{-3} .

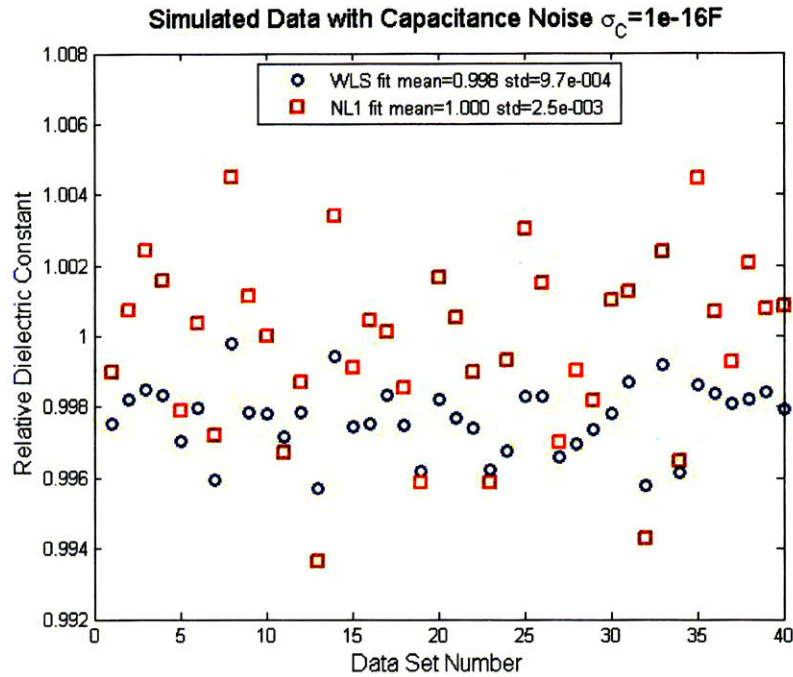


Figure 4.11: Determination the relative permittivity using WLS and NL1 techniques from 40 sets of simulated noisy impedance data. Noise on the impedance data is simulated as a normal distribution where $\sigma_C = 3 \times 10^{-16}$ F. The range of the simulated data is $15 \mu\text{m}$ collected in steps of $0.5 \mu\text{m}$.

The standard deviation of ϵ_r for each $C(x)$ dataset for both WLS and NL1 analysis are estimated using the procedures outlined in Section 4.2 and 4.3 respectively. The results are shown in Figure 4.12. For WLS analysis, the average of the estimated standard deviation of ϵ_r is 2.4×10^{-3} . The estimated value is approximate 2.5 times the actual standard deviation from 40 simulated $C(x)$ datasets shown in Figure 4.11. The factor of 2.5 is consistent for different values of σ_C , which implies that the estimated standard deviation from WLS analysis is a good predictor of the actual standard deviation of ϵ_r .

For NL1 analysis, the average of the estimated standard deviation of ε_r is 1.9×10^{-3} . This value is deceptively close to the actual standard deviation of 2.5×10^{-3} . However, the estimated standard deviation of ε_r for NL1 analysis does not scale with different values of σ_C . This is likely a result of the optimization based on minimum fitting error. Since the estimated standard deviation of ε_r in NL1 analysis is a measure of the quality of the optimization, the estimated standard deviation may be quite low despite incorrect values of ε_r and x_0 . As a result, the estimated standard deviation from NL1 analysis is not a good predictor of the actual standard deviation of ε_r .

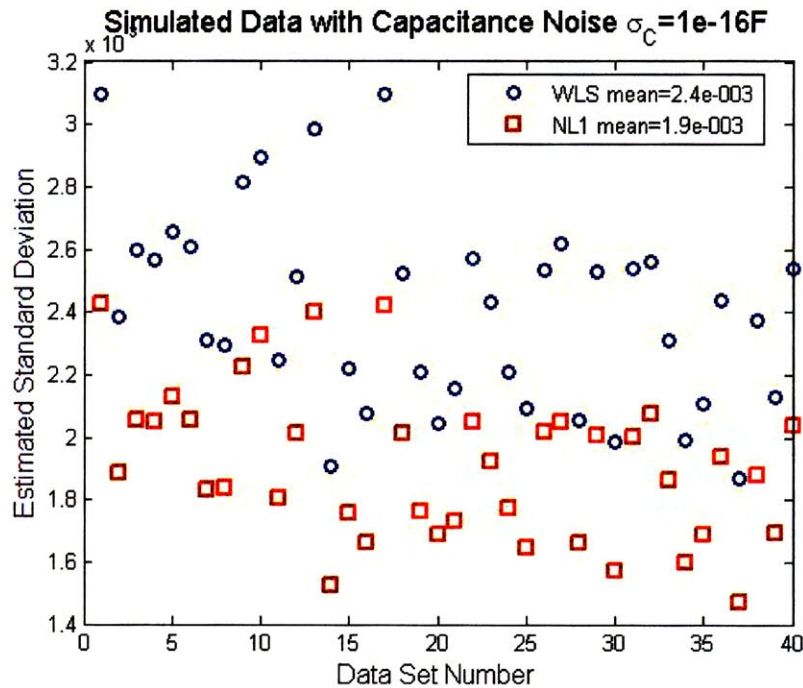


Figure 4.12: Estimated standard deviation of the previous relative permittivity measurements by WLS and NL1 techniques.

4.5.2 Sensitivity to Electrode Position Noise

The sensitivity of both WLS and NL1 analysis to electrode position noise is studied using simulated datasets for $C(x)$ generated as before, with the x values used in fitting modified as,

$$\hat{x} = x + x_E . \quad (4.45)$$

The error term, x_E , is simulated as a Gaussian distribution with zero mean and a standard deviation, $\sigma_x = 2nm$. WLS and NL1 analyses are applied to 40 randomly generated datasets, where the measured value of ε_r are plotted in Figure 4.13. As in the previous case of for capacitance noise, the mean of ε_r is approximately 1. The standard deviation of the results determined by WLS is 2.3×10^{-3} , while the standard deviation determined by NL1 is approximately twice as much at 5.2×10^{-3} . The estimated standard deviation of each dataset is shown in Figure 4.14. In this case, the mean of the estimated standard deviation for WLS is 8.7×10^{-4} , which is approximately 2.5 times the actual standard deviation determined from the fitting results. The estimated standard deviation from NL1 is 7.7×10^{-4} , which is significantly smaller than the actual standard deviation. This is reflective of the fact that optimizations of NL1 analysis may optimize to the incorrect values of ε_r and x_0 , which is not reflected by the estimated standard deviation.

Therefore, based on the simulations shown, the WLS analysis is more robust to position noise than NL1 analysis. Furthermore, the estimated standard deviation from WLS analysis is a good predictor of the actual standard deviation, whereas the equivalent parameter in NL1 analysis is not.

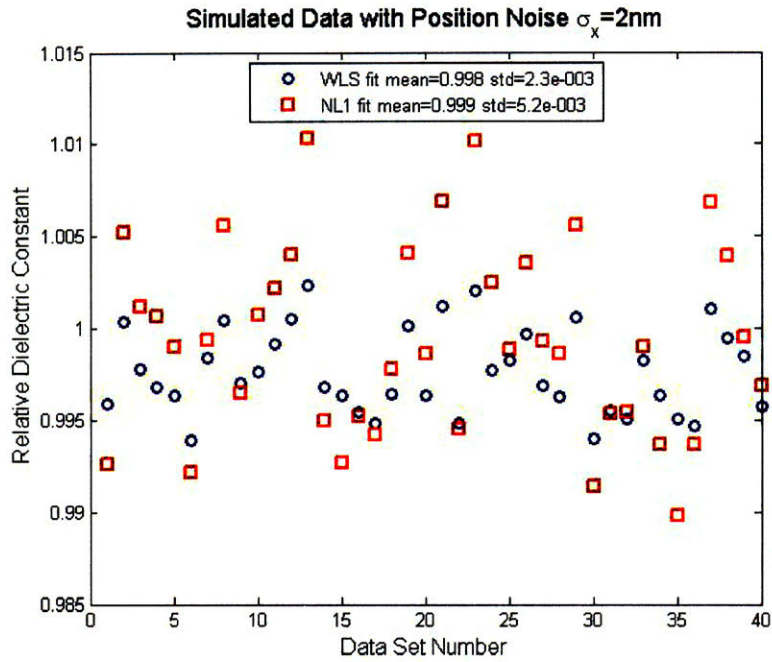


Figure 4.13: Determination of the relative permittivity using WLS and NL1 techniques from 40 sets of simulated noisy data. Noise on the electrode position, x , is simulated as a normal distribution with zero mean and $\sigma_x = 2$ nm. No noise is assumed on the capacitance measurement.

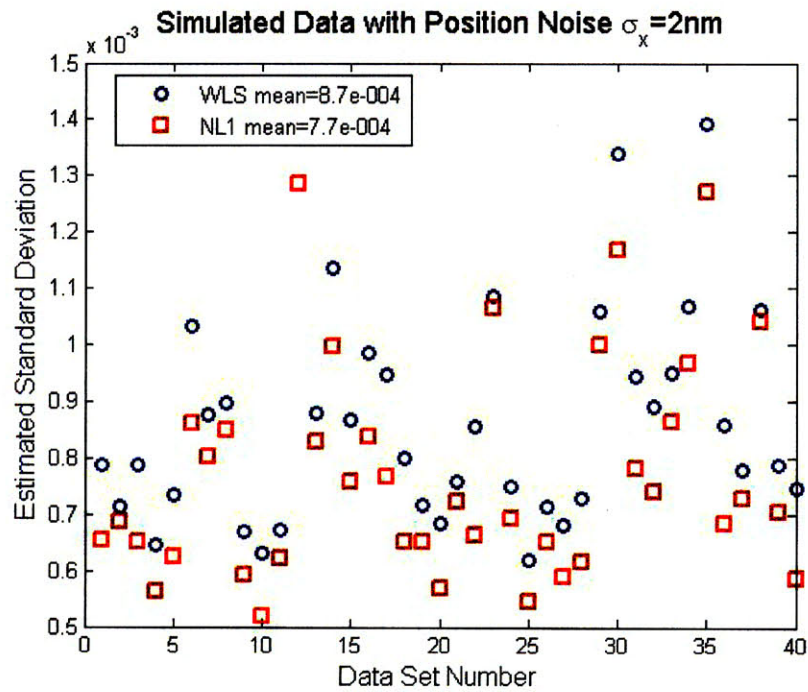


Figure 4.14: The estimated standard deviation of each simulated data set. Noise on the electrode position, x , is simulated as a normal distribution with zero mean and $\sigma_x = 2$ nm. No noise is assumed on the capacitance measurement.

4.5.3 Comparison of Noise Sensitivity

The analysis of both WLS and NL1 techniques from the two previous sections using 40 simulated random data sets are repeated at different values of σ_C and σ_x to study the trend of in the determination of ϵ_r . The standard deviations of ϵ_r plotted as a function of σ_C and σ_x are shown in Figure 4.15 and Figure 4.1. These graphs clearly indicate that the NL1 analysis is more sensitive to both capacitance noise and displacement noise. The effect is more pronounced with displacement error where the noise sensitivity is approximately three times higher in NL1 than WLS.

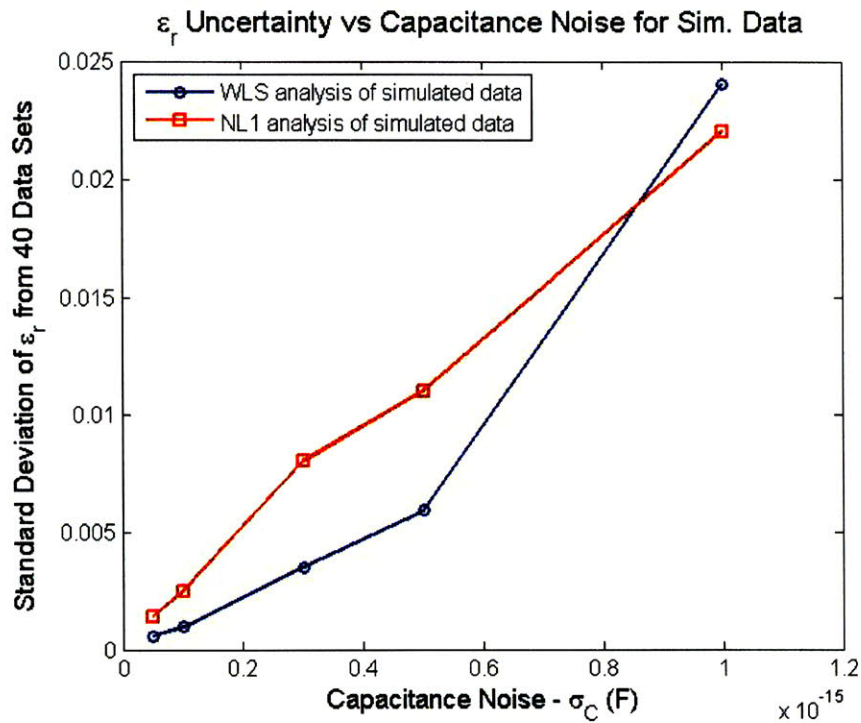


Figure 4.15: Standard deviation of ϵ_r from 40 data sets with simulated capacitance noise. The capacitance noise is normally distributed with standard deviation, σ_C plotted along the x-axis.

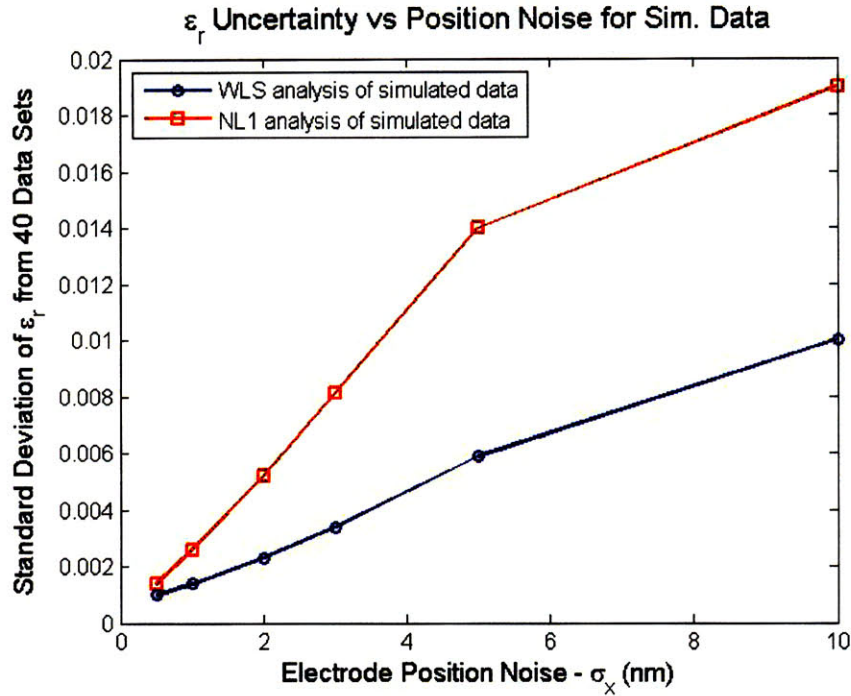


Figure 4.16: Standard deviation of ϵ_r from 40 data sets with simulated electrode position noise. The position noise is normally distributed with standard deviation, σ_c plotted along the x-axis.

4.6 Summary of Data Analysis Techniques

This chapter has presented analysis techniques designed to determine permittivity and conductivity from capacitance versus displacement and conductance versus displacement datasets. The effectiveness of WLS and NL1 fitting methods has been evaluated. NL1 fitting was found to be more immune to systematic errors caused by the shape of the electrode mounting apparatus which deviates from the shape of ideal spheres. WLS fitting has been found to be more robust to random errors from the measurement of electrical impedance and electrode position. Therefore, in a low noise environment, NL1 fitting is more desirable, whereas in a high noise environment, WLS fitting is more desirable. Ultimately, WLS fitting may more suitable in future designs of

the impedance test cell where the electrode mounting apparatus could be better designed to more closely approximate the shape of an ideal sphere.

Chapter 5

Results

This chapter presents permittivity and conductivity measurements of various substances in order to demonstrate the capabilities of the instrument and to evaluate the accuracy of the new measurement technique developed in this thesis. First, measurements of the permittivity of nitrogen gas at atmospheric are presented to study the capabilities of the instrument in a simple gaseous medium. Then, measurements of the permittivity of methanol are presented to study the capabilities of the instrument in liquid media and demonstrate its capabilities of measuring permittivity of different media without calibration. These results are followed by permittivity measurements of 2-propanol and water as further confirmation of the ability of the instrument to make accurate measurements of substances with different permittivity. Next, the conductivity of potassium chloride (KCl) solutions is presented to study the capabilities of the instrument to study conductivity. The penultimate section presents measurements of permittivity and conductivity of KCl solutions at different frequencies. The last section presents the measurements of nanometer electrode gaps in air and surface roughness models that help explain some of the results.

5.1 Permittivity of Nitrogen Gas

Nitrogen gas at atmospheric pressure is an ideal media for initial measurements since it is uniformly polarizable over a wide frequency range, and it has a well-know permittivity and negligibly low conductivity. Since the technique presented in this thesis is designed to be accurate within 1%, these measurements are not expected to be able to distinguish between nitrogen gas and vacuum, which have permittivity values of 1.00055 and 1.00000 respectively. Although air has similar properties as nitrogen, nitrogen gas is used to control the humidity inside the sample chamber in order to prevent condensation from forming. The measured signal for nitrogen gas is expected to show more scatter than liquid media since the permittivity is low and the measured capacitance is relatively small, which means that the impedance signal is more easily affected by electrical interference.

Although, the permittivity of nitrogen gas is not significantly dependent on temperature, the measurement apparatus is temperature controlled at 18°C in order to limit the errors caused by thermal expansion. The measurements are made starting at a large electrode gap, typically 35-40 μm , and decremented in steps of approximately 250 nm until the electrodes come into contact with one another. The impedance is measured after each adjustment, waiting appropriately 1 second for the positioning mechanism to settle to its final position. The excitation signal is a sinusoidal source with RMS amplitude of 500 mV. The excitation frequency is 120 kHz. This frequency is chosen because it is least affected by nearby electronic interference sources, of which the most prominent source is the PWM signal from the servomechanical actuator.

The measured resistance as a function of electrode separation is shown in Figure 5.1. The electrode displacement measurement has been zeroed at the last data point of x . Before the electrodes come into contact with one another, the resistance values show a large negative value. This is not the actual resistance of nitrogen gas, but an artifact of the measurement apparatus and the impedance analyzer. The impedance analyzer measures the resistive and reactive component of impedance as in-phase and quadrature voltage signals. When the test impedance is entirely resistive or entirely reactive, the complementary signal has zero amplitude. As a result, the signal measured by the impedance analyzer is dominated by stray impedances and leakage currents from the connectors, cabling, and internal electronics of the analyzer.

The capacitance versus electrode displacement data is shown in Figure 5.2. As the electrodes are advanced closer to one another, the capacitance increases as predicted by the model of equation (4.3). After the electrodes come into contact, the impedance becomes purely resistive, and the measured capacitance increases sharply, before lowering to a negative value. The negative capacitance is also not the actual capacitance, but rather an artifact of the impedance measurement.

The flexure stage can continue to be advanced even after the electrodes begin conducting. These displacements likely result from compression of mechanical components between the capacitance probes, such as the electrodes and mounting posts. Further compression will eventually create defects in the electrode where pieces of the platinum film will delaminate from the silicon-nitride spheres.

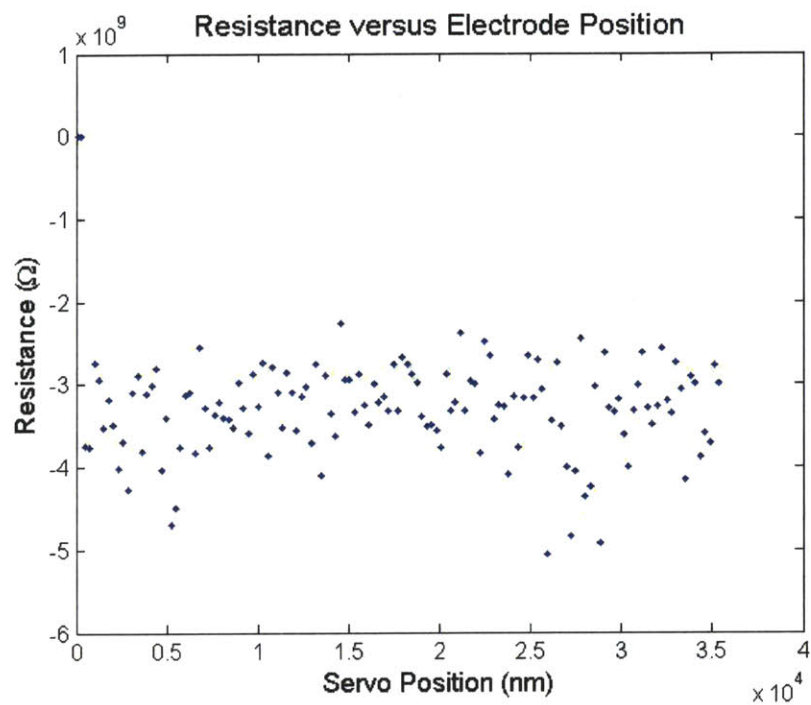


Figure 5.1: Resistance versus electrode position in nitrogen gas.

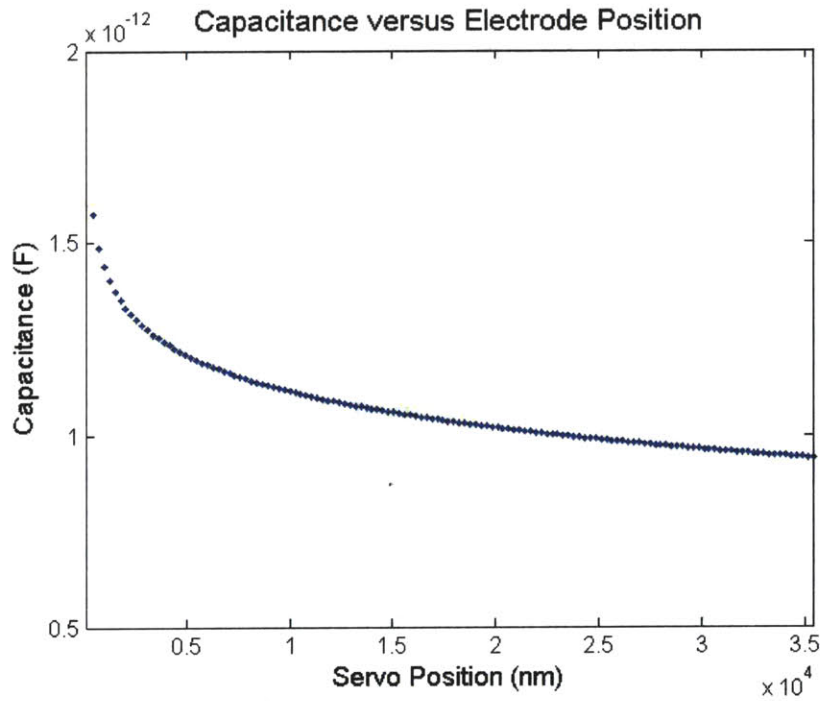


Figure 5.2: Capacitance versus electrode position in nitrogen gas.

The relative permittivity of nitrogen gas is determined using the WLS analysis described in Section 4.2. As shown in Figure 5.3, the electrode displacement, x , is plotted along the horizontal axis. The quantity y , defined in equation (4.7), is plotted along the vertical axis. As predicted by the model, the data points lie on a straight line and the relative permittivity is the inverse of the slope. As expected from the model of the measurement uncertainty, data points from larger electrode gaps show more scatter since ΔC is smaller for each Δx . The data points at larger electrode separations also show a slight droop from the fitted straight line. This droop is a result of the errors caused by the electrode mounting shaft.

Only a portion of the full data set is used for WLS fitting. Data from electrode gaps smaller than $1\ \mu\text{m}$ are excluded to avoid incorrect measurements caused by trapped particles. Data from larger electrode gaps, beyond $35\ \mu\text{m}$ are also excluded in order to maintain a consistent range of data for estimating the permittivity. There are some significant outliers at larger electrode gaps. These data points are measured while the tip of the servomechanical actuator is in the process of establishing mechanical contact in order to move the fine adjustor flexure. Problems such as parasitic displacement can be exaggerated in this situation until a significant mechanical preload is established by advancing the actuator.

The relative permittivity determined using WLS analysis is 1.011. The difference between this value and the known permittivity of nitrogen gas, 1.001, can be compensated using Figure 4.10 in Section 4.6. This compensation can be simplified as a 1% reduction of the measured value. The validity of this correction is be verified by plotting the relative permittivity from WLS analysis as a function of data range as shown

in Figure 5.4. This graph shows close resemblance to the simulated result in Figure 4.10, confirming the model of the electrode shape error.

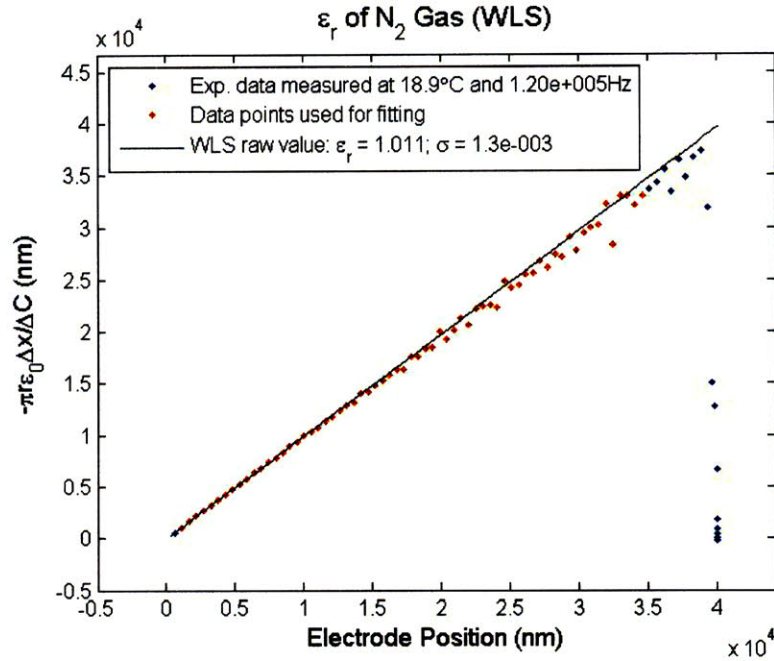


Figure 5.3: Permittivity of nitrogen gas analyzed using WLS analysis.

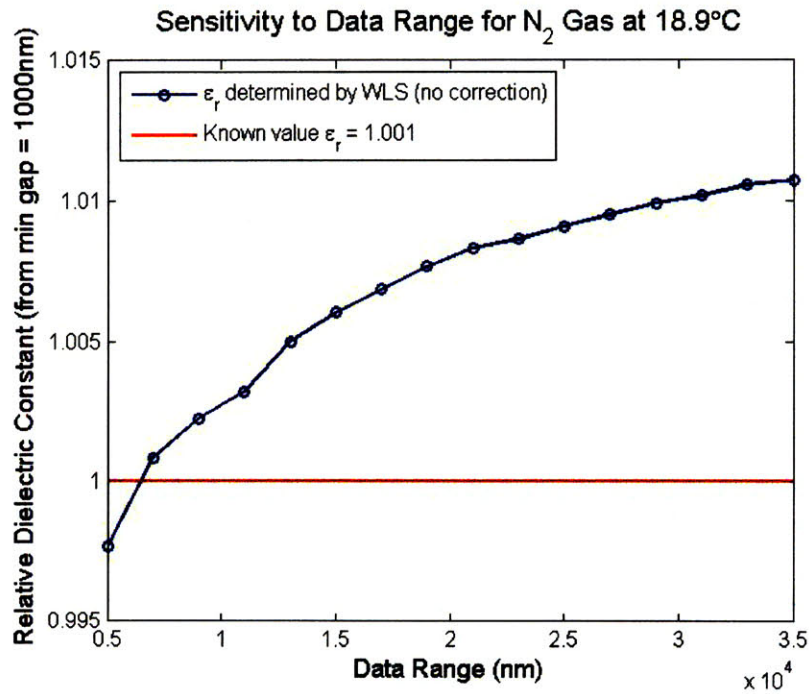


Figure 5.4: Relative permittivity determined by WLS versus data range from measured data for nitrogen gas.

The model used in WLS analysis is further validated by graphing the weighted residue from the WLS fit. The random distribution of data points in Figure 5.5 confirms the validity of the weight function.

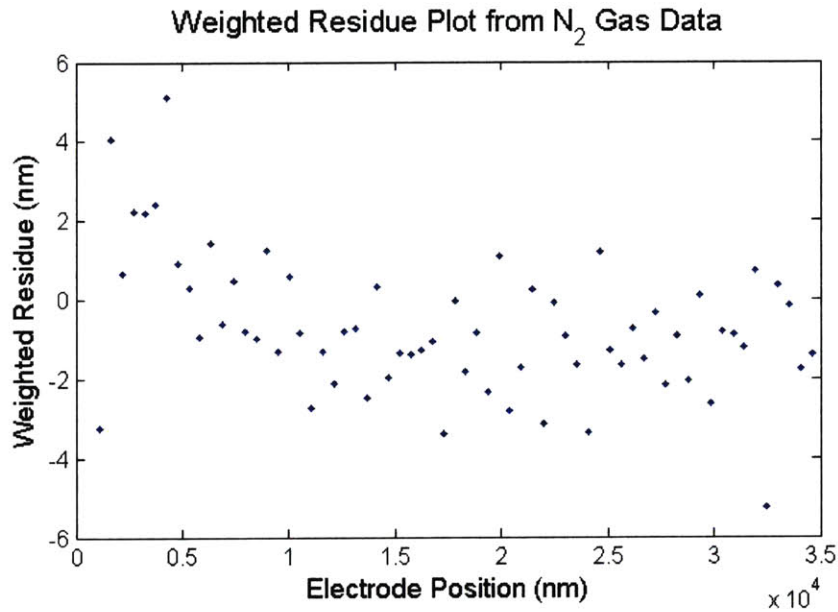


Figure 5.5: Weighted residue from the permittivity of nitrogen gas measurement.

The relative permittivity of nitrogen gas is can also be determined using the NL1 analysis as described in Section 4.3. The transformed data for this analysis is plotted in Figure 5.6, where the horizontal axis plots the capacitance and electrode displacement transformed according to the right hand side of equation (4.43) and the vertical axis plots the differential values of capacitance. The relative permittivity is equal to the slope obtained by simple least squares fitting in the transformed figure. The value of the relative permittivity determined using this technique is 0.997. The optimization for x_0 based on the RMS fitting error is shown in Figure 5.7. The rounded curve around the minimum is an indication the level of uncertainty in the determination of x_0 , which can lead to an inaccurate prediction of the relative permittivity.

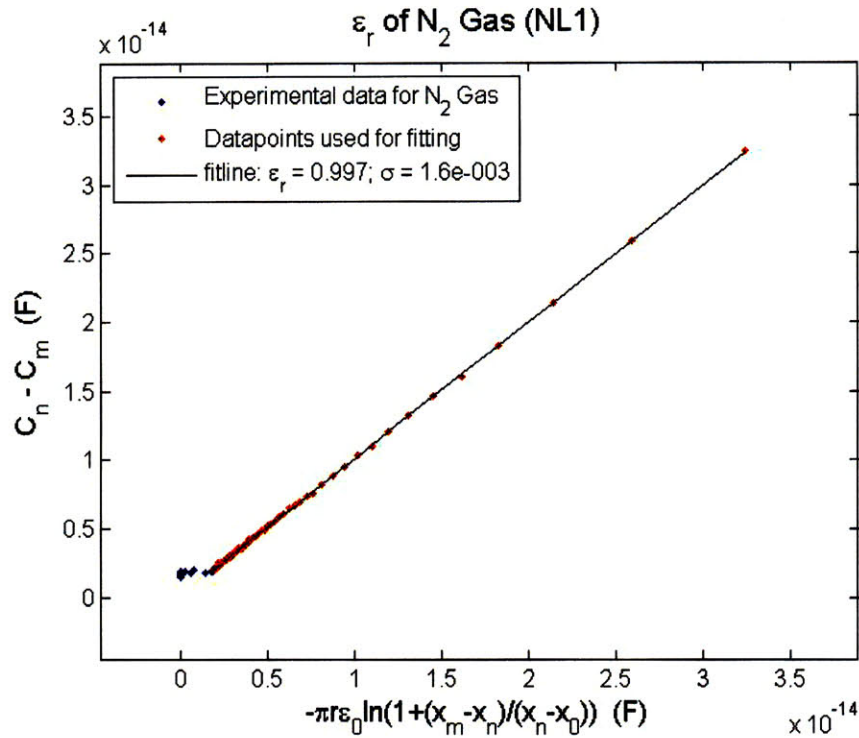


Figure 5.6: Permittivity of nitrogen gas measurement analyzed using NL1. Data points from smaller electrode gaps that are not used for fitting are located beyond the top right boundaries of the graph. These data points have been omitted for clarity.

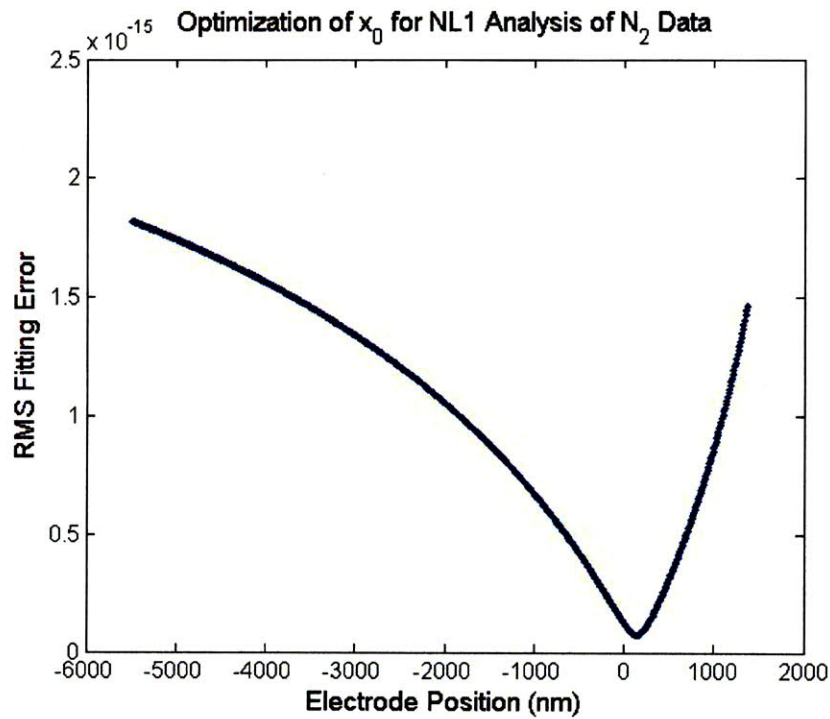


Figure 5.7: Optimization for x_0 using the RMS fitting error for NL1 analysis of nitrogen gas data.

Measurement of the relative permittivity of nitrogen gas as described above are repeated multiple times in order to establish statistical significance of the observations. The values of the relative permittivity analyzed using both WLS and NL1 techniques are shown in Figure 5.8 from 20 datasets. The output from WLS analysis has been corrected by 1% as previously discussed. The mean of these values is 1.002 with a standard deviation of 1.8×10^{-3} . The mean of the output values from NL1 analysis is 1.000 with a standard deviation of 5.5×10^{-3} . Both of these values are well within the 1% target accuracy. The results from NL1 analysis show higher standard deviation than WLS analysis and thus confer the predictions of Section 4.6.

The standard deviations from WLS and NL1 analysis, σ_{WLS} and σ_{NL1} , in Figure 5.8 can also be used to estimate the level of capacitance and position uncertainty modeled in Section 4.5. The noise sensitivity model in Figure 4.15 and Figure 4.16 indicate that the values of σ_{WLS} and σ_{NL1} is equivalent to either a the capacitance uncertainty where $\sigma_C = 2 \times 10^{-16}$ F, or position uncertainty where $\sigma_x = 2$ nm, or some combination of both.

A zoomed version of Figure 5.3 is shown in Figure 5.9 to show the behavior at small electrode gaps. The three data points below 500 nm electrode gap depart noticeably from the straight line. The suspected cause is a thin film of water on the surface of the electrodes. More investigations of measurements across small gaps will be discussed in Section 5.6.

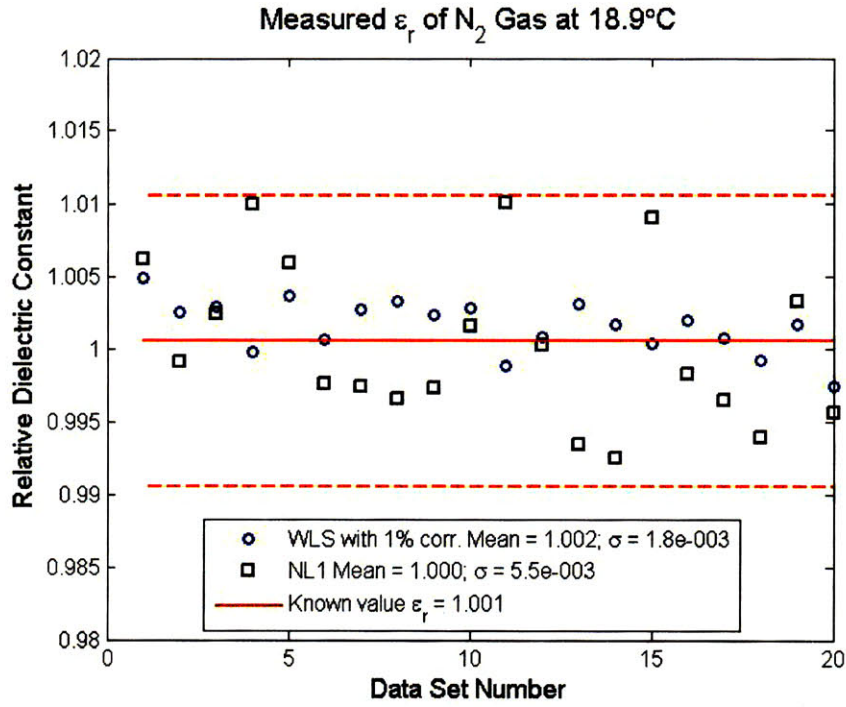


Figure 5.8: Permittivity of nitrogen gas from repeated measurements determined using both WLS and NL1 analysis.

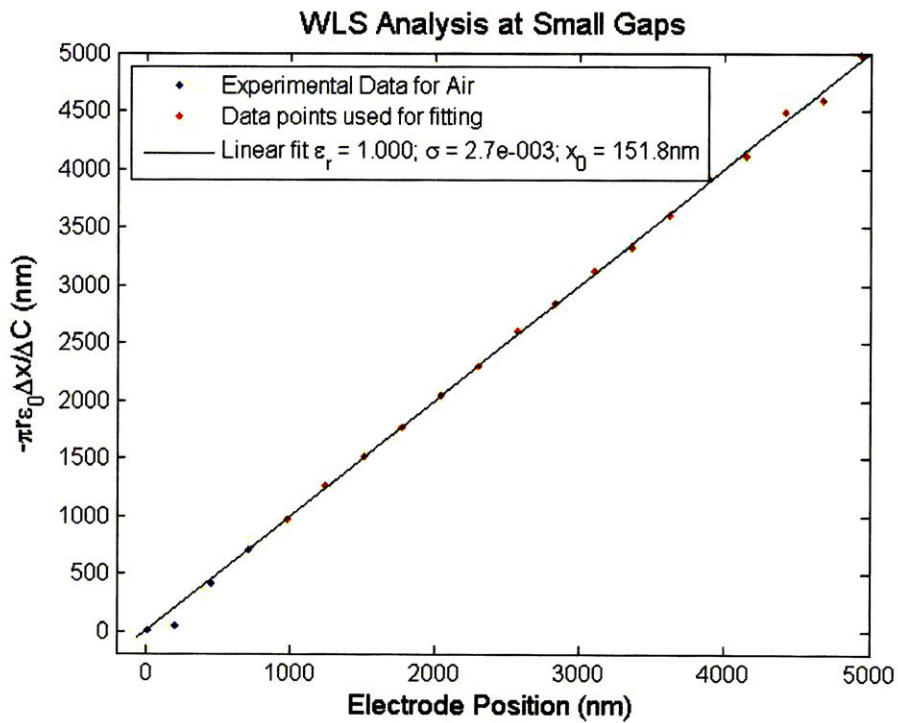


Figure 5.9: Zoomed view of Figure 5.3 show the behavior at small electrode gaps.

5.2 Permittivity of Methanol

The capability of the technique described in this thesis for measuring the permittivity of liquid media has been verified by measurements of methanol. The large permittivity difference between nitrogen gas and methanol demonstrates the capability for accurate measurements without requiring wet calibration across a wide range of permittivity values.

Methanol is a common solvent with well characterized properties. The relative permittivity of methanol is 32.6 at 25°C, and decreasing by approximately 0.5% for every degree increase in temperature. The value of the relative permittivity versus temperature is described by the empirical formula [17]

$$\epsilon_r = \frac{a_0}{T^2} + \frac{a_1}{T} + a_2 + a_3T. \quad (5.1)$$

where the temperature, T , has units of Kelvins and the constants a_0 thru a_4 are shown in Table 5.1. This formula is valid from 220 K to 330 K.

Temp Range (°K)	a_0	a_1	a_2	a_3
220 – 330	-41846.68	18855.60	35.08116	0.01658160

Table 5.1: Constants used in equation (5.1) for predicting the relative permittivity of pure methanol.

One of the difficulties in measuring pure methanol is its hygroscopicity. In atmospheric conditions, methanol absorbs water vapor from the air, altering both its permittivity and conductivity. In order to prevent water contamination, 99.9% pure anhydrous methanol packaged under an Argon environment (Alpha Aesar: 41838) is used. The methanol liquid is shipped in a special bottle capped by a flexible membrane. Liquid is drawn from the bottle into a syringe using a 6-inch long needle pushed through the membrane. The methanol sample was not degassed since degassing and re-exposing

to atmosphere rapidly cools the sample liquid and facilitate condensation of water vapor. The sample liquid in the syringe is injected into the chamber via the microtubes and the fluid ports. The first 10 ml of the sample liquid is flushed through the chamber in order to help remove impurities before beginning permittivity measurements.

As in the measurements for nitrogen gas, the impedance is measured starting at a large electrode separation and gradually decremented until the electrodes come into contact with one another. The electrode separation is decremented in steps of 500 nm from approximately 35 μm until the onset of direct conduction between the electrodes. The impedance is measured after each adjustment, waiting 1 second for the positioning mechanism to settle to its final position. The excitation signal is a sinusoidal source with 10 mV RMS amplitude. The excitation signal used in methanol is much smaller than that of nitrogen gas in order to prevent oxidation of the electrode surface. Low voltage excitations are also made possible because the permittivity of methanol is many times higher than nitrogen, which significantly improves the signal-to-noise ratio. The excitation frequency is 120 kHz.

The sample temperature is controlled using the thermal control system described in Section 2.3.2. Since only open-loop control has been implemented, temperature changes requires approximately six hours before reaching its final value. Thus, only a limited number of data points have been collected for temperature varying experiments.

The resistance versus electrode displacement plot is shown in Figure 5.10. Unlike the nitrogen gas measurements, the resistance of methanol is not dominated by leakage currents and it is a readily measurable value. The resistance of methanol, however, is

highly dependent on the concentration of impurities and is not a well-controlled parameter.

The capacitance versus displacement data is shown in Figure 5.11. Similar to the nitrogen gas measurements, the capacitance increases with decreasing electrode separation until the electrodes begin to conduct. At which point, the capacitance increases sharply before dropping to a negative value.

The permittivity is determined from the capacitance versus displacement data using the procedure described in Section 4.2. The transformed data is shown in Figure 5.12 where the electrode displacement is plotted along the horizontal axis and the quantity y , defined in equation (4.7), is plotted along the vertical axis. The data fall along a straight line as predicted and the relative permittivity is determined by WLS fitting as described in Section 4.2. As in the case for nitrogen, some of the data points around the minimum and maximum electrode gaps are excluded from the fitting: Data points from below 1 μm are not used in order to avoid surface effects at the electrode-electrolyte interface. Data points from beyond 35 μm are not used in order to control the total range of data and avoid potential errors from the actuator at the end of its travel.

As a result of its higher permittivity, data from methanol in Figure 5.12 show considerably less noise than results from nitrogen in the corresponding Figure 5.3. The data clearly shows a droop at larger electrode separation that is caused by the geometry of the electrode mounting shaft.

The relative permittivity of methanol, at 18.0°C, determined using WLS analysis is 34.4, while the established value is 34.0 [17]. A permittivity value within 1% of the established value can be obtained by applying a -1% correction as discussed earlier. As in

the nitrogen case, the validity of the -1% correction is confirmed by plotting the relative permittivity as a function of data range in Figure 5.13. This graph shows close resemblance with the modeled result from Figure 4.10 and the nitrogen gas result in Figure 5.4.

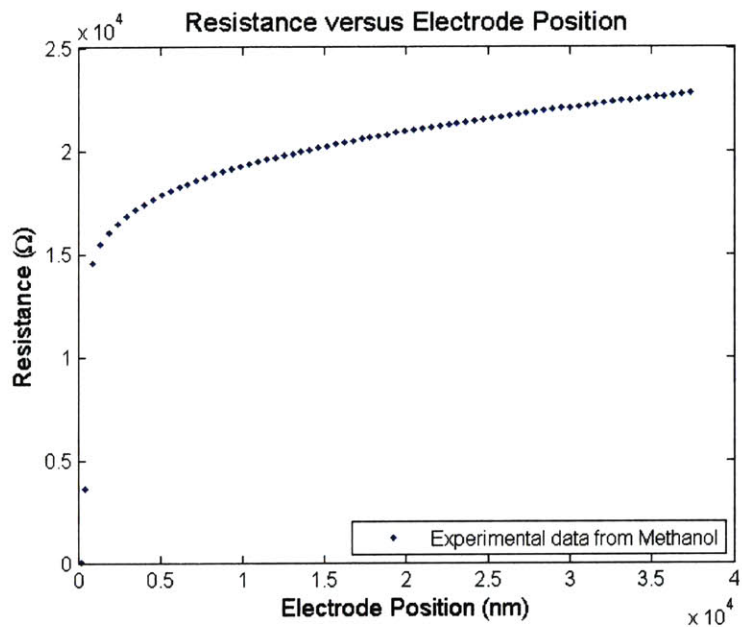


Figure 5.10: Example resistance versus electrode position plot for methanol.

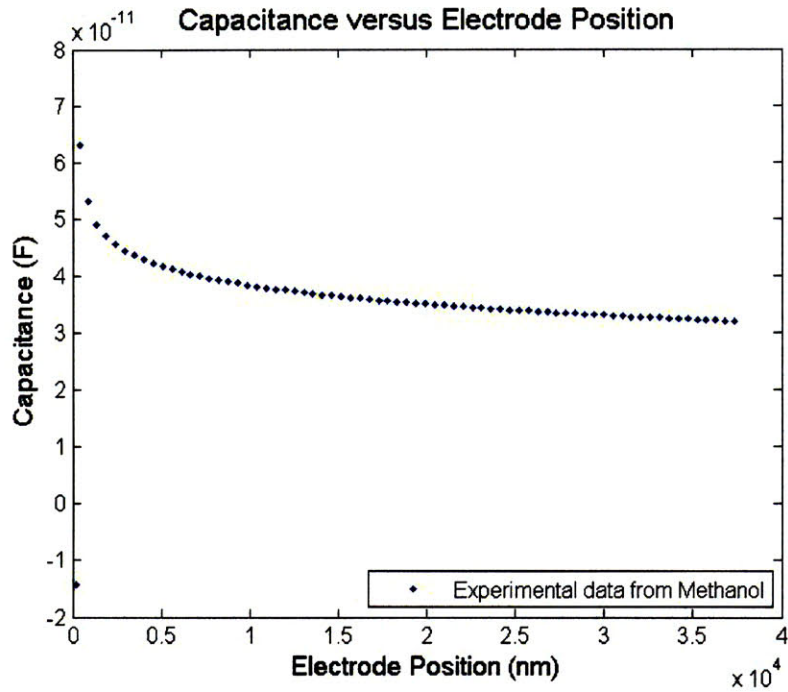


Figure 5.11: Example capacitance versus electrode position plot for methanol.

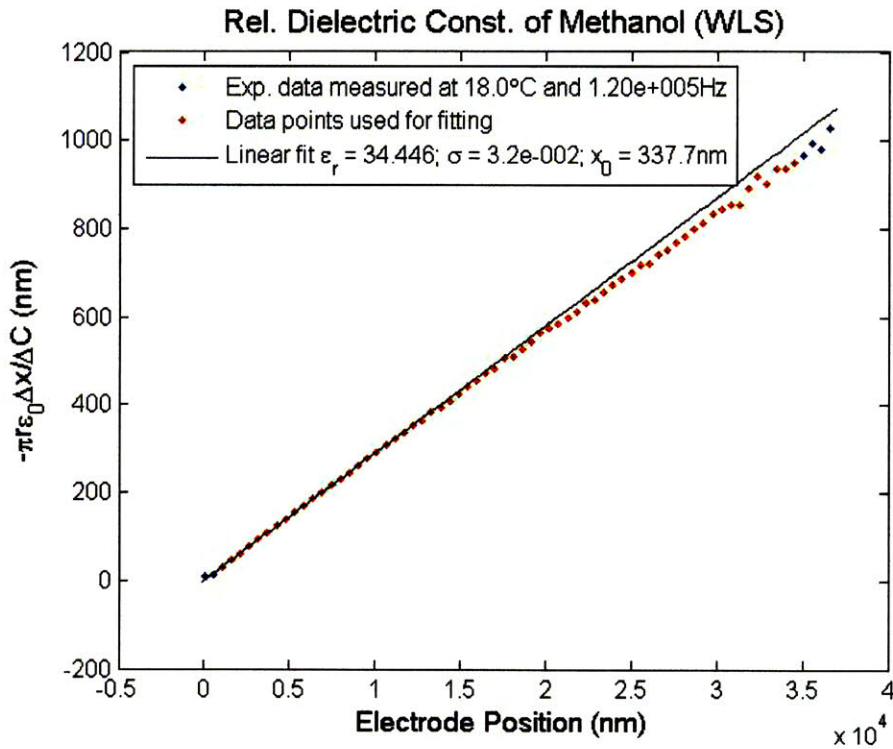


Figure 5.12: The relative permittivity of 99.9% pure methanol measured at 15.4°C and 120 kHz. The relative permittivity has been determined using WLS analysis.

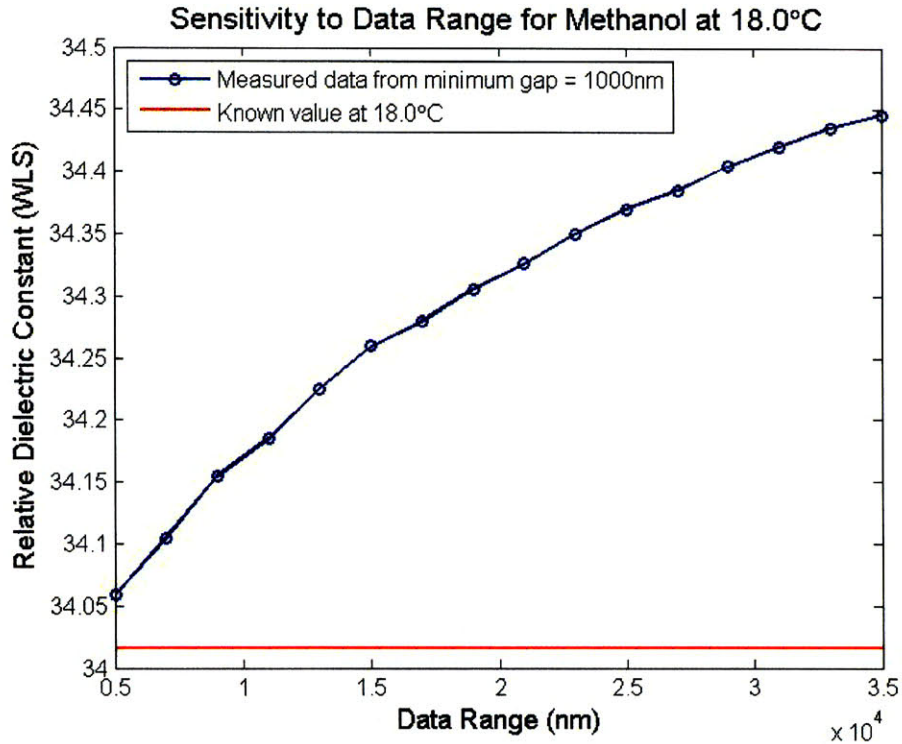


Figure 5.13: Relative permittivity determined by WLS versus data range from measured data for methanol.

Measurements of the permittivity of methanol are repeated multiple times in order to establish statistical significance of the observations. The measurement results from 30 datasets are analyzed using WLS analysis with the -1% correction and NL1 analysis and are shown in Figure 5.14. The mean of the corrected WLS values is 34.13 and the standard deviation is 0.06. These results are well within the $\pm 1\%$ target range. In fact, the standard deviation is only 0.18% of the mean. The relative permittivity values analyzed using NL1 has a mean of 34.00 and a standard deviation of 0.09. Once again, it has been shown that the result of the NL1 analysis is correct without modification, but the standard deviation, at 0.28% of the mean, is high than that of WLS analysis.

The relative permittivity values of methanol measured at three different temperatures are shown in Figure 5.15. The results are analyzed using WLS and then

corrected by 1%. The results are well within the established values of methanol predicted by equation (5.1). The same dataset is also analyzed using NL1 and shown in Figure 5.16. In this dataset, the results around 18°C and 22°C are within 1% of the established value. The results from 26°C deviated slightly below the 1% limit. This deviation is likely a result of inaccurate temperature control as the temperature is raised from below room temperature to above room temperature.

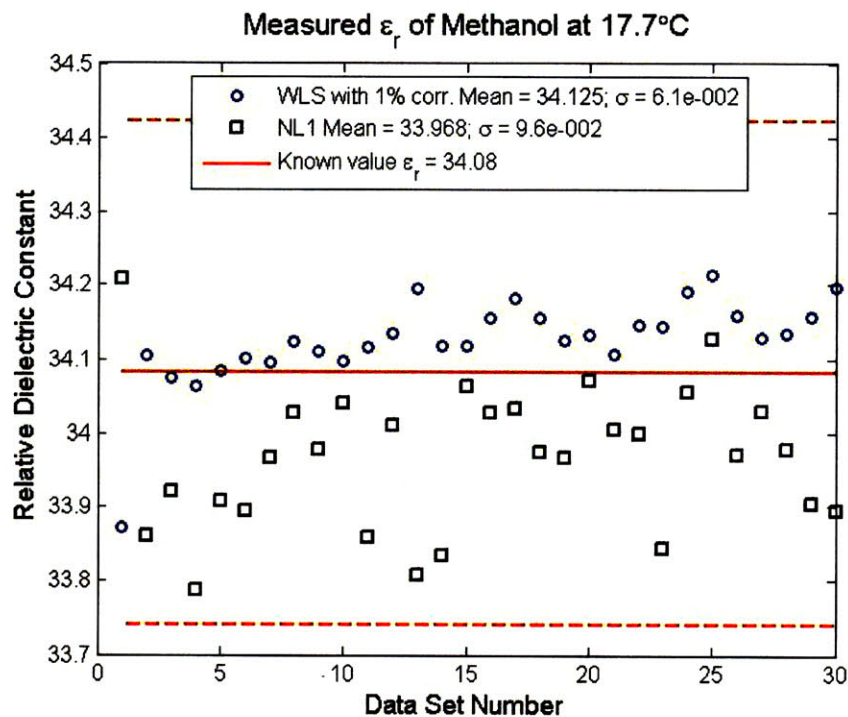


Figure 5.14: Relative permittivity of 99.9% pure methanol at 15.4°C and 120 kHz from repeated measurements determined using WLS analysis.

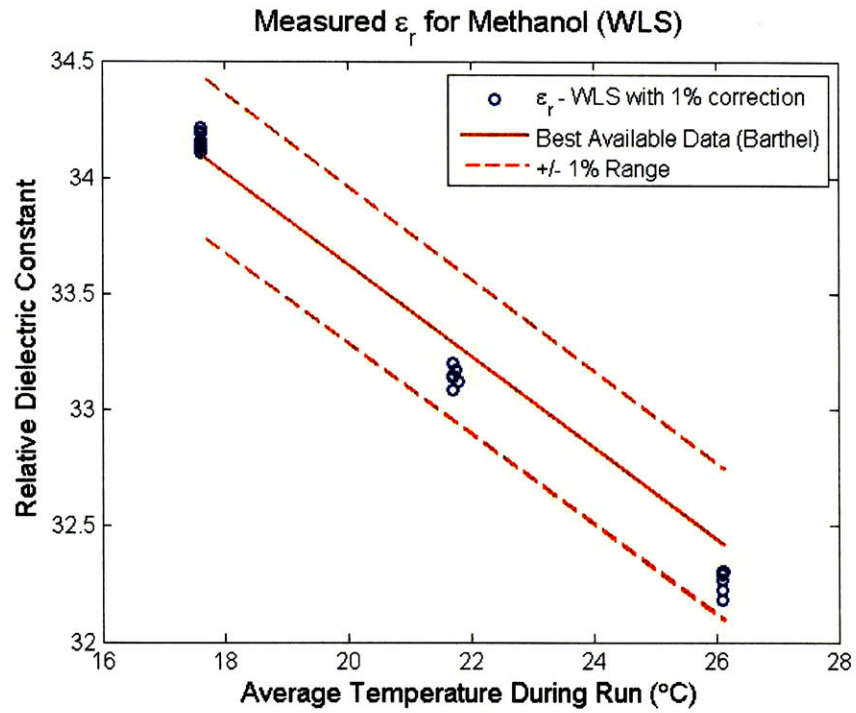


Figure 5.15: Measured relative permittivity from repeated experiments analyzed using WLS with -1% correction.

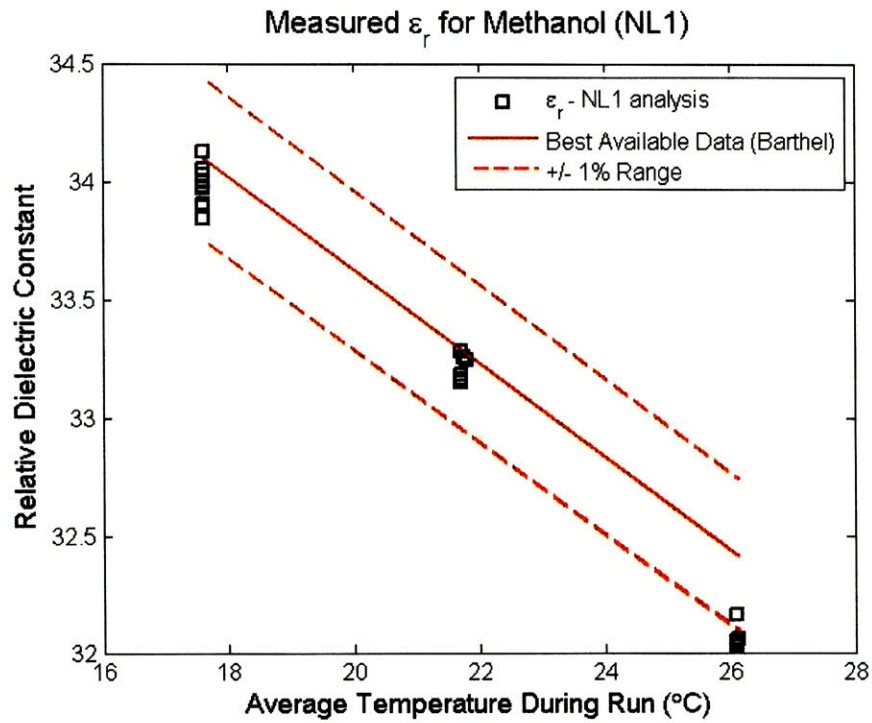


Figure 5.16: Measured relative permittivity from repeated experiments analyzed using NL1.

5.3 Additional Permittivity Measurements

The capability for accurately measuring permittivity without wet calibration is further validated by measurements of 2-propanol (also known as isopropanol) and water. In order to control the impurities in water, a 0.1 mM KCl solution in water has been used instead. The experiments have been performed in the same manner as before. The results have been analyzed using WLS fitting with the -1% compensation to account for the shape of the electrode mount as described previously. Results from repeated relative permittivity measurements of 2-propanol at 17.6°C are shown in Figure 5.17. Results from relative permittivity versus temperature measurements of 2-propanol are shown in Figure 5.18. Results from repeated relative permittivity measurements of 0.1 mM KCl solution at 18°C are shown in Figure 5.19. Results from relative permittivity versus temperature measurements of 0.1 mM KCl solution are shown in Figure 5.20.

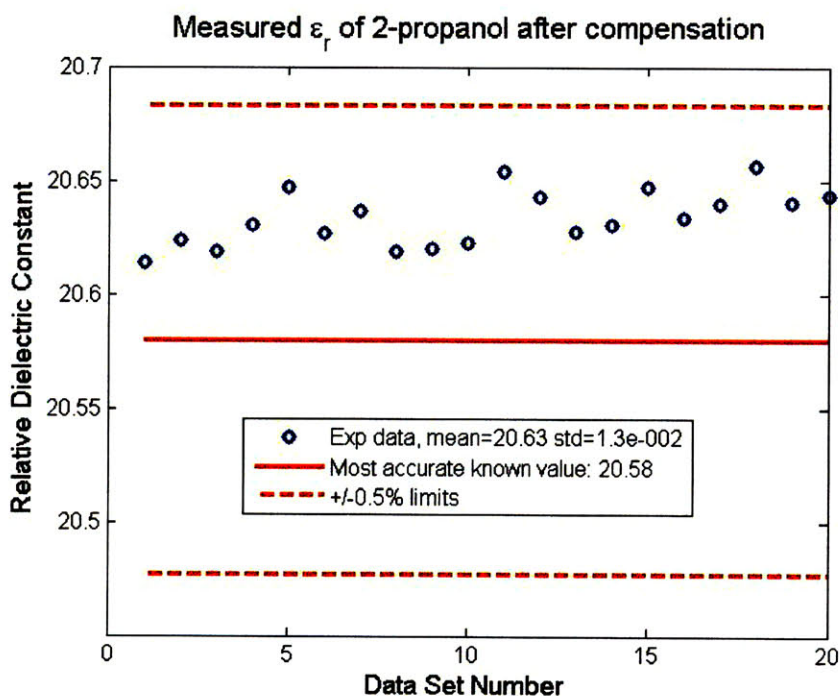


Figure 5.17: Repeated measurements of the relative permittivity of 2-propanol at 17.6°C.

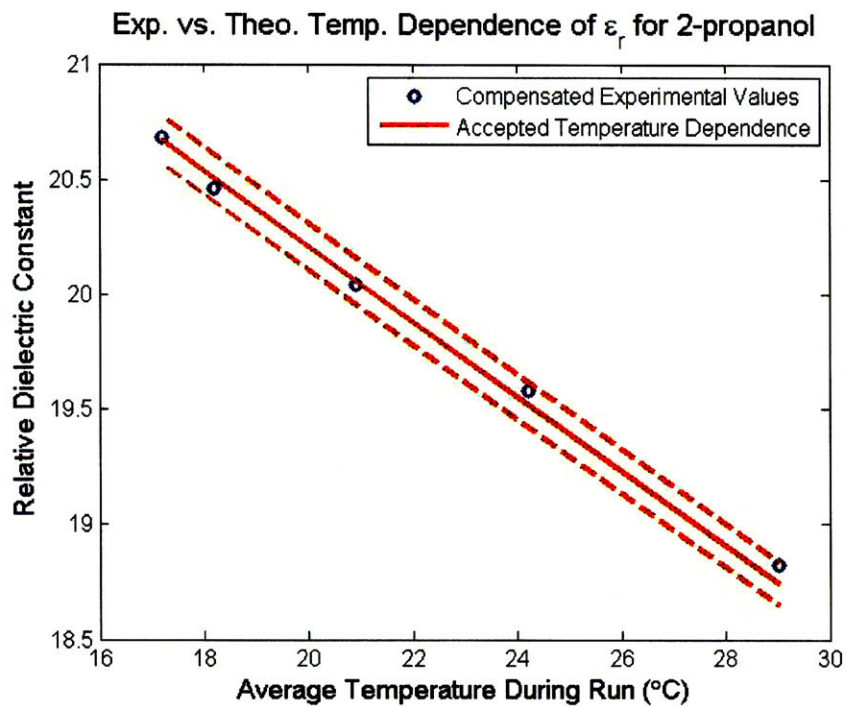


Figure 5.18: The permittivity of 2-propanol as a function of temperature after compensation.

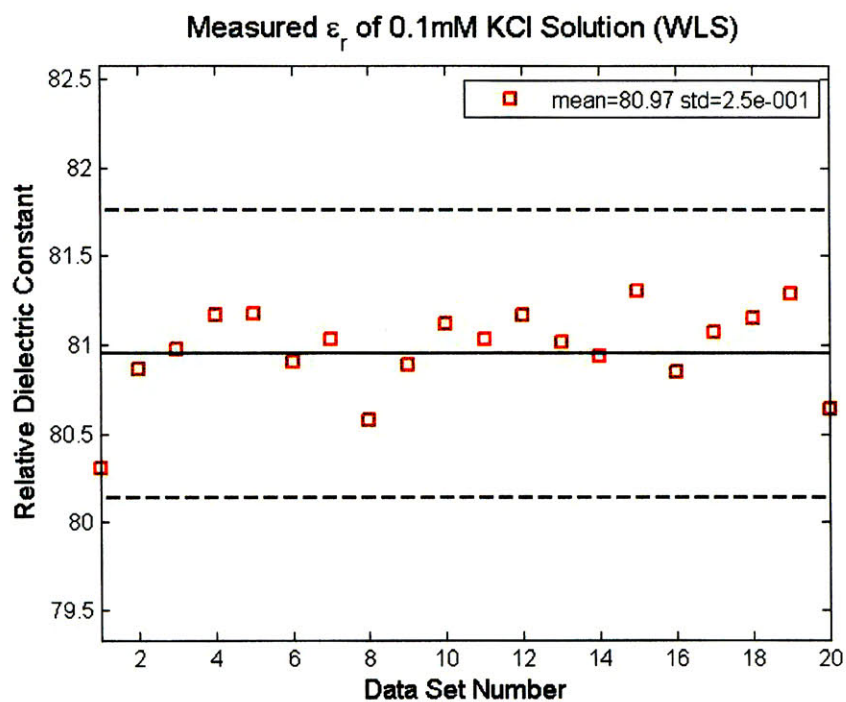


Figure 5.19: Repeated measurements of the permittivity of 0.1 mM KCl solution at 18.0°C.

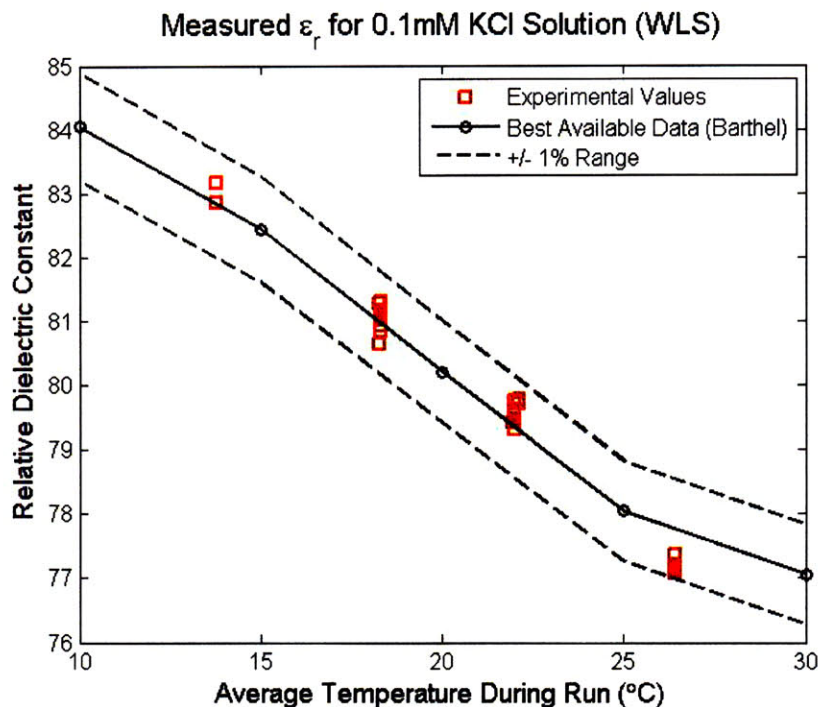


Figure 5.20: Temperature dependence of the permittivity of 0.1 mM KCl solution after compensation.

5.4 Conductivity of Potassium Chloride Solutions

The capability of the technique described in this thesis for measuring the conductivity of liquid media is verified by measurements of potassium chloride (KCl) solutions in water. KCl solutions have long been used as a standard liquid for calibrating the cell constant of standard conductivity meters, and as a result, accurate, premixed bottles of KCl solutions are available commercially.

In physical chemistry literature, electrical conductivity, κ , is typically specified as molar conductivity, Λ , which is defined as the electrical conductivity normalized over concentration as

$$\Lambda = \kappa / c . \quad (5.2)$$

The molar conductivities of KCl solutions are predicted from Fuoss-Onsager theory [14] using the equation

$$\Lambda = \Lambda_0 - Sc^{1/2} + Ec \log c + J_1c - J_2c^{3/2}. \quad (5.3)$$

The values of the constants at 10, 18, and 25°C were measured by Barthel [14] and shown in Table 5.2 for c in units of $mol \cdot l^{-1}$. Using these values, the molar conductivity is calculated at several concentrations and shown in Table 5.3.

Constants for Calculating Molar Conductivity					
Temp (°C)	Λ_0	S	E	J_1	J_2
25	149.873	95.01	38.48	183.1	176.4
18	129.497	80.38	32.87	154.3	143.0
10	107.359	64.98	27.07	125.4	110.3

Table 5.2: Constants used in equation (5.3) for predicting the conductivity of KCl solutions.

The units of molar conductivity in literature can be quite confusing because of the use of centimeters and liters, which are non-standard SI units. In physical chemistry reference books [17, 18] and papers [14] the value of Λ is typically specified in units of $10^{-4} m^2 \cdot S \cdot mol^{-1}$. With the concentration, c specified in $mol \cdot l^{-1}$, the conductivity determine from equation (5.2) has units of $10^{-1} S \cdot m^{-1}$.

Molar Conductivity $\Lambda \cdot 10^{-4} m^2 S mol^{-1}$					
Temp (°C)	$10^{-2} M$	$5 \times 10^{-3} M$	$1 \times 10^{-3} M$	$5 \times 10^{-4} M$	$1 \times 10^{-4} M$
25	140.25	142.99	146.78	147.69	149.57
18	121.35	123.66	126.88	127.65	129.24
10	100.76	102.64	105.24	105.86	107.15

Table 5.3: Conductivities for various concentrations of KCl calculated using equation (5.3).

The sample liquid used in these measurements is 10 mM KCl solution from VWR (VW3349-1). The expected conductivity at 25°C can be determined from the molar conductivity in Table 5.3, multiplying by the concentration, and adjusting for the appropriate units, the expected conductivity is 0.1403 S/m.

The temperature dependence of conduction through electrolytes can be described by the Arrhenius equation

$$\kappa = \kappa_0 \exp(-qE_a / k_B T). \quad (5.4)$$

where q is the elementary charge, k_B is the Boltzmann factor, and T is the absolute temperature. The factor E_a is defined as the activation energy for conduction, while κ_0 is the reference conductivity, which is determined by the charge carrier concentration and mobility. From the KCl conductivity values measured by Barthel [14], the activation energy for conduction is 0.161 eV.

The experimental procedure for measuring conductivity is identical to the procedure for measuring the permittivity of methanol. The impedance is measured from a starting electrode gap of approximately 35-40 μm and gradually decreasing until the onset of direct conduction across the electrode. The electrode separation is decremented in steps of 500 nm. The impedance is measured after each adjustment, waiting approximately 1 second for the positioning mechanism to settle to its final position. The amplitude of the excitation signal is 10 mV RMS. The lower excitation amplitude is used to minimize oxidation of the electrode and mounting apparatus. As in the case for methanol, an excitation frequency of 120 kHz is used. The resistance versus electrode displacement plot is shown in Figure 5.21. The range of resistances is quite small from 80 down to 50 Ω before dropping to the electrode contact resistance which ranges between 10 and 15 Ω . The corresponding capacitance versus electrode displacement plot is shown in Figure 5.22. The measured capacitance is dominated by the interfacial capacitance, and is therefore, quite high. When the electrodes come into contact, the capacitance drops to a negative value as previous cases for nitrogen gas and methanol. The frequency spectrum of KCl solutions will be discussed in the following section.

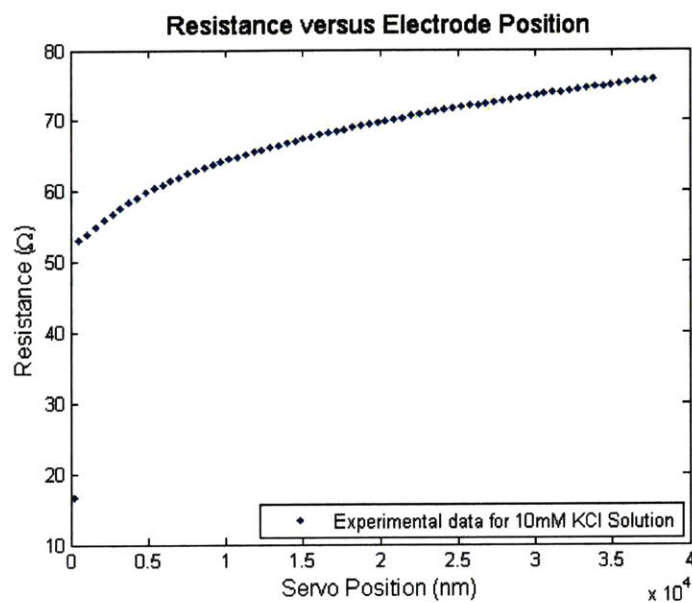


Figure 5.21: An example resistance versus electrode position plot from 10 mM KCl solutions.

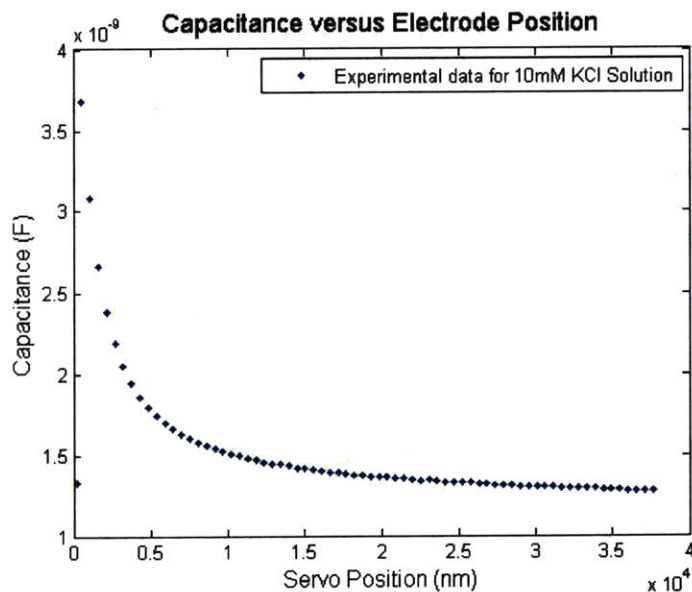


Figure 5.22: An example capacitance versus electrode position plot from 10mM KCl solutions.

The conductivity is determined from the conductance versus displacement dataset, using the procedure and transformation described in Section 4.1. The transformed data is

shown in Figure 5.23, where the electrode displacement is plotted along the horizontal axis. The quantity y , defined in this case as

$$y = -\frac{\pi r \Delta x}{\Delta G}, \quad (5.5)$$

is plotted along the vertical axis.

The transformed data fall along a straight line as predicted by theory and the conductivity is determined by WLS fitting described in Section 4.2. It is interesting to note that the droop due to electrode geometry is not as apparent in conductivity measurements as it is in permittivity measurements. Similar to permittivity measurements, some of the data points around the minimum and maximum electrode gaps are excluded from fitting. Data points below 2 μm are not used in order to avoid interfacial effects at the electrode-electrolyte interface. Data points from beyond 35 μm are also not used to avoid errors caused by the backlash of the actuator. The conductivity of the data shown in Figure 5.23 is 0.126 S/m with a standard deviation of 9.8×10^{-4} S/m.

Data from repeated conductivity measurements at 21.9°C are shown in Figure 5.24. The mean value of κ from these measurements is 0.1247 S/m with a standard deviation of 3.2×10^{-4} S/m. The mean of the measured value is lower than the established value of 0.1319 S/m by approximately 5%. The standard deviation of the measurements, however, is only 0.26% of the mean. Since permittivity measurements yielded results within 1% of the established value, and the equations that relate capacitance with permittivity is exactly parallel with the equations that relate conductance and conductivity, this deviation is likely a result of the variation in the composition of the

sample liquid. Measurements of liquid conductivity as a function of temperature yield additional confirmations of this hypothesis.

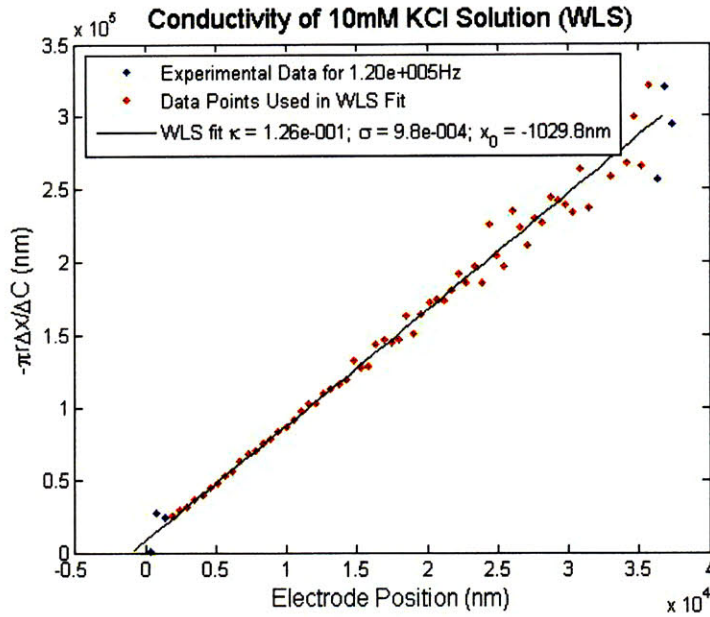


Figure 5.23: An example dataset from conductivity measurements using WLS analysis.

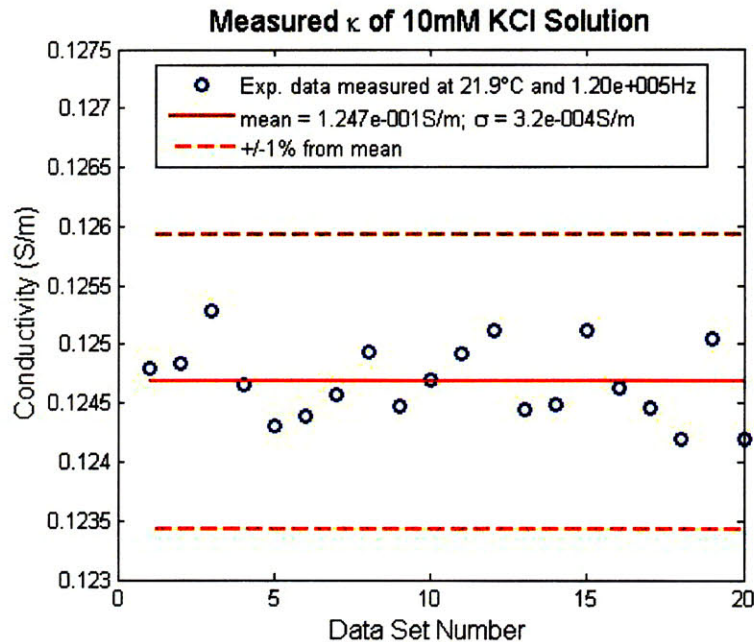


Figure 5.24: Results from conductivity of 10mM KCl solutions at 11.4 °C from repeated 20 times; κ determined using WLS analysis.

The temperature dependence of the conductivity of 10 mM KCl solutions is shown in Figure 5.25. The data sets have been gathered under two different circumstances. The first data set, indicated using square markers, is collected after the impedance test cell has been previously used to measure lower molarity KCl solutions. Although the impedance test cell was flushed with 10 ml of 10 mM KCl solutions before measurement, the measured conductivity values were still lower than the established value by approximately 10%. The second data set, indicated using diamond markers, is collected after 10 mM KCl solution has been introduced into a new impedance test cell. The result is still lower than the established value by approximately 5%.

The deviation of the results in the first set of experiment could reasonably be explained by dilution of the sample liquid by residual liquid. Even though the sample chamber has been flushed, there are pockets of dead volume such as the region inside the mounting shaft behind the electrode where liquid may not circulate well with liquid from the main part of the chamber. The results from the second set of experiments could not have been diluted by liquid left within the impedance test cell. However, since the surface area to volume ratio of the impedance is quite large, it is possible that water condensed on the surface of the impedance test cell could have diluted the sample liquid. Another culprit may be the absorption of the solute by the O-ring seals or the adsorption of solute because of corrosion of the electrode, which would reduce the concentration of the solute. A third possibility may be the presence of microbubbles in the sample liquid, which may have resulted in decreased conductivity. The sample liquid was not degassed in order to avoid solvent loss due to evaporation.

The activation energy for conduction, the parameter defined in the Arrhenius equation in (5.4), can be determined by plotting the log of conductivity versus the inverse absolute temperature (with appropriate constant factors), as shown in Figure 5.26. Therefore, the activation energy is the gradient of the fit lines, which for the first data set is 0.159 eV with $\sigma = 0.001$ eV. For the second data set, the activation energy is also 0.159 eV with $\sigma = 0.0007$ eV. These values are in relatively good agreement with the established value of 0.161 eV, which reflects the fact that the mechanism for conduction is consistent with potassium ions and chlorine ions in water. The small amount of deviation in this case may also have come from the presence of microbubbles.

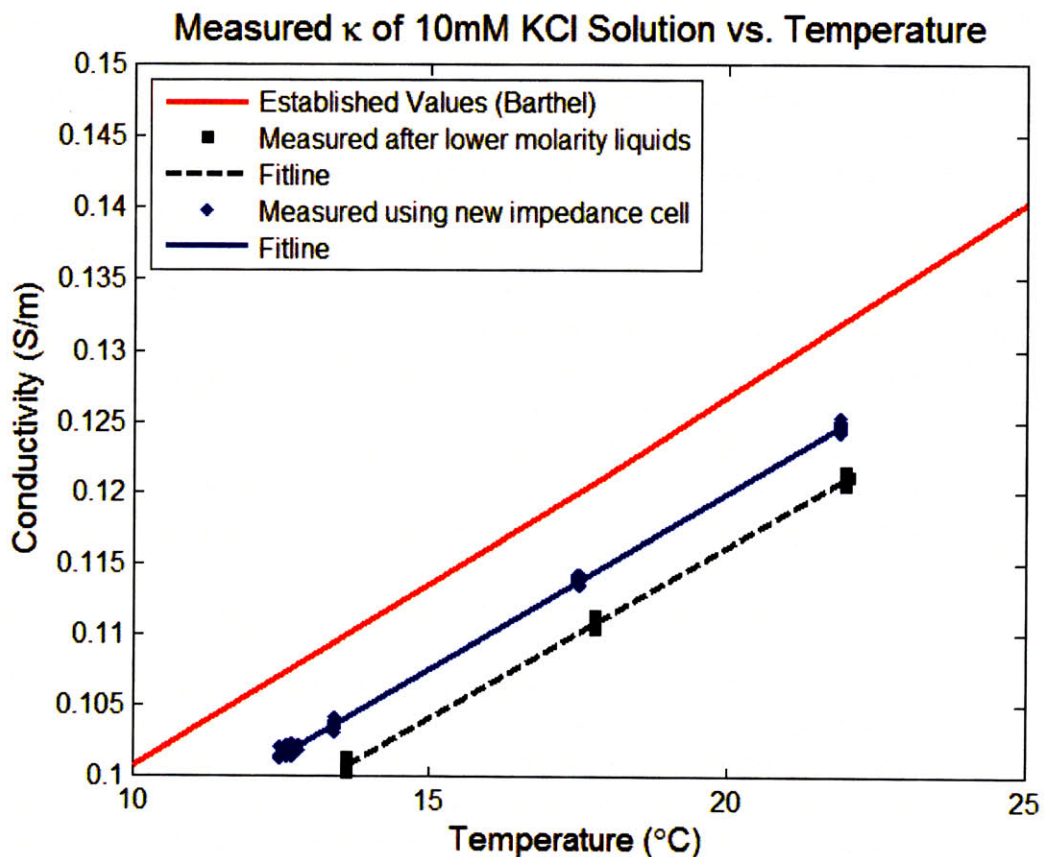


Figure 5.25: Conductivity versus temperature for 10 mM KCl solutions. The data points indicated by squares is measured after the chamber had previous been used to measure lower molarity solutions. The data points indicated by diamonds is measured on a newly assembled impedance test cell.

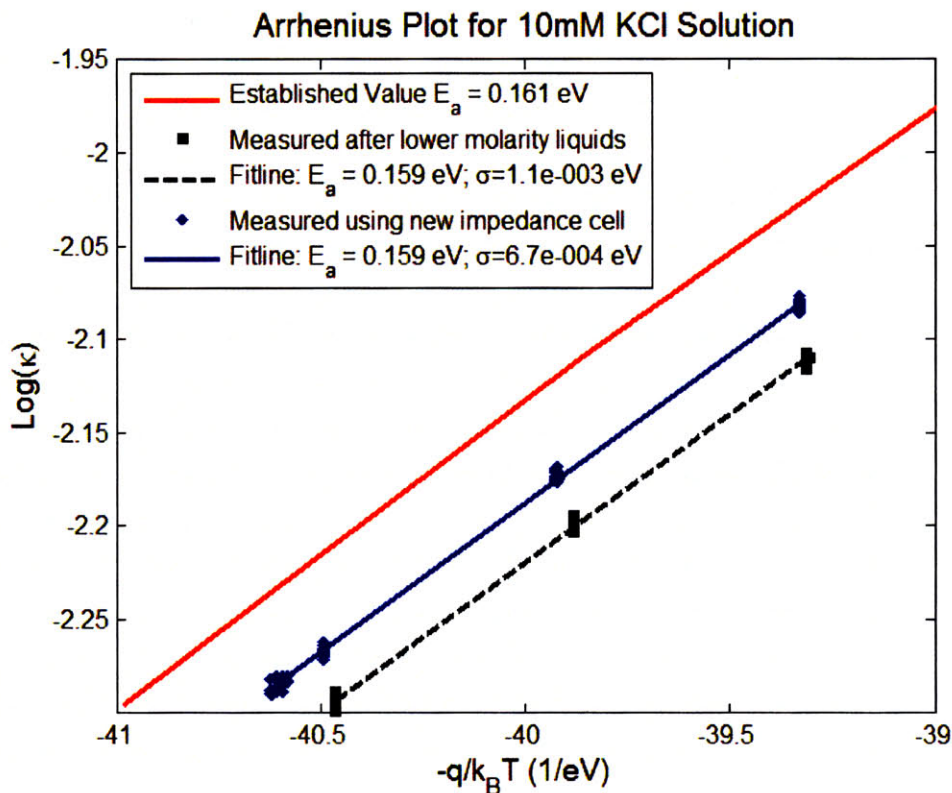


Figure 5.26: Arrhenius plot for 10 mM KCl solutions.

5.5 Frequency Dependence Measurements

Measurements up to this point have exclusively been performed at 120 kHz in order to avoid frequency dependent effects described in Section 3.2.2. This section describes measurements over a wide range of frequencies in an attempt to verify the equivalent circuit of the GCS model described in Section 3.2.2.

Recall from Section 3.2.3, the equivalent circuit of the GCS model, shown in Figure 3.7, is equivalent to the bulk capacitance and resistance between the zeros at ω_1 and ω_2 . As the frequency lowers, however, the measured impedance begins to be affected by the interfacial capacitance. When the impedance in this frequency region is interpreted as a simple parallel capacitance and resistance, the measured capacitance and resistance has the expressions:

$$C = C_s \left(1 + \frac{1}{\omega^2 R_s^2 C_s C_p} \right) \left(\frac{R_s}{R} \right)^2. \quad (5.6)$$

$$R = R_s \left(1 - \frac{C_s}{C_p} \right) \frac{(1 + (\omega RC)^2)}{(1 + (\omega R_s C_s)^2)}. \quad (5.7)$$

Clearly, the measured capacitance increases dramatically as the frequency is lowered, or when the bulk capacitance, R_s , is lowered. The latter is equivalent to reducing the electrode gap, which lowers R_s . The measured resistance is not affected by the decrease in frequencies. It is, however, affected by the ratio of the bulk capacitance, C_s , and the interfacial capacitance C_p . At smaller electrode gaps, the value of C_s is greatly enlarged. As a result, the measured resistance decreases; or equivalently, the measured conductance increases.

The measured capacitance data from three frequencies: 240, 24, and 7 kHz, transformed as described in Section 4.2 for WLS analysis, are shown in Figure 5.27. At smaller electrode separations, the measured signal begins to depart noticeably from the straight line. This affect is more pronounced at 7 and 24 kHz and is not noticeable at 240 kHz.

The measured conductance data from three frequencies: 240, 7, and 1.5 kHz, are shown in Figure 5.28. Here, the data also show a flattening at smaller gaps, which is more pronounced at lower frequencies. In the capacitance case, this flattening seems to approach a y value of zero, whereas in the conductance case, the flattening curve plateaus to a constant y value before claspng to zero at the onset of direct conduction between the electrodes. The plateau of the y value is dependent on the excitation frequency and indicate a constant derivative, dG/dx . The vertical offset of the lower frequency curves

suggest that the flattening of the curve is caused by a physical layer on the order of the electrode separation where the flattening begins to occur.

The spectrum of the measured relative permittivity for a 0.1mM KCl solution is shown in Figure 5.29. The measured permittivity increases sharply at lower frequencies since the measured impedance becomes dominated by the interfacial capacitance. The spectrum of the measured conductance is shown in Figure 5.30. The value of the measured conductance remains relatively constant over the measured spectrum. The conductance increases by approximately 5% beyond 500 kHz. This effect is likely due to high frequency terms in expression (5.7). There is also a slow increase of the measured conductivity at lower frequencies. This is likely a result of low frequency artifacts relating to C_s and C_p .

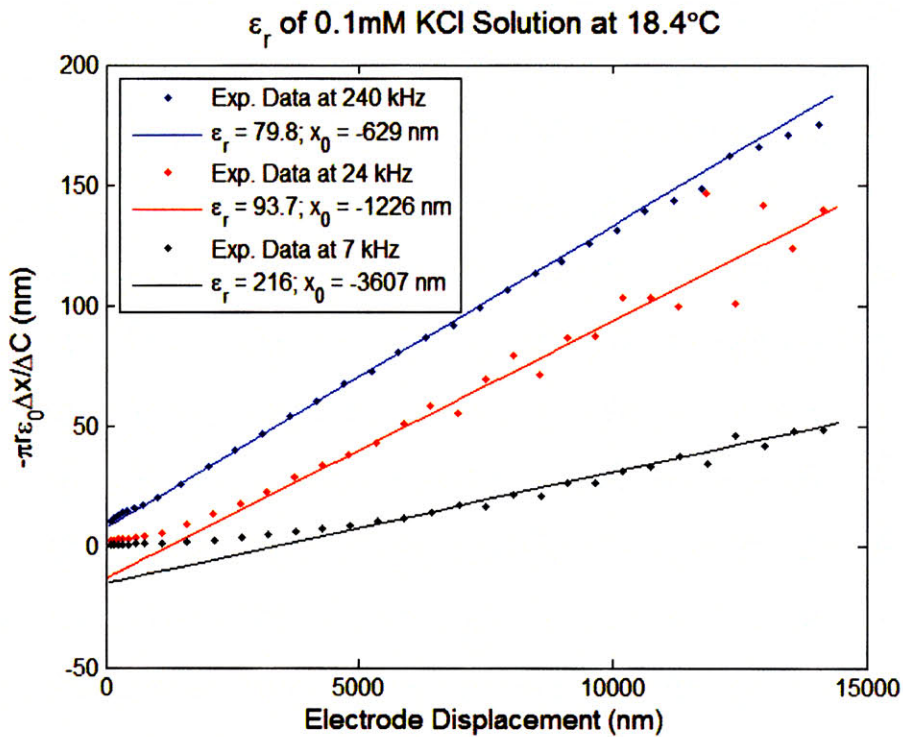


Figure 5.27: Relative permittivity measurements of 0.1 mM KCl solution at 240, 24, and 7 kHz.

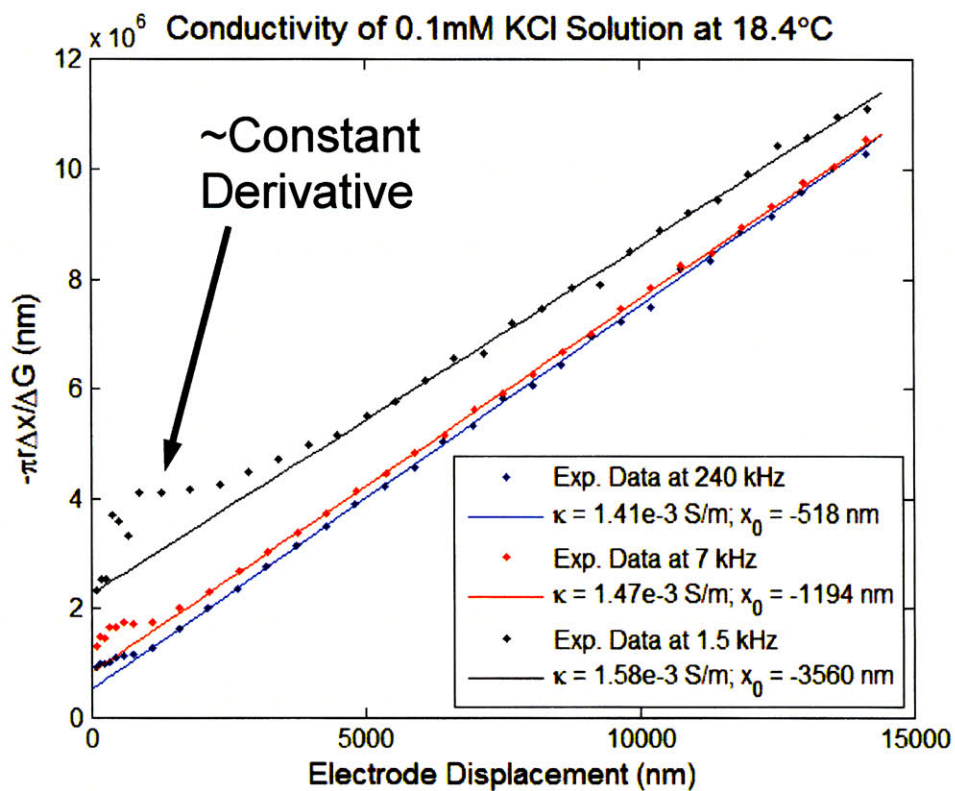


Figure 5.28: Conductivity measurements of 0.1 mM KCl solution at 240, 7, and 1.5 kHz.

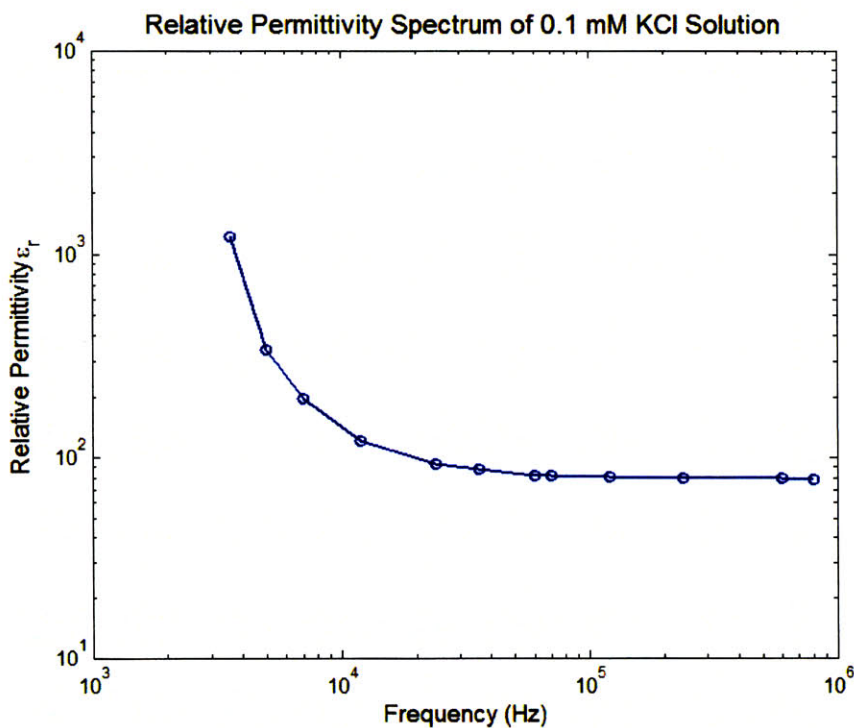


Figure 5.29: Relative permittivity spectra of 0.1 mM KCl solution.

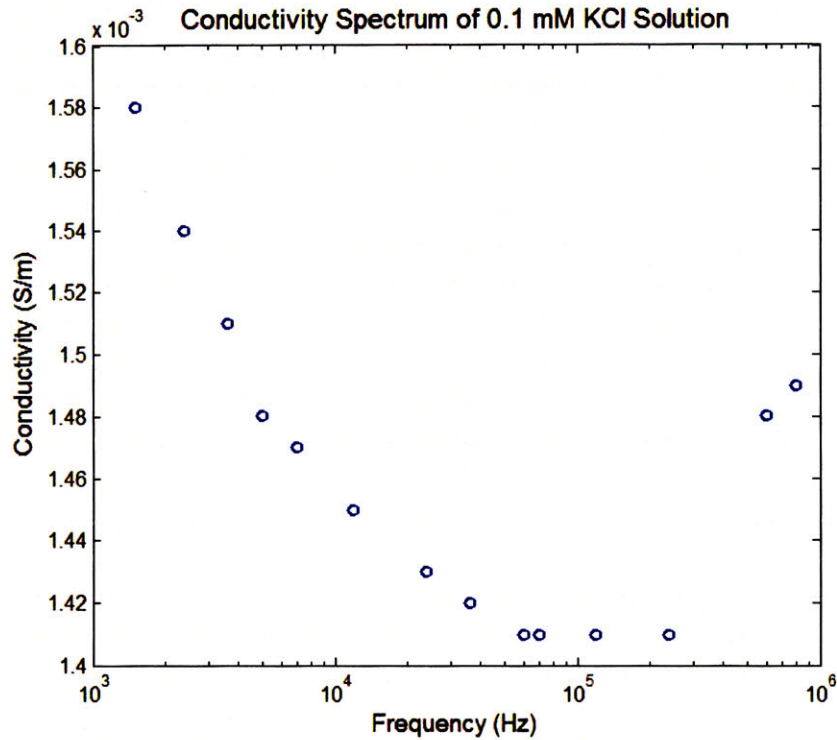


Figure 5.30: Conductivity spectra of 0.1 mM KCl solution.

A common method to plot the frequency spectrum of EIS data is to use a Nyquist diagram, which plots the imaginary part of the impedance versus the real part. The convention in electrochemical literature is to plot the negative of the negative of the imaginary axis, which allows the data points to be shown in the first quadrant. The theoretical Nyquist diagram of the equivalent circuit in Figure 3.7 is shown in Figure 5.31. The frequency range covered by impedance analyzer enables only a small region in the bottom right corner of the Nyquist plot to be measured. Measurement at different electrode gaps enables a family of Nyquist plots to be generated for a series of electrode separations. The Nyquist diagrams for 1 mM KCl and 0.1 mM KCl are shown in Figure 5.32 and Figure 5.33. The measured data follows the circular branch of the data until the minimum point is reached. As the frequency is lowered beyond this point, the measured Nyquist plots do not depart upward as predicted by theory. Rather, the real part of the

measured impedance begins to increase. This departure from theory indicates that the interfacial impedance follows a different model as the equivalent circuit for GCS theory. Thus, more sophisticated models of the interfacial impedance need to be developed.

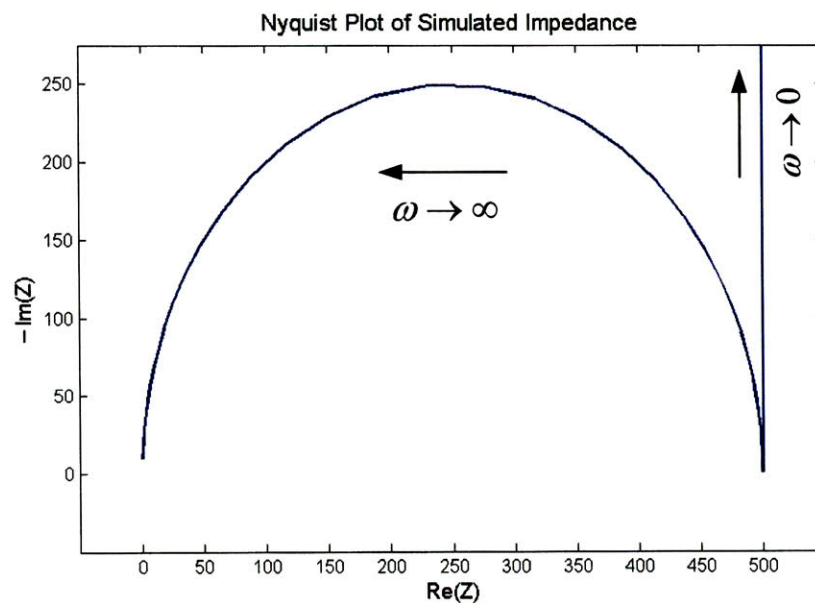


Figure 5.31: Theoretical Nyquist diagram of the equivalent circuit in Figure 3.7.

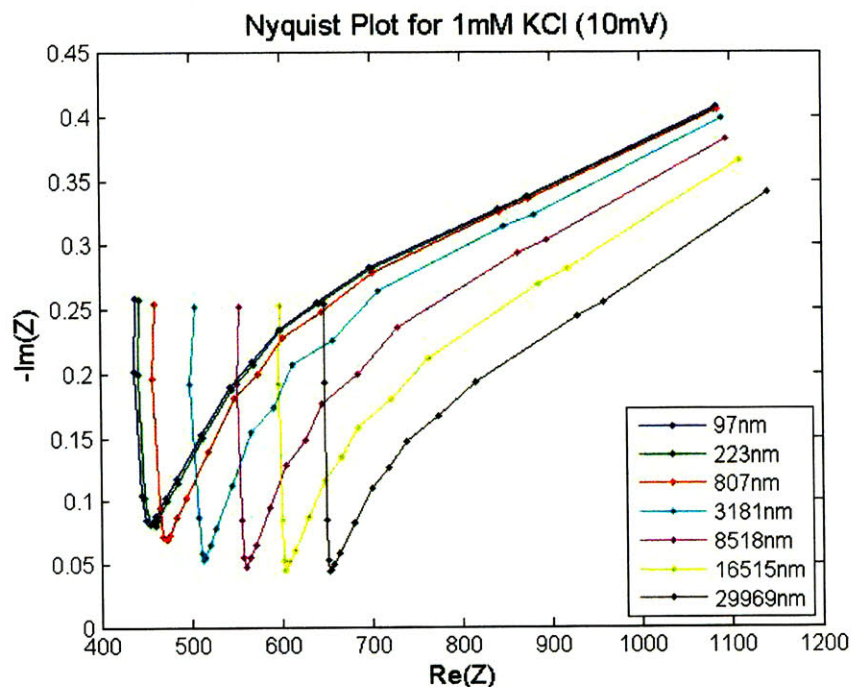


Figure 5.32: Experimental Nyquist diagram of 1 mM KCl solution.

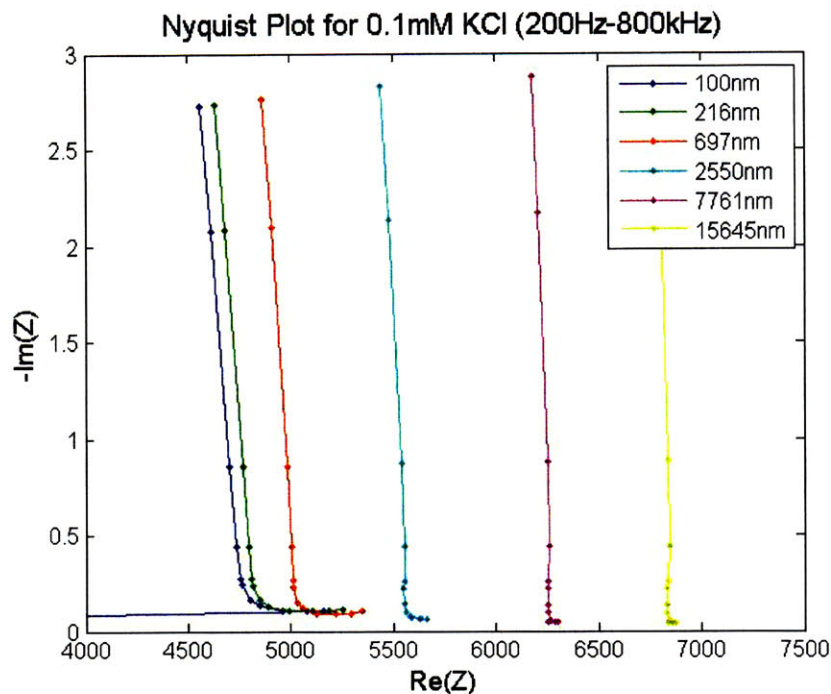


Figure 5.33: Experimental Nyquist diagram of 0.1 mM KCl solution.

5.6 Nanometer Electrode Gaps in Air

As discussed in section 1.7, there is a tremendous amount of interest in creating electrode gaps with nanometer separation as a way to study the electrical properties of nanoscale systems. Specifically, nanometer gaps between macroscopic electrodes could be applied to study the properties of materials confined within nanometer channels. This section studies the feasibility of using the apparatus developed in this thesis to create an adjustable nanometer gap. The first sub-section presents measurements of nanometer electrode gaps in air aimed at determining the minimum electrode separation. The second sub-section presents surface roughness models used to explain deviations of the measured data from idealized models.

5.6.1 Measurement of Nanometer Electrode Gaps in Air

The minimum electrode separation is limited by the defects that cause direct conduction between electrodes before the spherical surfaces come into contact. Defects include both surface roughness of the silicon-nitride substrate and conductive particles adsorbed on the surface of the electrodes. Not all defects restrict the minimum electrode separation. As shown in Figure 5.34, inward facing defects and defects not located at the place of minimum electrode separation do not cause premature direct conduction. Typically, the minimum electrode separation is limited to between 100 nm to 200 nm. After some trials with carefully prepared electrodes, it is possible to find a pair of electrodes free of the problem defects. In this case, much smaller electrode separations can be formed.

Data from one pair of defect-free electrodes are shown in Figure 5.35 using the transform for y from equation (4.7). This data set is taken with the electrodes separated starting at approximately 150 nm apart and decremented in steps of 0.25 nm until the onset of direct conduction. The data shown as been re-sampled once every 1 nm in order to improve the signal-to-noise ratio. The excitation amplitude is 500 mV RMS, while the interelectrode medium is air. In order to prove that this measured data is not an artifact of electrostatic attraction, repeated measurements at 100, 200, 500, and 1000 mV RMS amplitudes are plotted on top of one another in Figure 5.36.

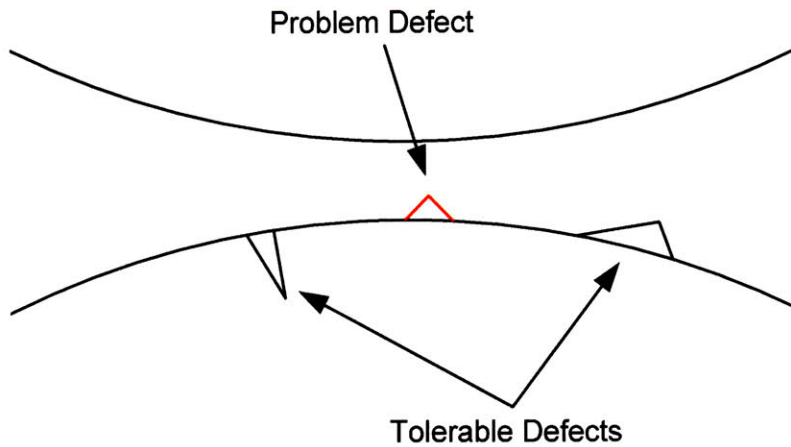


Figure 5.34: Tolerable versus problem defects.

The y versus x curve, in Figure 5.35, forms a straight line with a slope of 1.00 at large electrode separations as expected for air. The y versus x curve begins to depart from the straight line at electrode separations smaller than 40 nm. This departure region can be separated into two parts by considering the slope of the y versus x curve. The first part ranges from 20 to 40 nm where the slope of y versus x is greater than 1. The second part is below 20 nm and the slope is less than 1. As discussed previously, the relative permittivity of the interelectrode medium is equal to the inverse of the slope of the y versus x . Therefore, a slope of less than 1 is not physically possible and the deviation in the first part cannot be explained by dielectric materials trapped between the electrodes. In fact, this deviation can be explained by the native surface roughness of the electrodes which will be discussed in detail in the next sub-section. The second part of the deviation however, is most likely explained by a thin layer of adsorbed water on the surface of the electrodes.

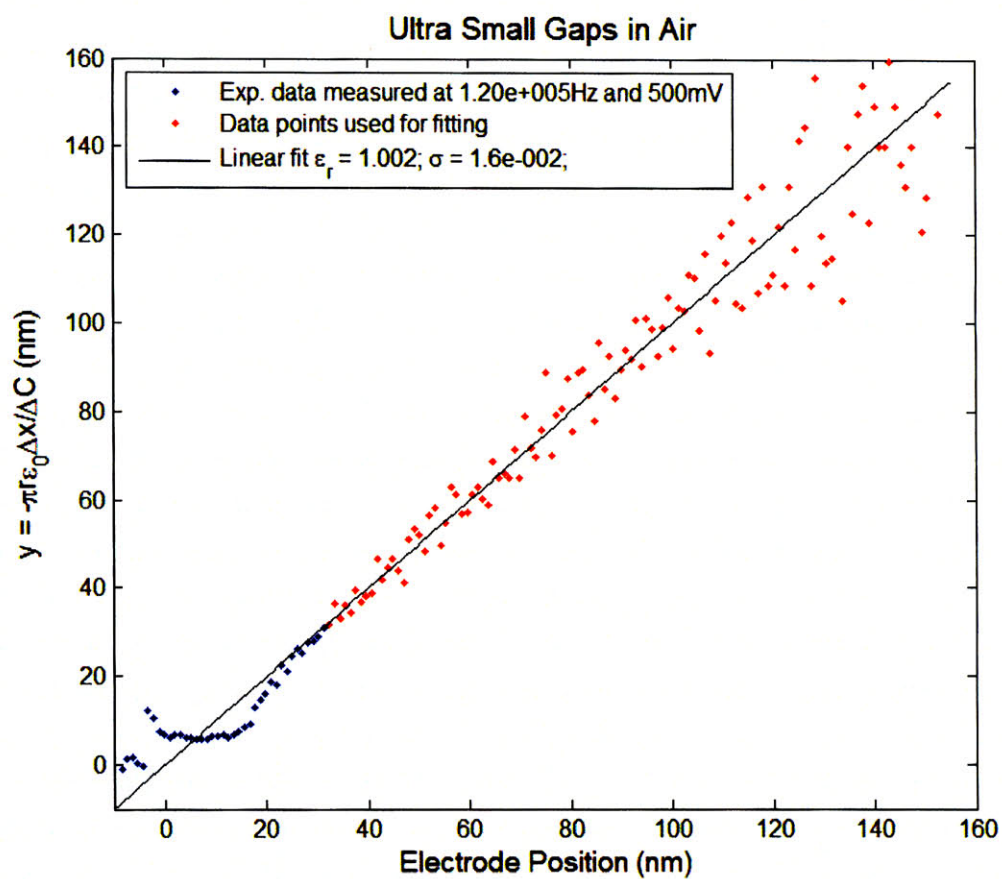


Figure 5.35: Nanometer electrode gaps measured in air. The deviation from the fitting line between 20 and 40 nm could be explained by surface roughness. The deviation from the fitting line below 20 nm is likely a result of surface-bound water.

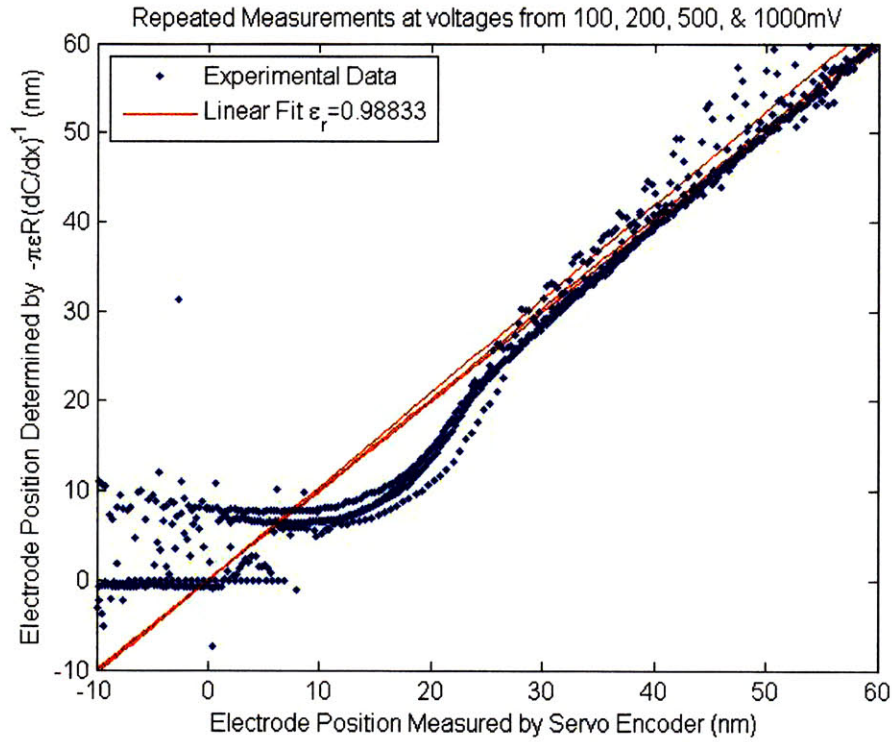


Figure 5.36: Small gap measurements repeated using several different excitation voltages, showing that the measured electrode gap is independent of excitation voltage.

5.6.2 Surface Roughness Model

The surface roughness of the electrodes can be modeled using a probabilistic distribution of the electrode separation as outlined by Boyer [42]. Recall the capacitance between perfectly spherical surfaces that are closely spaced together is described by

$$C = \pi r \epsilon_r \epsilon_0 \ln\left(\frac{2r}{\xi}\right) + C_0, \quad (5.8)$$

Where the spatial derivative is thus

$$\frac{dC}{d\xi} = -\frac{\pi\epsilon r}{\xi}. \quad (5.9)$$

The effect of surface roughness can be added to this model by replacing the electrode separation, ξ using $\xi + z$, where z is described by the probability distribution $h(z)$. This distribution function has a maximum at $z = 0$ and the property that

$$\int h(z) dz = 1. \quad (5.10)$$

The spatial derivative of C thus becomes

$$\frac{dC}{dx} = -\pi\epsilon_0\epsilon_r r \int \frac{h(z)}{(\xi+z)} dz. \quad (5.11)$$

The shape of $h(z)$ is dependent on the nature of the surface roughness of the silicon-nitride substrate. In fact, $h(z)$ is essentially the convolution of the surface roughness distribution functions from the two electrodes. A simple, approximate form of $h(z)$ that is both realistic and aspires convergence of the integral in equation (5.11) is the triangular shape defined by p_1 , p_2 , and h_0 , as shown in Figure 5.37. The value of p_1 and p_2 are not necessarily symmetric, reflecting a possible non-zero skew of the surface roughness of the electrodes. In the region where $z \in [p_1, 0]$, $h(z)$ is described by

$$h(z) = \frac{2}{(p_1 + p_2)p_1} (z + p_1). \quad (5.12)$$

while for $z \in [0, p_2]$, $h(z)$ is described by

$$h(z) = \frac{2}{(p_1 + p_2)p_2} (p_2 - z). \quad (5.13)$$

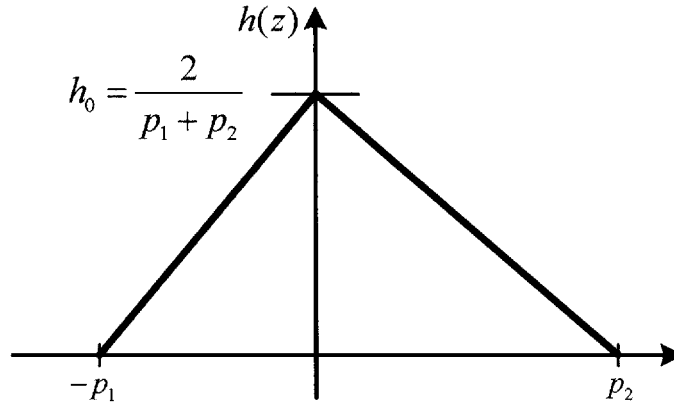


Figure 5.37: Distribution function used to formulate the surface roughness model.

Equation (5.11) can be evaluated in a piece-wise manner, such that

$$\frac{dC}{dx} = -\pi\epsilon_0\epsilon_r r \left(\int_{p_1}^0 \frac{h(z)}{(\xi+z)} dz + \int_0^{p_2} \frac{h(z)}{(\xi+z)} dz \right), \quad (5.14)$$

$$\frac{dC}{dx} = -\pi\epsilon_0\epsilon_r r (I_1 + I_2). \quad (5.15)$$

Evaluating the first integral results in

$$I_1 = \frac{2}{(p_1 + p_2) p_1} \int_{-p_1}^0 \frac{z + p_1}{\xi + z} dz. \quad (5.16)$$

Applying a simple change of variables, $u = \xi + z$, results in

$$I_1 = \frac{2}{(p_1 + p_2) p_1} \int_{u=\xi-p_1}^{u=\xi} \frac{u - \xi + p_1}{u} du. \quad (5.17)$$

Netting the expression

$$I_1 = \frac{2}{(p_1 + p_2) p_1} \left[p_1 + (\xi - p_1) \log \left(1 - \frac{p_1}{\xi} \right) \right]. \quad (5.18)$$

Similarly, the second integral can be evaluated by the expression

$$I_2 = \frac{2}{(p_1 + p_2) p_2} \left[-p_2 + (p_2 + \xi) \log \left(1 + \frac{p_2}{\xi} \right) \right]. \quad (5.19)$$

Inserting these results into equation (5.15) produces the expression

$$\frac{dC}{dx} = -\frac{2\pi\epsilon_0\epsilon_r r}{(p_1 + p_2)} \left[\left(\frac{\xi}{p_1} - 1 \right) \log \left(1 - \frac{p_1}{\xi} \right) + \left(\frac{\xi}{p_2} + 1 \right) \log \left(1 + \frac{p_2}{\xi} \right) \right]. \quad (5.20)$$

Thus, the definition of y is revised as

$$y = \frac{(p_1 + p_2)}{2} \left[\left(\frac{\xi}{p_1} - 1 \right) \log \left(1 - \frac{p_1}{\xi} \right) + \left(\frac{\xi}{p_2} + 1 \right) \log \left(1 + \frac{p_2}{\xi} \right) \right]^{-1}. \quad (5.21)$$

The validity of the revised expression for y can be checked by examining the asymptotic expression of the integral when $\xi \gg p_1, p_2$. In this case, the log terms can be approximated using the series expansion

$$\log(1+y) = y - \frac{1}{2}y^2 + \frac{1}{3}y^3 - \frac{1}{4}y^4 + \dots \quad (5.22)$$

Therefore, expression (5.21) becomes

$$y = \frac{(p_1 + p_2)}{2} \left[\left(\frac{\xi}{p_1} - 1 \right) \left(-\frac{p_1}{\xi} - \frac{p_1^2}{2\xi^2} + \dots \right) + \left(\frac{\xi}{p_2} + 1 \right) \left(\frac{p_2}{\xi} - \frac{p_2^2}{2\xi^2} + \dots \right) \right]. \quad (5.23)$$

Multiplying through and collecting only the first order terms produces

$$y \approx \xi, \quad (5.24)$$

the expected result for the case where $\xi \gg p_1, p_2$.

The surface roughness model superimposed on to the data from Figure 5.35 is shown in Figure 5.38. The values for p_1 and p_2 have been adjusted to 19 nm and 25 nm to obtain the best possible fit. These values are reasonable estimates from the peak-to-valley range of the electrode surface roughness, which are approximately 20 nm. The surface roughness model breaks down below 19 nm as the probabilistic distribution $h(z)$ begins to produce negative values of ξ .

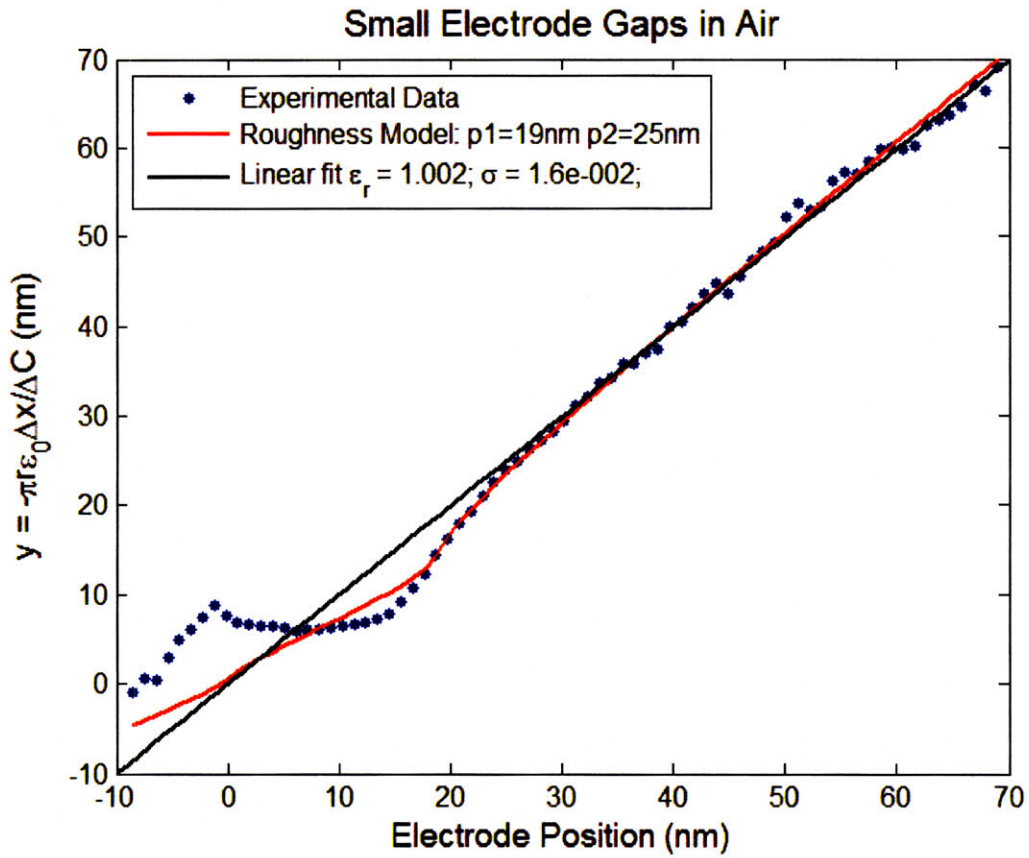


Figure 5.38: The surface roughness model superimposed on to the small electrode gap data from Figure 5.35.

Chapter 6

Conclusions and Future Directions

A method for measuring the electrical permittivity and conductivity of liquids and gases using closely spaced spherical electrodes with adjustable separation has been developed and presented in this thesis. This technique has the advantage of making accurate measurements, without the need for wet calibration, in a manner that is also compatible with miniaturized chemical analysis systems. A separate, but equally important result is the development of a technique for creating nanometer gaps between macroscopic electrodes that can be used for measuring electrical properties of nanoscale systems, as well as liquids and gases in highly confined states. This capability has been verified using the instrument developed in this thesis, which measures electrode gaps of less than 20 nm over a projected area on the order of 1 mm².

6.1 Contributions

Research to accomplish the initial goals of 1) developing accurate permittivity and conductivity measurements of liquids and gases without wet calibration and 2) creating nanometer gaps between macroscopic electrodes resulted in a number of contributions. Initially, the idea of using permittivity and conductivity measurements as a chemical detection technique in miniaturized chemical analysis systems is formulated and

the requirement for wet calibration is identified as a key obstacle. Design rules for impedance test cells that do not require wet calibration has been developed, and a fundamental tradeoff is revealed between the adjustable range of the cell constant and the variance of the parasitic terms. Further investigations indicate that this tradeoff can be optimized at small electrode gaps where the electrode separation is adjusted.

Based on these ideas, an instrument for measuring the electrical impedance between spherical electrodes where the electrode separation is a precisely adjusted small gap has been developed. The components of this system include:

- Platinum electrodes fabricated using silicon-nitride spheres as a substrate.
- A electrode mounting shaft for mechanically constraining the spheres while making electrical contact to the electrode film.
- A flexure mechanism for precisely adjusting the electrode separation by reducing the displacement from a servomechanical actuator while minimizing parasitic displacements. This mechanism has a resolution of 0.25 nm and a range of 50 μm .
- A mechanically isolated metrology frame for measuring the displacement of both electrodes using capacitance probes.
- A temperature control system that maintains constant temperature with 0.1°C resolution.
- A data acquisition system for automating experiment control and data collection.

Electrostatic and electrochemical models describing the measurement scheme have been developed. In particular, a new analysis of the equivalent circuit of the electrochemical model has been presented in Section 3.2.3 using fewer assumptions than

previous analyses [49]. This analysis has been useful for clarifying the relationship between interfacial and bulk impedances in the measured medium.

A rigorous study of analysis techniques for extracting permittivity and conductivity from $C(x)$ and $G(x)$ measurements has been carried out in Chapter 4. Both weighted least squares and non-linear fitting methods has been implemented and evaluated. The non-linear fitting technique is more immune to the systematic errors caused by electrode geometry while the weighted least squares technique is more robust to random errors resulting from uncertainty in the measurement of the sample impedance and electrode displacement.

The operation and accuracy of the instrument developed has been verified using relative permittivity measurements of nitrogen gas and methanol. Without adjustment of the model, the measured results were within 1% of established values. Repeated measurements of 20 samples indicate standard deviations from mean of 0.18% for nitrogen gas and 0.18% for methanol. Additionally, the relative permittivity of 2-propanol and water has also been made as further verifications of this technique.

Measurements of liquid conductivity have been verified using potassium chloride solutions. Although the standard deviations from 20 repeated measurements are within 0.26% of the mean, the measured results were lower than established values by approximately 5%. The activation energy for conduction, however, closely matches that of established value for potassium chloride solutions. Since the equations for describing conductivity are exactly equivalent to the equations describing capacitance, it is concluded that the source of the scale-factor error comes from the composition of the electrolyte and is not an artifact of the measurement technique. The composition of the

electrolyte may have been altered by moisture adsorbed on the walls of the impedance test cell diluting the sample liquid, or by adsorption and corrosion processes at the electrode-electrolyte interface, which modify the ion concentration in the bulk liquid.

The frequency dependence of impedance has been measured for potassium chloride solutions. Impedance measurements as a function of electrode separation and frequency enable independent measurements bulk and interfacial impedance. The measured results highlight potential failures of the Gouy-Chapman-Sterns model to describes the impedance of the electrode-electrolyte interface and motivate the need for more sophisticated models for describing the behavior of electrochemical systems.

Finally, this apparatus has shown capabilities for creating nanometer electrode gaps. Electrode gaps as little as 20 nm have been shown over a projected area on the order of 1 mm². Deviations from models of ideal spheres can be partially explained by the surface roughness of the spherical electrodes.

6.2 Implications and Future Directions

An immediate next step in this work is to develop a disposable version of the impedance test cell presented in this thesis. The single-use nature of this device avoids the sample contamination problems that plague current multi-use devices, while the measurement technique developed in this thesis ensure repeatable measurements without requiring wet calibration. Disposable impedance test cells could be mass-fabricated using injection molding or cast molding. State-of-the-art diamond-turning machines can be used to create molds for spherical electrodes with highly accurate geometries and nanometer-smooth surfaces. The adjustable electrode separation could be achieved using

an electrode array at a series of electrode separations. One possible design for this concept is shown in Figure 6.1. A key parameter for this device is the tolerances on the electrode separation, which represent an uncertainty in the electrode separation. Thus, careful control of the molding processes will be required in order to fabricate reproducible devices. Alternatively, a flexible sample chamber could be developed to allow the electrode separation to be adjusted using an external actuator. Portable, low-cost microactuators [50] are becoming available in response to the demand for image-stabilization systems in digital cameras.

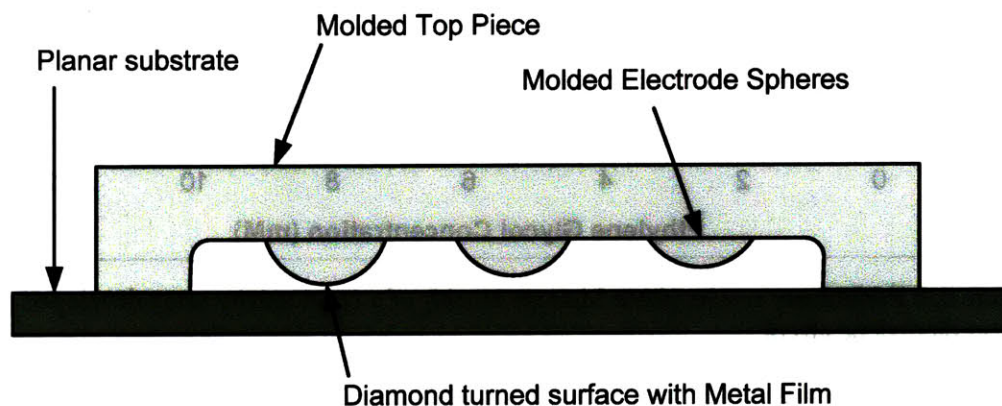


Figure 6.1: A possible design of an injection-molded impedance test cell.

A mass-fabricated impedance test cell is applicable as a sensor for measuring the liquid purity in many industrial applications such as in power generation, chemical and pharmaceutical production, and semiconductor manufacturing. Since wet calibration is not required, simpler and more accurate measurements could be made.

Chemical detection technologies based on the measurement of electrical conductivity could be developed using conductivity assays designed to react with specific substances. This work has already begun with undergraduate Melanie Hoehl at MIT to

develop an enzyme-based conductivity assay for detecting diethylene glycol. Some initial results from this work are shown in Figure 6.2.

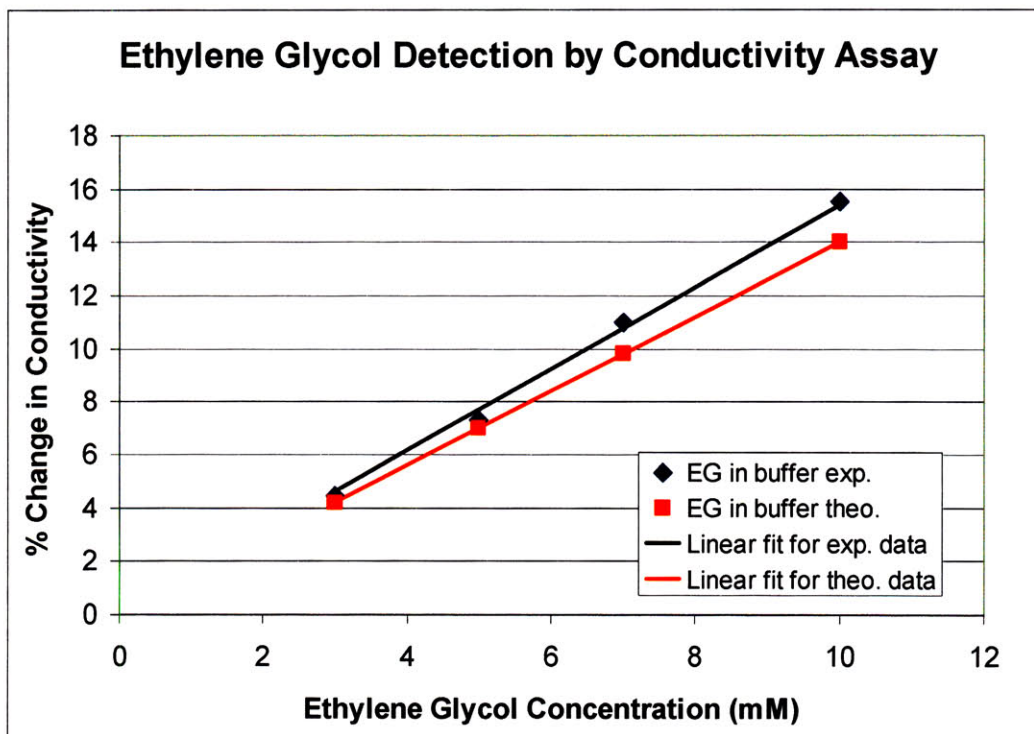


Figure 6.2: Preliminary results (from Melanie Hoehl) of a conductivity assay developed to detect diethylene glycol.

The properties of materials confined within nanometer-thin channels is a fascinating area of research since many natural biochemical processes take place inside nano-confined structures such as cells, organelles, and the intercellular matrix, while current biochemical studies are typically performed in bulk liquid. Some fundamental questions that the current system could begin to address include: “Does the mobility of particles increase or decrease when particles are confined within channels that are similar to their own size?” “Do chemical reaction rates of large chemical compounds increase or decrease when the rotational and translational degrees of freedom are reduced?”

Aspects of the first question could begin to be tackled by measuring the concentration of nanoparticles in different sizes of electrode gap as illustrated in Figure

6.3. Nanoparticles made of polystyrene, melamine resin, and latex typically have relative permittivity values from 2 to 3, while water has a relative permittivity of approximately 80. Given the tremendous dielectric contrast between these materials, the concentration of nanoparticles in water can be measured by the relative permittivity of the suspension. This capability is made possible by the fact that the instrument developed is capable of measuring permittivity accurate to within 1%.

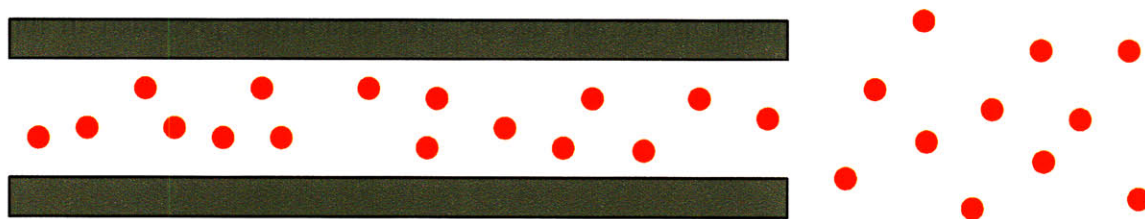


Figure 6.3: Illustration of the experiment for measuring nanoparticle mobility in gap.

As the electrode separation is adjusted from large to small, the concentration of the particles in the electrode gap region could be used to measure the differential mobility of nanoparticles. If the mobility of the nanoparticles decreases at smaller electrode gaps, then the concentration of nanoparticles should increase within the small gap region compared to the bulk region. If the mobility of the nanoparticles increase at smaller electrode gaps, then the concentration of the nanoparticles should decrease as the electrode gap is reduced. By experimenting with different size and concentration of nanoparticles, a coherent theory of nanoparticle mobility maybe developed with the help of appropriate hydrodynamic models. These experiments will be important in drug deliver for determining the ability of nanoparticles to move through tissue, and for developing methods for specifically targeting certain tissues.

A similar experiment could also be developed for measuring the mobility and reaction rates of macromolecules in high confined spaces. In this case, the concentration

of macromolecules can be measured conductivity, which is a reflection of the ability of the molecule to attract charge carriers.

Ultimately, the adjustable nanometer gap electrode instrument developed in this thesis will be an enabling technology for the development of chemical detectors in miniaturized chemical analysis systems, as well as, the study of the properties of materials confined in nanoscale systems. Since both of these research topics have gathered tremendous momentum in the last decade, the capabilities presented in this thesis will open up a plethora of new research opportunities.

References

- [1] T. Thorsen, S. J. Maerkl, and S. R. Quake, "Microfluidic large-scale integration," *Science*, vol. 298, pp. 580-584, Oct 18 2002.
- [2] W. Bogdanich and J. Hooker, "From China to Panama, a Trail of Poisoned Medicine," in *The New York Times* New York, NY, 2007.
- [3] M. Hanif, M. R. Mobarak, A. Ronan, D. Rahman, J. J. Donovan, and M. L. Bennish, "Fatal Renal-Failure Caused by Diethylene Glycol in Paracetamol Elixir - the Bangladesh Epidemic," *British Medical Journal*, vol. 311, pp. 88-91, Jul 8 1995.
- [4] W. Bogdanich, "Toxic Toothpaste Made in China is Found in U.S.," in *The New York Times* New York, 2007.
- [5] Y. C. Wu and P. A. Berezansky, "Low Electrolytic Conductivity Standards," *Journal of the Research of the National Institute of Standards and Technology*, vol. 100, pp. 521-527, 1995.
- [6] H. Schlizio, "Optimization of feed and boiler water quality in the power plant of the Aarberg sugar factory," *Zuckerindustrie*, vol. 132, pp. 18-24, Jan 2007.
- [7] J. Y. Lee and S. H. Song, "Evaluation of groundwater quality in coastal areas: implications for sustainable agriculture," *Environmental Geology*, vol. 52, pp. 1231-1242, Jul 2007.
- [8] S. Colombie, E. Latrille, and J. M. Sablayrolles, "Online estimation of assimilable nitrogen by electrical conductivity measurement during alcoholic fermentation in enological conditions," *Journal of Bioscience and Bioengineering*, vol. 103, pp. 229-235, Mar 2007.
- [9] J. K. Duchowski and H. Mannebach, "A novel approach to predictive maintenance: A portable, multi-component MEMS sensor for on-line monitoring of fluid condition in hydraulic and lubricating systems," *Tribology Transactions*, vol. 49, pp. 545-553, Oct-Dec 2006.
- [10] S. L. Shiefelbein, N. A. Fried, K. G. Rhoads, and D. R. Sadoway, "A High-Accuracy Calibration-Free Technique for Measuring the Electrical Conductivity of Liquids," *Review of Scientific Instruments*, vol. 69, 1998.
- [11] E. F. Treo, C. J. Felice, M. C. Tirado, M. E. Valentinuzzi, and D. O. Cervantes, "Hematocrit measurement by dielectric spectroscopy," *IEEE Transactions on Biomedical Engineering*, vol. 52, pp. 124-127, Jan 2005.
- [12] J. M. Fouke, A. D. Wolin, K. G. Saunders, M. R. Neuman, and E. R. Mcfadden, "Sensor for Measuring Surface Fluid Conductivity In vivo," *Ieee Transactions on Biomedical Engineering*, vol. 35, pp. 877-881, Oct 1988.
- [13] S. Oh, J. S. Lee, K. H. Jeong, and L. P. Lee, "Minimization of Electrode Polarization Effect by Nanogap Electrodes for Biosensor Applications," in *IEEE MEMS2003*, Kyoto, Japan, 2003, pp. 52-55.

- [14] J. Barthel, F. Feuerlein, R. Neueder, and R. Wachter, "Calibration of Conductance Cells at Various Temperatures," *Journal of Solution Chemistry*, vol. 9, pp. 209-219, 1980.
- [15] J. Barthel, M. Krell, L. Iberl, and F. Feuerlein, "Conductance of 1-1 Electrolytes in Methanol Solutions from -45-Degrees-C to + 25-Degrees-C," *Journal of Electroanalytical Chemistry*, vol. 214, pp. 485-505, Dec 10 1986.
- [16] Y. C. Wu, K. W. Pratt, and W. F. Koch, "Determination of the Absolute Specific Conductance of Primary Standard KCl Solutions," *Journal of Solution Chemistry*, vol. 18, pp. 515-528, Jun 1989.
- [17] J. Barthel and R. Neueder, *Electrolyte data collection*. Frankfurt/Main, Germany: DECHEMA, 1992.
- [18] P. Vanysek, "Equivalent Conductivity of Electrolytes in Aqueous Solution," in *CRC Handbook of Chemistry and Physics*, 87th ed, D. R. Lide, Ed.: CRC Press, 2007, pp. 5-75.
- [19] J. K. Gimzewski and C. Joachim, "Nanoscale science of single molecules using local probes," *Science*, vol. 283, pp. 1683-1688, Mar 1999.
- [20] X. D. Cui, A. Primak, X. Zarate, J. Tomfohr, O. F. Sankey, A. L. Moore, T. A. Moore, D. Gust, G. Harris, and S. M. Lindsay, "Reproducible measurement of single-molecule conductivity," *Science*, vol. 294, pp. 571-574, Oct 2001.
- [21] J. M. van Ruitenbeek, A. Alvarez, I. Pineyro, C. Grahmann, P. Joyez, M. H. Devoret, D. Esteve, and C. Urbina, "Adjustable nanofabricated atomic size contacts," *Review of Scientific Instruments*, vol. 67, pp. 108-111, Jan 1996.
- [22] C. Zhou, C. J. Muller, M. R. Deshpande, J. W. Sleight, and M. A. Reed, "Microfabrication of a Mechanically Controllable Break Junction in Silicon," *Applied Physics Letters*, vol. 67, pp. 1160-1162, Aug 21 1995.
- [23] H. Park, A. K. L. Lim, A. P. Alivisatos, J. Park, and P. L. McEuen, "Fabrication of metallic electrodes with nanometer separation by electromigration," *Applied Physics Letters*, vol. 75, pp. 301-303, Jul 12 1999.
- [24] A. F. Morpurgo, C. M. Marcus, and D. B. Robinson, "Controlled fabrication of metallic electrodes with atomic separation," *Applied Physics Letters*, vol. 74, pp. 2084-2086, Apr 5 1999.
- [25] G. C. Gazzadi, E. Angeli, P. Facci, and S. Frabboni, "Electrical characterization and Auger depth profiling of nanogap electrodes fabricated by I-2-assisted focused ion beam," *Applied Physics Letters*, vol. 89, Oct 2006.
- [26] A. Kanda, M. Wada, Y. Hamamoto, and Y. Ootuka, "Simple and Controlled Fabrication of Nanoscale Gaps Using Double-Angle Evaporation," *Physica E*, vol. 29, pp. 707-711, 2005.
- [27] J. Lefebvre, M. Radosavljevic, and A. T. Johnson, "Fabrication of nanometer size gaps in a metallic wire," *Applied Physics Letters*, vol. 76, pp. 3828-3830, Jun 19 2000.
- [28] M. T. Gonzalez, S. M. Wu, R. Huber, S. J. van der Molen, C. Schonenberger, and M. Calame, "Electrical conductance of molecular junctions by a robust statistical analysis," *Nano Letters*, vol. 6, pp. 2238-2242, Oct 2006.
- [29] J. N. Israelachvili, "Measurement of Vanderwaals Dispersion Forces in Range 1.5 to 130 nm," *Proceedings of the Royal Society of London Series A - Mathematical and Physical Sciences*, vol. 331, 1972.

- [30] J. N. Israelachvili, *Intermolecular and Surface Forces*, 2nd ed. San Diego, CA: Academic Press, 1992.
- [31] D. Tabor and R. H. S. Winterton, "The Direct Measurement of Normal and Retarded van der Waal Forces," *Proceedings of the Royal Society of London Series A - Mathematical and Physical Sciences*, vol. 312, pp. 435-450, 1969.
- [32] P. Frantz, N. Agrait, and M. Salmeron, "Use of capacitance to measure surface forces .1. Measuring distance of separation with enhanced spatial and time resolution," *Langmuir*, vol. 12, pp. 3289-3294, Jun 26 1996.
- [33] P. Frantz, A. Artsyukhovich, R. W. Carpick, and M. Salmeron, "Use of capacitance to measure surface forces .2. Application to the study of contact mechanics," *Langmuir*, vol. 13, pp. 5957-5961, Oct 1997.
- [34] Y. K. Cho and S. Granick, "A surface forces platform for dielectric measurements," *Journal of Chemical Physics*, vol. 119, pp. 547-554, Jul 2003.
- [35] J. M. Georges, S. Millot, J. L. Loubet, and A. Tonck, "Drainage of Thin Liquid-Films between Relatively Smooth Surfaces," *Journal of Chemical Physics*, vol. 98, pp. 7345-7360, May 1993.
- [36] A. Tonck, J. M. Georges, and J. L. Loubet, "Measurements of Intermolecular Forces and the Rheology of Dodecane between Alumina Surfaces," *Journal of Colloid and Interface Science*, vol. 126, pp. 150-163, Nov 1988.
- [37] F. Restagno, J. Crassous, E. Charlaix, C. Cottin-Bizonne, and M. Monchanin, "A new surface forces apparatus for nanorheology," *Review of Scientific Instruments*, vol. 73, pp. 2292-2297, Jun 2002.
- [38] F. Houze and L. Boyer, "A Quantitative Approach to the Effects of Surface-Topography on Tunneling Current between 2 Large Rough Metal Bodies," *Journal of Physics-Condensed Matter*, vol. 3, pp. 4655-4675, Jun 1991.
- [39] A. Tonck, F. Houze, L. Boyer, J. L. Loubet, and J. M. Georges, "Electrical and Mechanical Contact between Rough Gold Surfaces in Air," *Journal of Physics-Condensed Matter*, vol. 3, pp. 5195-5201, Jul 8 1991.
- [40] A. H. Slocum, "Flexural Bearings," in *Precision Machine Design* Dearborn, Michigan: Society of Manufacturing Engineers, 1992, p. 521.
- [41] "Agilent Technologies Impedance Measurement Handbook," 2006.
- [42] L. Boyer, F. Houze, A. Tonck, J. L. Loubet, and J. M. Georges, "The Influence of Surface-Roughness on the Capacitance between a Sphere and a Plane," *Journal of Physics D-Applied Physics*, vol. 27, pp. 1504-1508, Jul 14 1994.
- [43] M. Z. Bazant, K. T. Chu, and B. J. Bayly, "Current-Voltage Relations for Electrochemical Thin Films," *J. Appl. Math.*, vol. 65, pp. 1463-1484, 2005.
- [44] M. Z. Bazant, K. Thorton, and A. Ajdari, "Diffuse-charge dynamics in electrochemical systems," *Phys. Rev. E*, vol. 70, 2005.
- [45] G. Barbero, A. M. Figueiredo, F. C. M. Freire, and M. Scalerandi, "Frequency dependence of the electrical impedance of electrolytic cells: The role of the ionic adsorption/desorption phenomena and the Stern layer," *Physics Letters A*, vol. 360, pp. 179-182, Dec 18 2006.
- [46] J. B. Bates, Y. T. Chu, and W. T. Stribling, "Surface-Topography and Impedance of Metal-Electrolyte Interfaces," *Physical Review Letters*, vol. 60, pp. 627-630, Feb 15 1988.

- [47] A. J. Bard and L. R. Faulkner, *Electrochemical Methods: Fundamentals and Applications*. New York: John Wiley, 2001.
- [48] J. O. M. Bockris and A. K. N. Reddy, *Modern electrochemistry; an introduction to an interdisciplinary area [by] John O'M. Bockris and Amulya K. N. Reddy*. New York,: Plenum Press, 1970.
- [49] H. P. Schwan, "Linear and Nonlinear Electrode Polarization and Biological-Materials," *Annals of Biomedical Engineering*, vol. 20, pp. 269-288, 1992.
- [50] "www.newscaletech.com/squiggle_overview.html."

Appendix A: Mechanical Drawings

Drawing 1: Ring nut for constraining and making electrical contact with the electrode sphere

Drawing 2: Electrode mounting shaft

Drawing 3: Sample chamber

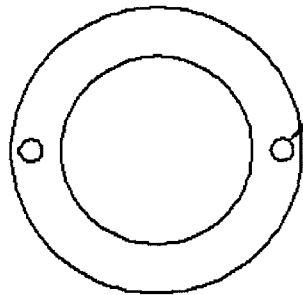
Drawing 4: Clamp for securing the electrode mounting shafts onto the flexure

Drawing 5: Supporting attachment for the coarse actuator

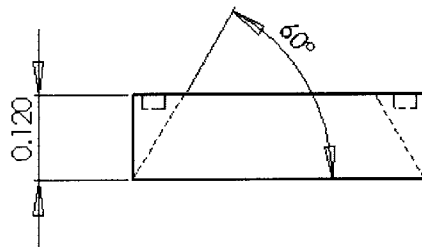
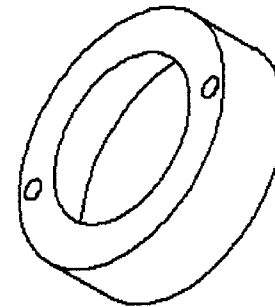
Drawing 6: Attachment for the bottom capacitance probe

Drawing 7: Steel puck for interfacing with the coarse actuator

Drawing 8: Flexure fabrication drawing



~1/32 hole
Please make tool for tightening



Threaded for
7/16-32 UN

PROPRIETARY AND CONFIDENTIAL
Hongshen Ma
MASSACHUSETTS INSTITUTE OF TECHNOLOGY
CONTACT: HONGMA@MIT.EDU
DATE:

5

NOTE:
Contact:
Hong Ma
617-680-7578
hongma@mit.edu

MATERIAL 316 SS

FINISH

3

UNLESS OTHERWISE SPECIFIED:

DIMENSIONS ARE IN INCHES
TOLERANCES:
FRACTIONAL ±
ANGULAR: MACH ± BEND ±

TITLE: Cap Ring
Qty=4

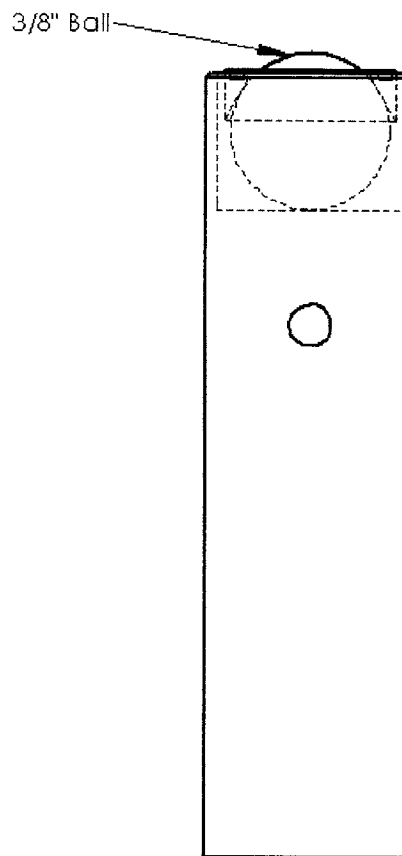
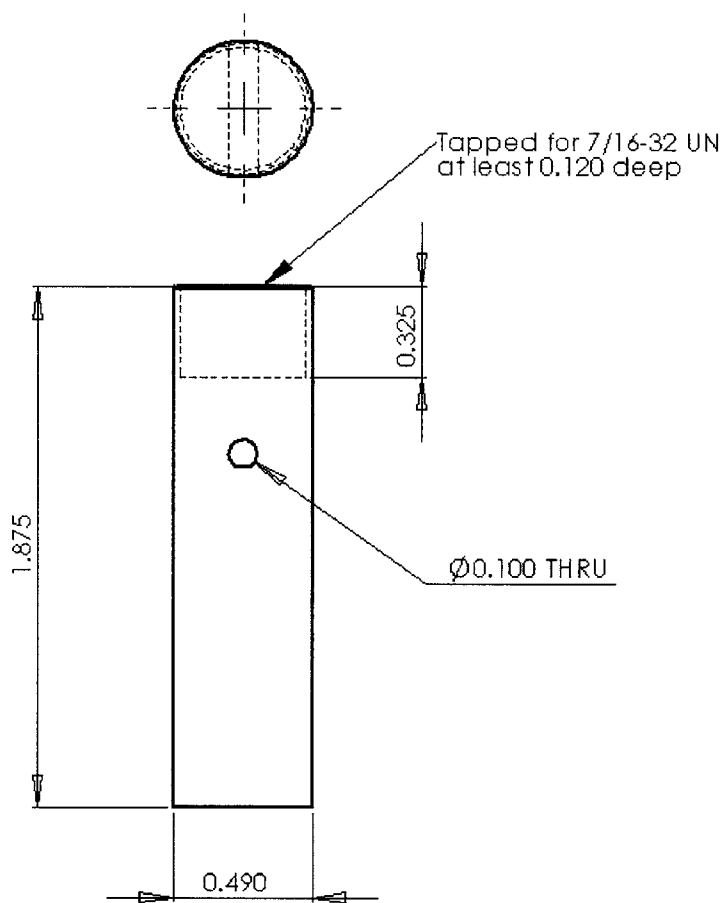
SCALE:

2

REV

SHEET 1 OF 1

1



Assembled View
3:1 Scale

PROPRIETARY AND CONFIDENTIAL
 Hongshen Ma
 MASSACHUSETTS INSTITUTE OF TECHNOLOGY
 CONTACT: HONGMA@MIT.EDU
 DATE:

5

NOTES:
 Contact:
 Hong Ma
 617-680-7578
 hongma@mit.edu

MATERIAL 316 SS

FINISH

3

UNLESS OTHERWISE SPECIFIED:

DIMENSIONS ARE IN INCHES
 DECIMALS:
 FRACTIONS:
 ANGULAR: MACH ± BEND ±

2

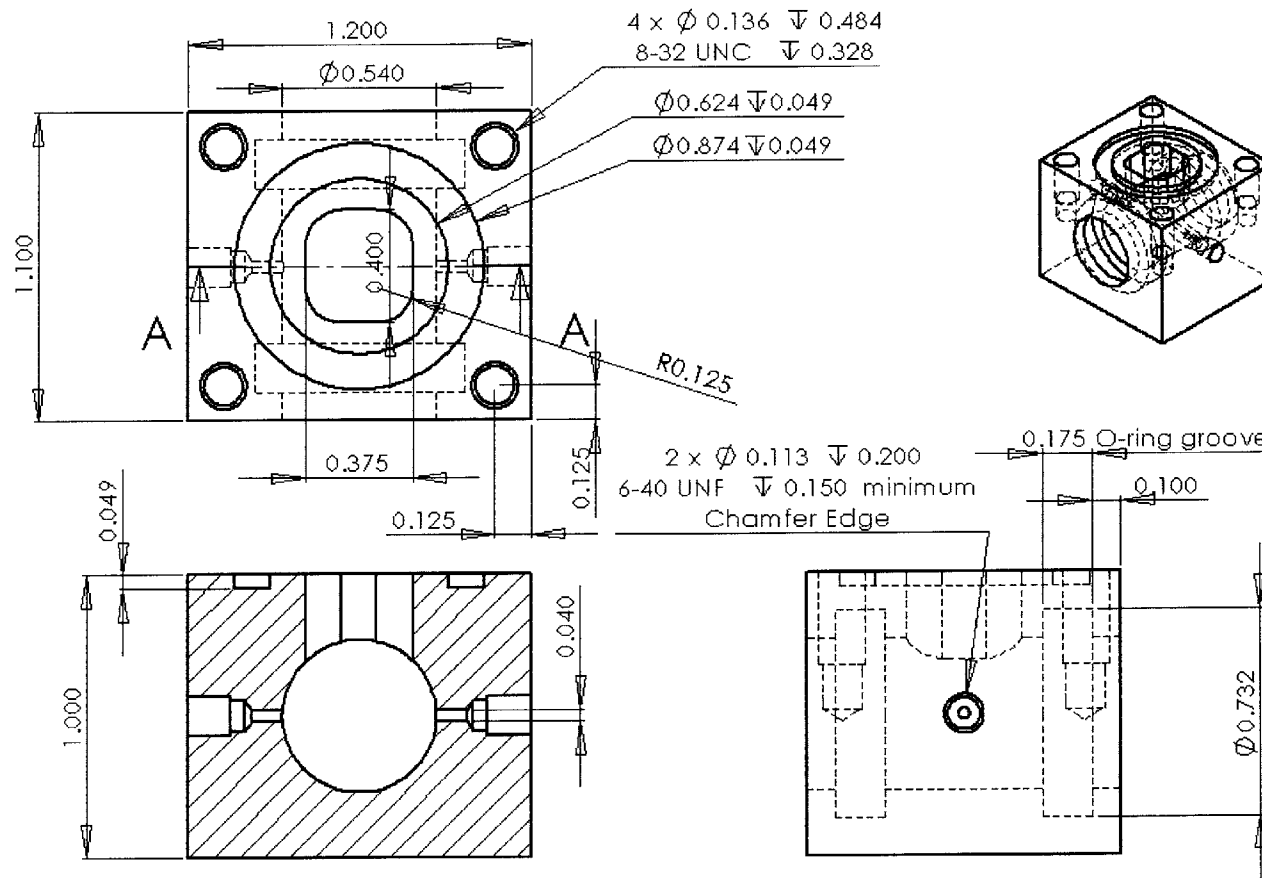
TITLE: Electrode Shaft
 Qty=4

SCALE:

REV

SHEET 1 OF 1

1



PROPRIETARY AND CONFIDENTIAL
 Hongshen Ma
 MASSACHUSETTS INSTITUTE OF TECHNOLOGY
 CONTACT: HONGMA@MIT.EDU
 DATE:

5

NOTE:
 Contact:
 Hong Ma
 617-680-7578
 hongma@mit.edu

4

MATERIAL 316 SS
 FINISH

3

UNLESS OTHERWISE SPECIFIED:
 DIMENSIONS ARE IN INCHES
 TOLERANCES:
 FRACTIONAL \pm
 ANGULAR: MACH \pm BEND \pm

2

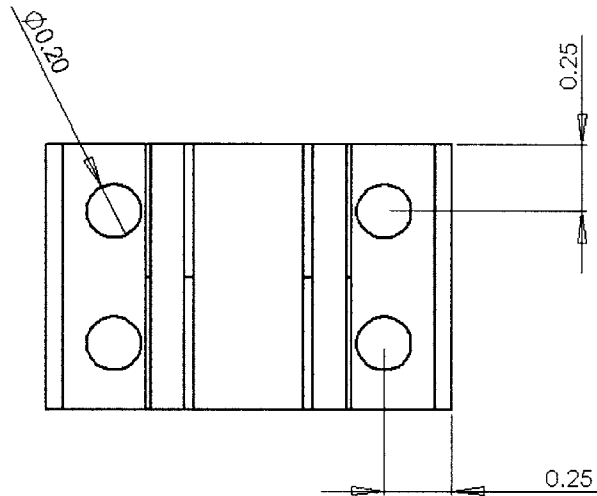
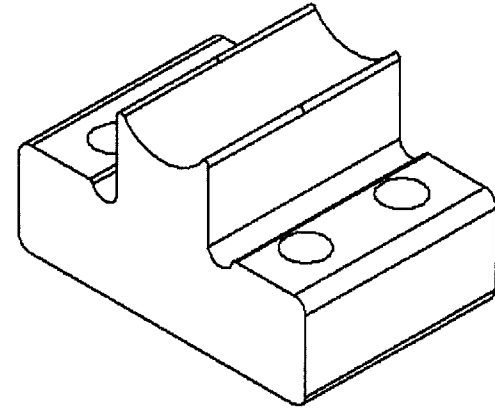
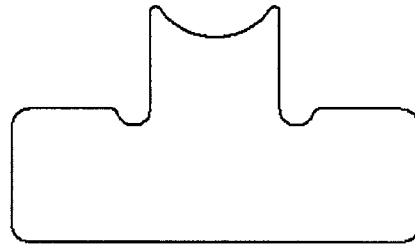
TITLE: Sample Chamber
 Qty=2

SCALE:

REV

SHEET 1 OF 1

1



PROPRIETARY AND CONFIDENTIAL
 Hongshen Ma
 MASSACHUSETTS INSTITUTE OF TECHNOLOGY
 CONTACT: HONGMA@MIT.EDU
 DATE:

NOTES:

MATERIAL

FR38H

UNLESS OTHERWISE SPECIFIED:

DIMENSIONS ARE IN INCHES
 TOLERANCES:
 FRACTIONAL ±
 ANGULAR: MACH ± BEND ±

TITLE:

SCALE:

REV

SHEET 1 OF 1

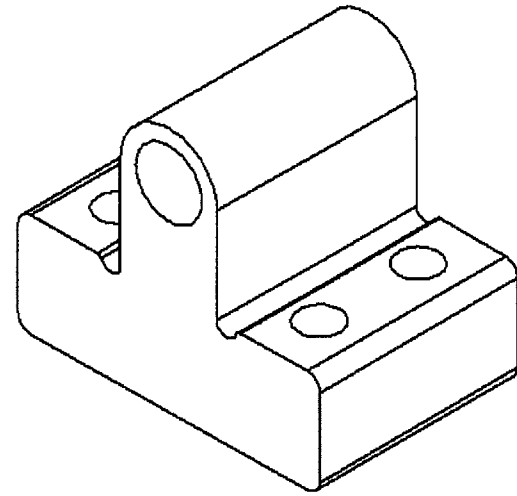
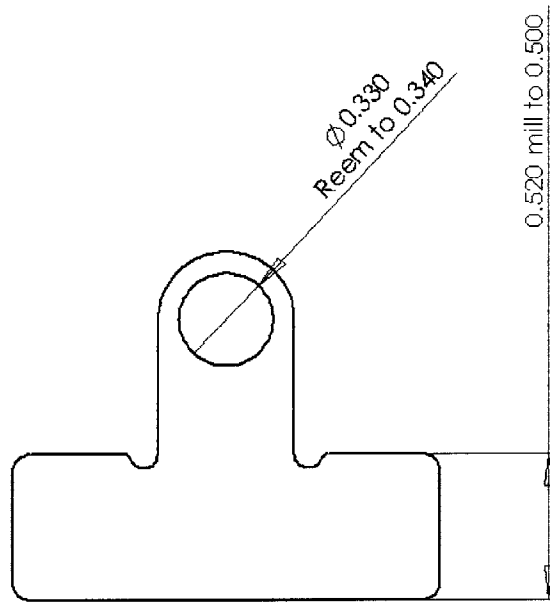
5

4

3

2

1



PROPRIETARY AND CONFIDENTIAL
 Hongshen Ma
 MASSACHUSETTS INSTITUTE OF TECHNOLOGY
 CONTACT: HONG.MA@MIT.EDU
 DATE:

5

NOTES:

4

MATERIAL

FINISH

3

UNLESS OTHERWISE SPECIFIED:

DIMENSIONS ARE IN INCHES
 TOLERANCES:
 FRACTIONAL \pm
 ANGULAR: MACH \pm BEND \pm

2

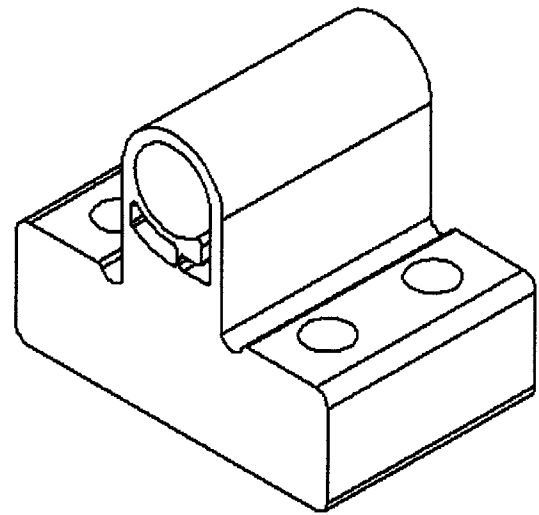
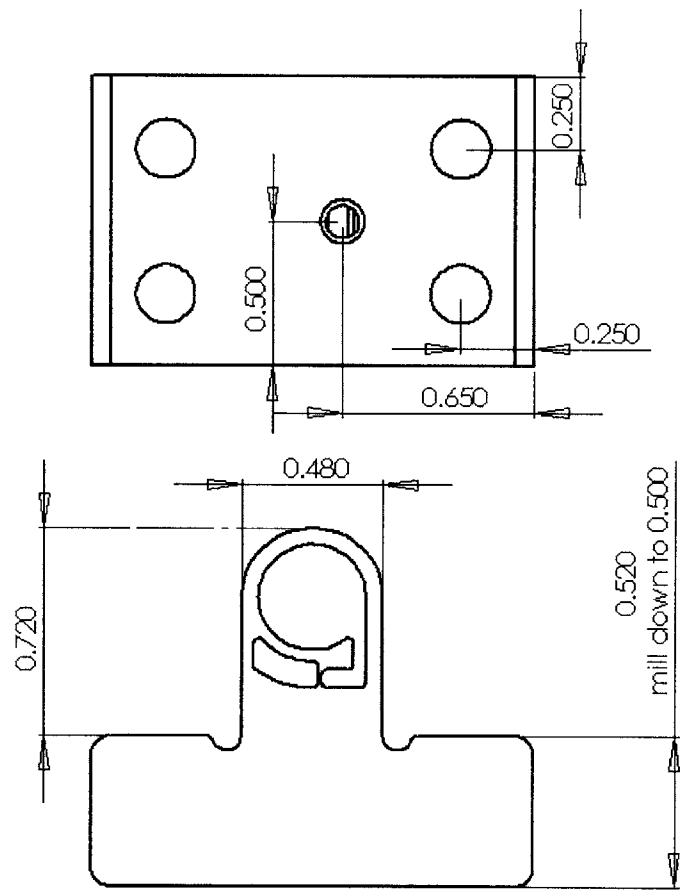
TITLE:

SCALE:

REV

SHEET 1 OF 1

1



PROPRIETARY AND CONFIDENTIAL
 Hongshen Ma
 MASSACHUSETTS INSTITUTE OF TECHNOLOGY
 CONTACT: HONGMA@MIT.EDU
 DATE:

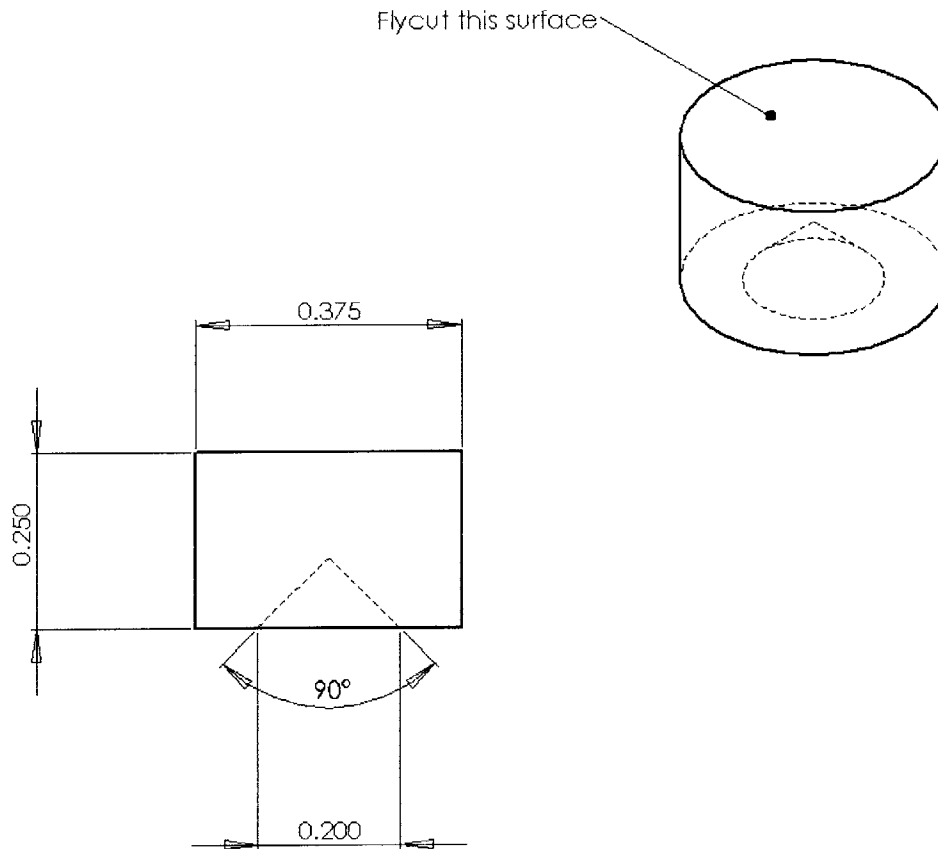
NOTE:

MATERIAL
 FINISH

UNLESS OTHERWISE SPECIFIED:
 DIMENSIONS ARE IN INCHES
 TOLERANCES:
 FRACTIONAL ±
 ANGULAR: MACH 1 BEND 2

TITLE:
 SCALE:

REV
 SHEET 1 OF 1



PROPRIETARY AND CONFIDENTIAL
 Hongshen Ma
 MASSACHUSETTS INSTITUTE OF TECHNOLOGY
 CONTACT: HONGMA@MIT.EDU
 DATE:

5

NOTES:
 Qty = 1
 hongma@mit.edu
 617-680-7578

4

MATERIAL
 Mild Steel
 FINISH

3

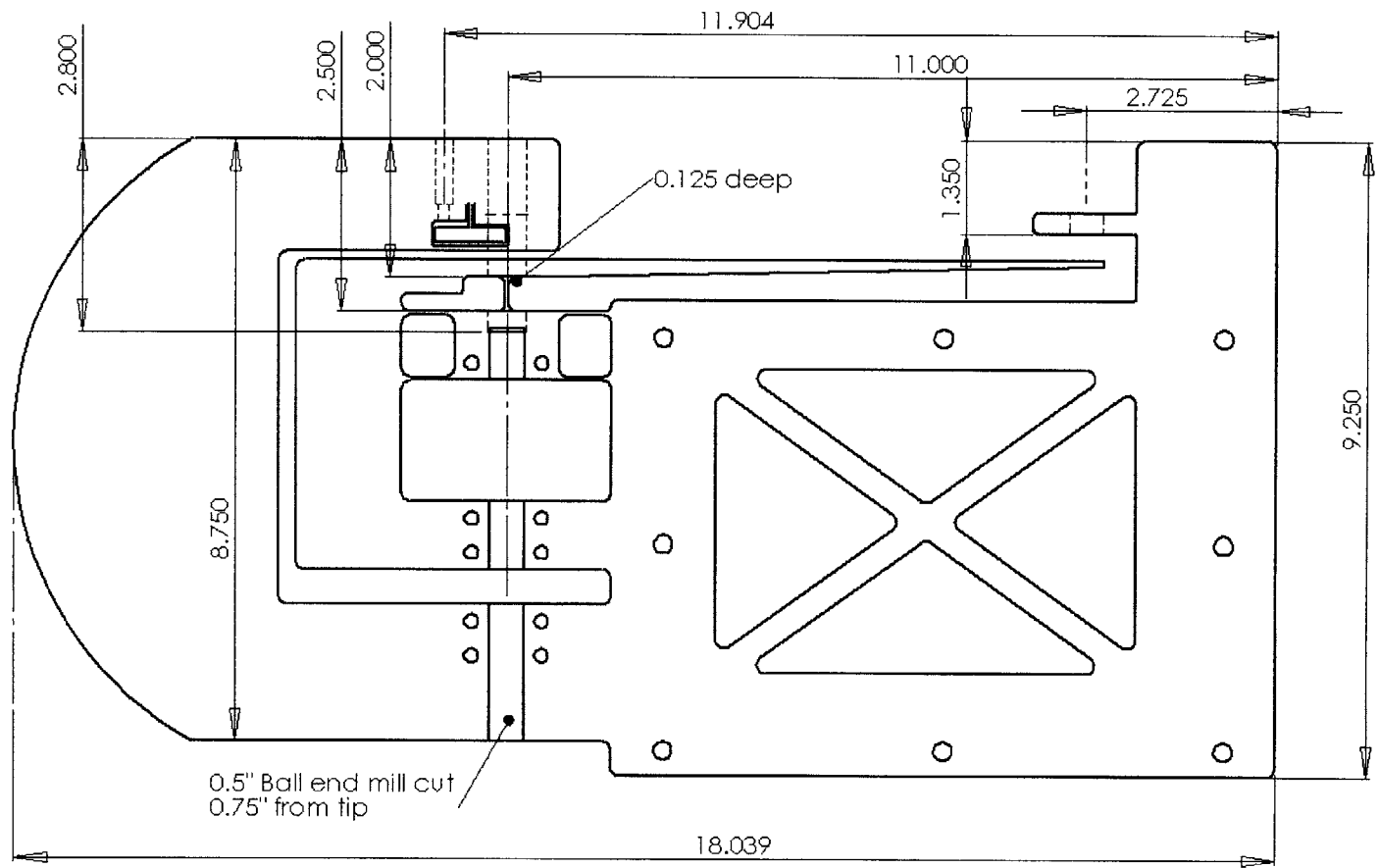
UNLESS OTHERWISE SPECIFIED:
 DIMENSIONS ARE IN INCHES
 TOLERANCES:
 FRACTIONAL: \pm
 ANGULAR: MACH \pm BEND \pm

2

TITLE: Steel Puck
 Drawing 4/4
 SCALE:

1

REV
 SHEET 1 OF 1



PROPRIETARY AND CONFIDENTIAL
 Hongshen Ma
 MASSACHUSETTS INSTITUTE OF TECHNOLOGY
 CONTACT: HONGMA@MIT.EDU
 DATE:

NOTES:
 5
 4

MATERIAL
 FINISH
 3

UNLESS OTHERWISE SPECIFIED:
 DIMENSIONS ARE IN INCHES
 TOLERANCES:
 FRACTIONAL: ±
 ANGULAR: MACH ±
 BEND ±
 2

TITLE: Flexure Hole drilling
 Guide
 SCALE: 2:1

REV
 SHEET 1 OF 1
 1

Appendix B: MATLAB Code

Main Data Analysis Routine

```
% Accufit.m script
% Created by Hong Ma, May 12, 2007

%% Standard Constants
r=0.0047625635;
%r=0.00635;
e0=8.85418782e-12;
% Substance Definition for Plotting Purposes
substance='Air';
% substance='Methanol';
% substance='DI Water';
% substance='0.1mM KCl Solution';
% substance='1mM KCl Solution';
% substance='10mM KCl Solution';
% substance='N_2 Gas';

%% Read in values from file

[time, freq, cp, rp, capnm, capv, servomm, capv2, capnm2, biasmv, temp1, temp2,
temp3, temp4, ampmv] = textread(file, '%f%f%f%f%f%f%f%f%f%f%f',
'delimiter', ',', 'headerlines', 1, 'commentstyle', 'c++');
capnm=capnm+capnm2-min(capnm+capnm2);
servomm=max(servomm)-servomm;
avgfreq=mean(freq); % Determine the frequency of the current data
set
filebad=0; % Bad data flag
% Determine the temperature of the current data set
avgtemp1=mean(temp1); % Temp probe 1 mounted on the sample chamber
avgtemp2=mean(temp2); % Temp probe 2 mounted at the center of the
flexure
avgtemp3=mean(temp3); % Temp probe 3 mounted on the left hand side of
the flexure
avgtemp4=mean(temp4); % Temp probe 4 mounted on the right hand side
of the flexure
amp=mean(ampmv); % Determine the amplitude of the excitation
signal
bias=mean(biasmv); % Determine the value of the DC bias

% Remove multiple data points measured at the same electrode position
servo_single=-ones(length(servomm),1);
cap_servo_single=zeros(length(servomm),1);
cp_single=zeros(length(servomm),1);
rp_single=zeros(length(servomm),1);
for i=1:length(servomm)
    x=find(servomm==servomm(i));
    if ((length(x)>1)&&(x(1)~=i))
        %do nothing!
    else
        servo_single(i)=mean(servomm(find(servomm==servomm(i))));
        cp_single(i)=mean(cp(find(servomm==servomm(i))));
        cap_servo_single(i)=mean(capnm(find(servomm==servomm(i))));
        rp_single(i)=mean(rp(find(servomm==servomm(i))));
    end
end
```

```

    end
end
servomm=servo_single(find(servo_single~-1));
cp=cp_single(find(servo_single~-1));
rp=rp_single(find(servo_single~-1));
capnm=cap_servo_single(find(servo_single~-1));

%This part is used to take a subset of the dataset
indices=1:length(find(servomm~=servomm(length(servomm))));
servomm=servomm(indices);
cp=cp(indices);
rp=rp(indices);
capnm=capnm(indices);

%% Determined and plot the transmission ratio of the flexure
fitx2=1e6*servomm(find((servomm>0.1*max(servomm))&(servomm<0.9*max(servomm))));
fity2=capnm(find((servomm>0.1*max(servomm))&(servomm<0.9*max(servomm))));
[fitresult2 goodness]=fit(fitx2, fity2, 'poly1', 'robust', 'LAR');
fitline2=fitresult2.p1*fitx2+fitresult2.p2;
if seepplot>=5
    figure(20); %Plot Transfer Function
    plot(1e6*servomm, capnm, '.b', fitx2, fitline2, '-r');
    xlabel('Position Derived from Servo Encoder (nm)');
    ylabel('Position Measured by Capacitance Probe');
    legend('Servo vs. Cap Probe', ['Fit line slope='
num2str(1./fitresult2.p1)], 'location', 'northwest');
end

servonm=1e6*servomm*fitresult2.p1;

% Reverse the order of the datapoints
reverseservo=zeros(length(servonm), 1);
reversecp=zeros(length(servonm), 1);
reverserp=zeros(length(servonm), 1);
reversecapnm=zeros(length(servonm), 1);
for i=1:length(servonm)
    reverseservo(i)=servonm(length(servonm)-i+1);
    reversecp(i)=cp(length(servonm)-i+1);
    reverserp(i)=rp(length(servonm)-i+1);
    reversecapnm(i)=capnm(length(servonm)-i+1);
end
servonm=reverseservo;
cp=reversecp;
rp=reverserp;
capnm=reversecapnm;
servonm=reversecapnm;

% We can measure electrode position using the two capacitance probes or using
% the servo encoder scale by the flexure transmission ratio. We will use
% the former in our analysis, this is implemented by above statement

%% Simulated data
% When uncommented, the following statements generate a simulated data set
% for evaluating the data analysis procedure

% noise_level=10e-16;
% %temp servo=100:25:2000;
% temp servo=3000:500:35000; %large range
% servonm=temp servo';
% %c0=noise_level*(rand(1, length(servonm))-0.5); %generate random error
% c0=0;
% fakeer=1;

```

```

% setxi0=0.0022;
% area=9.1e-5;          %Area of the electrode mounting area
% c1=fakeer*e0*area./(setxi0+1e-9*servonm);
% cp=pi*r*e0*fakeer*log(2*r*1e9./servonm)+c0'+c1;
% rp=1e9*ones(length(cp),1);

%% Find zero electrode separation using the resistance drop off

if isempty(find((rp>0)&(rp<1e4)))==1
    startingx0=-500;
else
    startingx0=servonm(find(rp==max(rp(find((rp>0)&(rp<1e4))))));
end

%% Plot rp and cp versus x
if seeplot>=3
    figure(1);
    plot(servonm, rp, '.b');
    xlabel('Electrode Position (nm)', 'fontsize', 12);
    ylabel('Resistance (\Omega)', 'fontsize', 12);
    title('Resistance versus Electrode Position', 'fontsize', 12.5);
    legend(['Experimental data from ' substance], 'location', 'southeast');

    figure(11);
    plot(servonm, cp, '.b');
    xlabel('Electrode Position (nm)', 'fontsize', 12);
    ylabel('Capacitance (F)', 'fontsize', 12);
    title('Capacitance versus Electrode Position', 'fontsize', 12.5);
    legend(['Experimental data from ' substance], 'location', 'southeast');
end

%% Set up the limits to search for x0 in NL1 analysis
lowerdatapoint=0;
upperdatapoint=lowerdatapoint+xend;
searchrangelow=5000;
searchrangehigh=0.75*(lowerdatapoint-startingx0);

pointstep=10;
x0array=startingx0-searchrangelow:pointstep:startingx0+searchrangehigh;

%% Generate the transform variable for simple LS and WLS analysis
tempx=servonm(find((servonm>=lowerdatapoint)&(servonm<=upperdatapoint)));
y=cp(find((servonm>=lowerdatapoint)&(servonm<=upperdatapoint)));
gy=1./rp(find((servonm>=lowerdatapoint)&(servonm<=upperdatapoint)));
avgpoints=1;
wy= -pi*e0*r*diff(tempx)./diff(y);
dispx=servonm(find(servonm>(startingx0)));
dispy=cp(find(servonm>(startingx0)));
wdispy= -pi*e0*r*diff(dispx)./diff(dispy);

%% Find epsilon_r and x0 using simple least squares
fitx=tempx(1:length(tempx)-1)+0.5*diff(tempx);
fity=wy;
[fitresult, goodness]=fit(fitx, fity, 'poly1', 'robust', 'on');
simplex0=-fitresult.p2/fitresult.p1;
simpleer=1/fitresult.p1

%% Use x0 as a starting point to make a weighted LS fit
wx0=simplex0;
% Initial WLS fit
for i=1:5
    fitx=tempx(1:length(tempx)-1)+0.5*diff(tempx)-wx0;
    fity=wy;

```

```

deltax=abs(median(diff(servonm)));
sigmac=3e-17;
deltac=pi*r*8.85e-12*log(1+deltax./(fitx));
sigmay=2*sigmac*fity./deltac;
w=1./(sigmay.^2);
if sum(isinf(w))>0
    w(find(isinf(w)==1))=max(w(find(isinf(w)==0)));
end
w(find(w<0))=0;

[fitresult, goodness]=fit(fitx, fity, 'poly1', 'robust', 'off', 'Weights',
w);
wx0=wx0-fitresult.p2/fitresult.p1
end

% Refined WLS fit with better defined xstart and xend
for i=1:5
    tempx3=dispx(1:length(dispx)-1)+0.5*diff(dispx)-wx0;
    tempy3=wdispy;
    fitx=tempx3(find((tempx3>xstart)&(tempx3<xend)));
    fity=tempy3(find((tempx3>xstart)&(tempx3<xend)));

    deltax=abs(median(diff(servonm)));
    sigmac=3e-17;
    deltac=pi*r*8.85e-12*log(1+deltax./(fitx));
    sigmay=2*sigmac*fity./deltac;
    w=1./(sigmay.^2);
    [fitresult, goodness]=fit(fitx, fity, 'poly1', 'robust', 'off', 'Weights',
w);
    wx0=wx0-fitresult.p2/fitresult.p1
end

wer=1/fitresult.p1;
fitline=fitresult.p1*(servonm-wx0)+fitresult.p2;

% Obtain statistical parameters for WLS fit
n=length(w);
wtot=sum(w);
sxx=sum(w.*fitx.^2)/wtot-sum(fitx.*sqrt(w))^2/(n*wtot);
sxy=sum(w.*fitx.*fity)/wtot-sum(fitx.*sqrt(w))*sum(fity.*sqrt(w))/(n*wtot);
syy=sum(w.*fity.^2)/wtot-sum(fity.*sqrt(w))^2/(n*wtot);
sse=syy-sxy^2/sxx;
se=sqrt(sse/(n-2));
wsigab=se/sqrt(sxx);
wsigmaer=wsigab/fitresult.p1^2;
wsigmaa=se*sqrt(1/n);

if seeplot>=1
    % Plot WLS fitting data
    figure(7);
    plot(dispx(1:length(dispx)-1)+0.5*diff(dispx)-wx0, wdispy, '.b', fitx,
fity, '.r', servonm-wx0, fitline, '-k');
    axis([-10 160 -10 160]);
    xlabel('Electrode Position (nm)', 'fontsize', 12);
    ylabel('-\pi\epsilon_0\Delta x/\Delta C (nm)', 'fontsize', 12);
    title(['\epsilon_r of ' substance ' (WLS)'], 'fontsize', 12.5);
    legend(['Exp. data measured at ' num2str(avgfreq, '%1.2e') 'Hz and '
num2str(amp, '%1.0f') 'mV'], 'Data points used for fitting', ['Linear fit
\epsilon_r = ' num2str(wer, '%1.3f') '; \sigma = ' num2str(wsigmaer, '%1.1e')
'];], 'location', 'northwest');
    % Plot Weighted Residue
    figure(8)

```



```

plot(fitx, (fity-fitx*fitresult.p1).*sqrt(w)/sqrt((sum(w))), '.b');
title('Weighted Residue Plot from N_2 Gas Data', 'fontsize', 12.5);
xlabel('Electrode Position (nm)', 'fontsize', 12);
ylabel('Weighted Residue (nm)', 'fontsize', 12);
end

%% NL1 fit - find optimum x0

if nll==1
    % First, a quick search for x0
    fitslope=zeros(length(x0array),1);
    fitse=zeros(length(x0array),1);
    for i=1:length(x0array)
        x0=x0array(i);
        x=tempx-x0;
        %Technique 1 - use consecutive values of C(x)
        fitx=pi*r*e0*log(1+diff(x)./(x(1:length(x))-1));
        fity=-diff(y);

        %
        %Technique 2
        % fitx=zeros(length(x)-1,1);
        % fity=zeros(length(x)-1,1);
        % %midx=round(length(x)/2);
        % midx=length(x);
        % for i2=1:length(x)-1
        %     %fitx(i2)=-pi*r*e0*log(1+(x(i2)-x(midx))/(x(midx)-x0));
        %     fitx(i2)=pi*r*e0*log(1+(x(midx)-x(i2))/(x(i2)-x0));
        %     fity(i2)=y(i2)-y(midx);
        % end

        [fitresult, goodness]=fit(fitx, fity, 'poly1', 'robust', 'off');
        fitse(i)=goodness.rmse;
        fitslope(i)=fitresult.p1;
    end
    if seeplot>=5
        figure(2);
        plot(x0array, fitse, '.');
    end

    % Second, a more refined search for x0
    x0=x0array(find(fitse==min(fitse)));
    searchrange=14;
    pointstep=0.25;
    x0array=x0-searchrange:pointstep:x0+searchrange;
    fitslope=zeros(length(x0array),1);
    fitse=zeros(length(x0array),1);
    for i=1:length(x0array)
        x0=x0array(i);
        x=tempx-x0;
        %Technique 1
        fitx=pi*r*e0*log(1+diff(x)./(x(1:length(x))-1));
        fity=-diff(y);

        %
        %Technique 2
        % fitx=zeros(length(x)-1,1);
        % fity=zeros(length(x)-1,1);
        % %midx=round(length(x)/2);
        % midx=length(x);
        % for i2=1:length(x)-1
        %     fitx(i2)=pi*r*e0*log(1+(x(midx)-x(i2))/(x(i2)-x0));
        %     fity(i2)=y(i2)-y(midx);
        % end
    end
end

```

```

        [fitresult, goodness]=fit(fitx, fity, 'poly1', 'robust', 'off');
        fitse(i)=goodness.rmse;
        fitslope(i)=fitresult.p1;
    end

    if seeplot>=5
        figure(3);
        plot(x0array, fitse, '.');
    %    figure(4);
    %    plot(x0array, fitslope, '.');
    end

    % Finally, use the optimum x0 to fit to determine epsilon_r
    x0=x0array(find(fitse==min(fitse)));
    if (find(fitse==min(fitse))==1) || (find(fitse==min(fitse))==length(fitse))
        filebad=1;
    end
    %x0=-2832+0.7*abs(median(diff(servonm)));
    x=tempx-x0;

    %Technique 1
    fitx=pi*r*e0*log(1+diff(x)/(x(1:length(x)-1)));
    fity=-diff(y);
    dispfitx=pi*r*e0*log(1+diff(dispx)/(dispx(1:length(dispx)-1)-x0));
    dispfity=-diff(dispy);

    % %Technique 2
    % fitx=zeros(length(x)-1,1);
    % fity=zeros(length(x)-1,1);
    % %midx=round(length(x)/2);
    % midx=length(x);
    % for i2=1:length(x)-1
    %     %fitx(i2)=-pi*r*e0*log(1+(x(i2+1)-x(midx))/(x(midx)-x0));
    %     fitx(i2)=pi*r*e0*log(1+(x(midx)-x(i2))/(x(i2)-x0));
    %     fity(i2)=y(i2)-y(midx);
    % end
    % dispfitx=zeros(length(dispx)-1,1);
    % dispfity=zeros(length(dispx)-1,1);
    % for i2=1:length(dispx)-1
    %     dispfitx(i2)=pi*r*e0*log(1+(x(midx)-(dispx(i2)-x0))/(dispx(i2)-
2*x0));
    %     dispfity(i2)=dispy(i2)-y(midx);
    % end

    [fitresult, goodness]=fit(fitx, fity, 'poly1', 'robust', 'off');
    er=fitresult.p1;
    comper=wer/1.01;

    sxx=sum(fitx.^2)-(sum(fitx)^2)/length(fitx);
    erstd=goodness.rmse/sqrt(sxx);
    if seeplot>=1
        figure(5);
        fitline=fitx*fitresult.p1+fitresult.p2;
        plot(dispfitx, dispfity, '.b', fitx, fity, '.r', fitx, fitline, '-k');
        axis([min(fitx)-0.2*max(fitx) 1.2*max(fitx) min(fity)-0.2*max(fity)
1.2*max(fity)])
        xlabel(['-\pi r \epsilon_0 \ln(1+(x_m-x_n)/(x_n-x_0)) (F)', 'fontsize',
12);
        ylabel(['C_n - C_m (F)', 'fontsize', 12);
        title(['\epsilon_r of ' substance ' (NL1)'], 'fontsize', 12.5);

```

```

    w=1./(sigmay.^2);
    [fitresult, goodness]=fit(fitx, fity, 'poly1', 'robust', 'off', 'Weights',
w);
    wkx0=wkx0-fitresult.p2/fitresult.p1;
end

wk=1/fitresult.p1;
fitline=fitresult.p1*(servonm-wkx0);

n=length(w);
wtot=sum(w);
sxx=sum(w.*fitx.^2)/wtot-sum(fitx.*sqrt(w))^2/(n*wtot);
sxy=sum(w.*fitx.*fity)/wtot-sum(fitx.*sqrt(w))*sum(fity.*sqrt(w))/(n*wtot);
syy=sum(w.*fity.^2)/wtot-sum(fity.*sqrt(w))^2/(n*wtot);
sse=syy-sxy^2/sxx;
se=sqrt(sse/(n-2));
wsigmab=se/sqrt(sxx);
wkstd=wsigmab/fitresult.p1^2;
wsigmaa=se*sqrt(1/n);

if seeplot>=1
    % Plot WLS fit for conductivity
    figure(17);
    plot(dispgx(1:length(dispgx)-1)+0.5*diff(dispgx)-wkx0, dispwgy, '.b', fitx,
fity, '.r', servonm-wkx0, fitline, '-k')
    xlabel('Electrode Displacement (nm)', 'fontsize', 12);
    ylabel('-\pir\Delta x/\Delta G (nm)', 'fontsize', 12)
    title(['Conductivity of ' substance ' (WLS)'], 'fontsize', 12.5);
    legend(['Exp. data measured at ' num2str(avgttemp1, '%1.1f') '\circC and '
num2str(avgfreq, '%1.2e') 'Hz'], 'Data Points Used in WLS Fit', ['Linear fit
\kappa=' num2str(wk, '%1.2e') 'S/m; \sigma=' num2str(wkstd, '%1.1e') 'S/m;
x_0=' num2str(wkx0, '%3.1f') 'nm'], 'location', 'northwest');
    % Plot weighted residue
    figure(18)
    plot(fitx, (fity-fitx*fitresult.p1).*sqrt(w)/sqrt((sum(w))), '.b');
    title('Weighted Residue Plot');
    xlabel('Electrode Position Measured by Servo Encoder (nm)');
    ylabel('Weighted Residue (nm)');
end

%% Determine conductivity using NLI fit method
if nllg==1
    fitslope=zeros(length(x0array),1);
    fitse=zeros(length(x0array),1);

    % First, a quick search for x0
    for i=1:length(x0array)
        kx0=x0array(i);
        x=tempx-kx0;
        %Technique 1
        fitx=-pi*r*log(1+diff(x)./(x(1:length(x)-1)));
        fity=diff(gy);

        %
        %Technique 2
        %
        fitx=zeros(length(x)-1,1);
        %
        fity=zeros(length(x)-1,1);
        %
        %midx=round(length(x)/2);
        %
        midx=length(x);
        %
        for i2=1:length(x)-1
            %
            %fitx(i2)=-pi*r*e0*log(1+(x(i2)-x(midx))/(x(midx)-kx0));
            %
            fitx(i2)=pi*r*log(1+(x(midx)-x(i2))/(x(i2)-kx0));
            %
            fity(i2)=gy(i2)-gy(midx);
            %
        end
    end
end

```

```

        [fitresult, goodness]=fit(fitx, fity, 'poly1', 'robust', 'off');
        fitse(i)=goodness.rmse;
        fitslope(i)=fitresult.p1;
end
if seeplot>=5
    figure(12);
    plot(x0array, fitse, '.');
end

% Second, a more refined search for x0
kx0=x0array(find(fitse==min(fitse)));
searchrange=25;
pointstep=1;
x0array=kx0-searchrange:pointstep:kx0+searchrange;
fitslope=zeros(length(x0array),1);
fitse=zeros(length(x0array),1);
for i=1:length(x0array)
    kx0=x0array(i);
    x=tempx-kx0;
    %Technique 1
    fitx=-pi*r*log(1+diff(x)./(x(1:length(x)-1)));
    fity=diff(gy);

    % %Technique 2
    % fitx=zeros(length(x)-1,1);
    % fity=zeros(length(x)-1,1);
    % %midx=round(length(x)/2);
    % midx=length(x);
    % for i2=1:length(x)-1
    %     fitx(i2)=pi*r*log(1+(x(midx)-x(i2))/(x(i2)-kx0));
    %     fity(i2)=gy(i2)-gy(midx);
    % end

    [fitresult, goodness]=fit(fitx, fity, 'poly1', 'robust', 'off');
    fitse(i)=goodness.rmse;
    fitslope(i)=fitresult.p1;
end

if seeplot>=5
    figure(13);
    plot(x0array, fitse, '.');
end

% Use the optimum kx0 to fit for the conductivity k
kx0=x0array(find(fitse==min(fitse)));
if (find(fitse==min(fitse))==1) || (find(fitse==min(fitse))==length(fitse))
    filebad=filebad+2;
end
%kx0=-2832+0.7*abs(median(diff(servonm)));
x=tempx-kx0;
%Technique 1
fitx=-pi*r*log(1+diff(x)./(x(1:length(x)-1)));
fity=diff(gy);

% %Technique 2
% fitx=zeros(length(x)-1,1);
% fity=zeros(length(x)-1,1);
% %midx=round(length(x)/2);
% midx=length(x);
% for i2=1:length(x)-1
%     %fitx(i2)=-pi*r*e0*log(1+(x(i2+1)-x(midx))/(x(midx)-kx0));
%     fitx(i2)=pi*r*log(1+(x(midx)-x(i2))/(x(i2)-kx0));

```

```

        [fitresult, goodness]=fit(fitx, fity, 'poly1', 'robust', 'off');
        fitse(i)=goodness.rmse;
        fitslope(i)=fitresult.p1;
    end
    if seeplot>=5
        figure(12);
        plot(x0array, fitse, '.');
    end

    % Second, a more refined search for x0
    kx0=x0array(find(fitse==min(fitse)));
    searchrange=25;
    pointstep=1;
    x0array=kx0-searchrange:pointstep:kx0+searchrange;
    fitslope=zeros(length(x0array),1);
    fitse=zeros(length(x0array),1);
    for i=1:length(x0array)
        kx0=x0array(i);
        x=tempx-kx0;
        %Technique 1
        fitx=-pi*r*log(1+diff(x)./(x(1:length(x)-1)));
        fity=diff(gy);

        % %Technique 2
        % fitx=zeros(length(x)-1,1);
        % fity=zeros(length(x)-1,1);
        % %midx=round(length(x)/2);
        % midx=length(x);
        % for i2=1:length(x)-1
        %     fitx(i2)=pi*r*log(1+(x(midx)-x(i2))/(x(i2)-kx0));
        %     fity(i2)=gy(i2)-gy(midx);
        % end

        [fitresult, goodness]=fit(fitx, fity, 'poly1', 'robust', 'off');
        fitse(i)=goodness.rmse;
        fitslope(i)=fitresult.p1;
    end

    if seeplot>=5
        figure(13);
        plot(x0array, fitse, '.');
    end

    % Use the optimum kx0 to fit for the conductivity k
    kx0=x0array(find(fitse==min(fitse)));
    if (find(fitse==min(fitse))==1) || (find(fitse==min(fitse))==length(fitse))
        filebad=filebad+2;
    end
    %kx0=-2832+0.7*abs(median(diff(servonm)));
    x=tempx-kx0;
    %Technique 1
    fitx=-pi*r*log(1+diff(x)./(x(1:length(x)-1)));
    fity=diff(gy);

    % %Technique 2
    % fitx=zeros(length(x)-1,1);
    % fity=zeros(length(x)-1,1);
    % %midx=round(length(x)/2);
    % midx=length(x);
    % for i2=1:length(x)-1
    %     %fitx(i2)=-pi*r*e0*log(1+(x(i2+1)-x(midx))/(x(midx)-kx0));
    %     fitx(i2)=pi*r*log(1+(x(midx)-x(i2))/(x(i2)-kx0));

```

```

    %     fity(i2)=gy(i2)-gy(midx);
    % end
    % dispfitgx=zeros(length(dispgx)-1,1);
    % dispfitgy=zeros(length(dispgx)-1,1);
    % for i2=1:length(dispfitgx)-1
    %     dispfitgx(i2)=pi*r*log(1+(x(midx)-(dispgx(i2)-kx0))/(dispgx(i2)-
2*kx0));
    %     dispfitgy(i2)=dispgy(i2)-gy(midx);
    % end

    [fitresult, goodness]=fit(fitx, fity, 'poly1', 'robust', 'off');
    k=fitresult.p1;
    sxx=sum(fitx.^2)-(sum(fitx)^2)/length(fitx);
    kstd=goodness.rmse/sqrt(sxx);
    if seeplot>=1
        figure(15);
        fitline=fitx*fitresult.p1+fitresult.p2;
        plot(fitx, fity, 'r', fitx, fitline, '-k');
        axis([min(fitx)-0.2*max(fitx) 1.2*max(fitx) min(fity)-0.2*max(fity)
1.2*max(fity)])
        xlabel('\pirln(1+(x_m-x_n)/(x_n-x_0)) (F)', 'fontsize', 12);
        ylabel('G_n - G_m (F)', 'fontsize', 12);
        title(['Conductivity of ' substance ' (NL1)'], 'fontsize', 12.5);
        legend('Experimental Data', ['\kappa = ' num2str(k, '%1.3e') '; \sigma
= ' num2str(kstd, '%1.1e') '; x_0 = ' num2str(kx0, '%1.1f') 'nm'], 'location',
'northwest');
    end
end

% Optional command output
% ['Dielectric Constant: er=' num2str(er, '%1.3f') ' wer=' num2str(wer,
'%1.3f')]
% ['Conductivity k=' num2str(k, '%1.3e') ' wk=' num2str(wk, '%1.3e')]
% ['x0=' num2str(x0, '%1.1f') ' kx0=' num2str(kx0, '%1.1f') ' diff='
num2str(x0-kx0, '%1.1f')]
% ['wx0=' num2str(wx0, '%1.1f') ' wkx0=' num2str(wkx0, '%1.1f') ' diff='
num2str(wx0-wkx0, '%1.1f')]
% ['Filebad=' num2str(filebad, '%1.0f') ' temp=' num2str(avgtemp1, '%1.1f') 'C
freq=' num2str(avgfreq)]

```

Surface Roughness Model

```

%% Surface Roughness Calculation
p1=19; p2=25;
x=dispX(1:length(dispX)-1)+0.5*diff(dispX)-wx0;
y=smooth(wdispy, 5);
roughy=1./((2/(p1+p2))*((x/p1-1).*log(1-p1./x)+(x/p2+1).*log(1+p2./x)));
% roughy=1./((2/(p1+p2))*((y/p1-1).*log(1-p1./y)+(y/p2+1).*log(1+p2./y)));
figure(12);
plot(x, y, 'b', x, roughy, '-r', servonm-wx0, fitline, '-k', 'linewidth', 1.5,
'markersize', 12);
axis([-10 70 -10 70]);
xlabel('Electrode Position (nm)', 'fontsize', 12);
ylabel('y = -\pir\epsilon_0\Delta x/\Delta C (nm)', 'fontsize', 12)
title(['Small Electrode Gaps in ' substance], 'fontsize', 12.5);
legend('Experimental Data', ['Roughness Model: p1=' num2str(p1) 'nm p2='
num2str(p2) 'nm'], ['Linear fit \epsilon_r = ' num2str(wer, '%1.3f') '; \sigma
= ' num2str(wsigmaer, '%1.1e') ';'], 'location', 'northwest');

```

Appendix C: Visual Basic Code

See Figure 2.15 on page 54 for a screen shot of the graphical user interface.

```
Imports System
Imports System.IO
Imports System.Math
Imports NationalInstruments
Imports NationalInstruments.DAQmx
Imports Ivi
Imports Ivi.Visa.Interop

Public Class HongDaq

    Const mincap = 10000000000.0
    Dim voltzero As Double
    Dim picoposition As Double
    Dim digitalwritedef As Task
    Dim analogreaddef As Task
    Dim analogreaddef1 As Task
    Dim analogreaddef3 As Task
    Dim analogreaddef4 As Task
    Dim analogreaddef5 As Task
    Dim digitalwriter As DigitalSingleChannelWriter
    Dim analogreader As AnalogSingleChannelReader
    Dim capreader1 As AnalogSingleChannelReader
    Dim capreader3 As AnalogSingleChannelReader
    Dim capreader4 As AnalogSingleChannelReader
    Dim capreader5 As AnalogSingleChannelReader
    Dim ioDMM As Ivi.Visa.Interop.FormattedIO488
    Dim ioDMM2 As Ivi.Visa.Interop.FormattedIO488
    Dim ioLCR As Ivi.Visa.Interop.FormattedIO488
    Dim ioPPS As Ivi.Visa.Interop.FormattedIO488
    Dim VISAmgr As Ivi.Visa.Interop.ResourceManager
    Dim GPIBenabled As Boolean = True
    Dim recording As Boolean = False
    Dim logfile As System.IO.File
    Dim starttime As Date
    Dim picoactiveflag As Boolean = False
    Dim freqpointstaken As Integer = 0
    Dim freqstr As String
    Dim ampstr As String
    Dim biasstr As String
    Dim spectrumactive As Boolean = False
    Dim scriptstr As String

    Dim datapointscollected As Integer = 0
    Dim getspectraset As Boolean = False
    Dim desiredposition As Single
    Dim servocmdsent As Boolean

    Dim samplestate As Integer = 0 'state variable 0=normal run mode, 1=send
new servo position, 2=wait for new position to be reached
```

```

'3=Wait for position to settle, 4=get new Cp and Rp data, 5=wait after data
collection
Dim settletime As Integer = 0 'settling timer after new position has been
reached
Dim aftertime As Integer = 0 'timer for after data collection

Dim repeatgetstate As Integer '0=no repeat get, 1=retraction, 2=go to
start, 3=get data 'till end
Dim freqgetstate As Integer '0=no freq get, 1=retraction and set frequency,
2=go to start, 3=get data 'till end
Dim ampgetstate As Integer '0=no amp get, 1=retraction and set frequency,
2=go to start, 3=get data 'till end
Dim biasgetstate As Integer '0=no bias get, 1=retraction and set frequency,
2=go to start, 3=get data 'till end

'#####
Private Sub Form1_Load(ByVal sender As System.Object, ByVal e As
System.EventArgs) Handles MyBase.Load
    System.Windows.Forms.Form.CheckForIllegalCrossThreadCalls = False

    txtmv.Text = "500"
    txtFreq.Text = "120000"
    txtFreqFilename.Text = "c:\data\bob\freq2.txt"
    txtPointsPerFreq.Text = "1"
    down.Checked = True
    txtPicoPosition.Text = "0"
    txtPicoDelta.Text = "0"

    txtLogfilename.Text = "c:\data\ss\log1"
    chkRecordwhilemoving.Checked = False
    btnSkiptoNext.Enabled = False
    txtScriptFilename.Text = "c:\data\bob7\script1.txt"

    'serial port for Newport actuator
    If SerialPort3.IsOpen Then
        SerialPort3.Close()
    End If
    SerialPort3.PortName = "COM1"
    SerialPort3.BaudRate = 57600
    SerialPort3.ReceivedBytesThreshold = 12
    SerialPort3.DataBits = 8
    SerialPort3.StopBits = Ports.StopBits.One
    SerialPort3.Parity = Ports.Parity.None
    SerialPort3.Handshake = Ports.Handshake.XOnXOff
    Try
        SerialPort3.Open()
    Catch ex As Exception
        MsgBox(ex.Message)
    End Try

    digitalwritedef = New Task()
    Try
        ' Create an Digital Output channel and name it.
        digitalwritedef.DOChannels.CreateChannel("Dev1/port0", "port0", _
ChannelLineGrouping.OneChannelForAllLines)

        ' Write digital port data. WriteDigitalSingChanSingSampPort writes
a single sample
        ' of digital data on demand, so no timeout is necessary.
        digitalwriter = New
DigitalSingleChannelWriter(digitalwritedef.Stream)
    Catch ex As System.Exception
        MessageBox.Show(ex.Message)
    End Try

```



```

Finally
    System.Windows.Forms.Cursor.Current = Cursors.Default
    'digitalwritedef.Dispose()
End Try

analogreaddef = New Task()
analogreaddef1 = New Task()
analogreaddef3 = New Task()
analogreaddef4 = New Task()
analogreaddef5 = New Task()

Try
    ' Create an analog input channel and name it.
    analogreaddef.AIChannels.CreateVoltageChannel("dev1/ai6", "ai6", _
        AITerminalConfiguration.Differential, -10, 10,
AIVoltageUnits.Volts)
    analogreader = New AnalogSingleChannelReader(analogreaddef.Stream)

    Dim rt As Double
    Dim tempraw As Double
    digitalwriter.WriteSingleSamplePort(True, 0)
    tempraw = analogreader.ReadSingleSample()
    rt = (-7584.8 * tempraw - 125571.9528) / (1.8962 * tempraw -
25.846)
    txtTemp1.Text = Format$(1 / (0.00113 + 0.0002339 * Log(rt) +
0.00000008863 * (Log(rt)) ^ 3) - 273.15, "##.0")
    txtTemp1.Text = Format$(1 / (0.00113 + 0.0002339 * Log(rt) +
0.00000008863 * (Log(rt)) ^ 3) - 273.15, "##.0")

    digitalwriter.WriteSingleSamplePort(True, 2)
    tempraw = analogreader.ReadSingleSample()
    rt = (-7584.8 * tempraw - 125571.9528) / (1.8962 * tempraw -
25.846)
    txtTemp2.Text = Format$(1 / (0.00113 + 0.0002339 * Log(rt) +
0.00000008863 * (Log(rt)) ^ 3) - 273.15, "##.0")

    digitalwriter.WriteSingleSamplePort(True, 4)
    tempraw = analogreader.ReadSingleSample()
    rt = (-7584.8 * tempraw - 125571.9528) / (1.8962 * tempraw -
25.846)
    txtTemp3.Text = Format$(1 / (0.00113 + 0.0002339 * Log(rt) +
0.00000008863 * (Log(rt)) ^ 3) - 273.15, "##.0")

    digitalwriter.WriteSingleSamplePort(True, 6)
    tempraw = analogreader.ReadSingleSample()
    rt = (-7584.8 * tempraw - 125571.9528) / (1.8962 * tempraw -
25.846)
    txtTemp4.Text = Format$(1 / (0.00113 + 0.0002339 * Log(rt) +
0.00000008863 * (Log(rt)) ^ 3) - 273.15, "##.0")
    Catch ex As System.Exception
        MessageBox.Show(ex.Message)
    End Try

If chkGPiBenable.Checked Then
    ini_GPIB()
End If

My.Computer.Audio.Play("c:\WINDOWS\Media\notify.wav")

Timer1.Interval = 200
Timer1.Enabled = True

```

```

        Timer2.Interval = 5000
        Timer2.Enabled = True

        grpPico.Enabled = False
    End Sub

'#####
Private Sub ini_GPIB()
    VISAmgr = New Ivi.Visa.Interop.ResourceManager()
    ioDMM = New Ivi.Visa.Interop.FormattedIO488()
    ioDMM2 = New Ivi.Visa.Interop.FormattedIO488()
    ioLCR = New Ivi.Visa.Interop.FormattedIO488()
    ioPPS = New Ivi.Visa.Interop.FormattedIO488()
    Try
        ioDMM.IO() = VISAmgr.Open("TCPIP0::10.0.0.3::gpib0,22::INSTR",
        AccessMode.NO_LOCK)
        ioDMM2.IO() = VISAmgr.Open("TCPIP0::10.0.0.3::gpib0,20::INSTR",
        AccessMode.NO_LOCK)
        ioPPS.IO() = VISAmgr.Open("TCPIP0::10.0.0.3::gpib0,5::INSTR",
        AccessMode.NO_LOCK)
        ioLCR.IO() = VISAmgr.Open("TCPIP0::10.0.0.3::gpib0,17::INSTR",
        AccessMode.NO_LOCK)
        ioLCR.SetBufferSize(BufferMask.IO_IN_BUF, 30)
        ini_LCR()
    Catch ex As Exception
        MessageBox.Show(ex.Message)
    End Try
    GPIBEnabled = True
End Sub

'#####
Private Sub ini_LCR()
    ioLCR.WriteString("INIT:CONT ON" & Chr(10))
    ioLCR.WriteString("APER MED" & Chr(10))
    ioLCR.WriteString("BIAS STATE OFF" & Chr(10))
    ioLCR.WriteString("FREQ " & txtFreq.Text & "Hz" & Chr(10))
    ioLCR.WriteString("VOLT " & txtmv.Text & "mV" & Chr(10))
End Sub

'#####
Private Function getdata() As Boolean
    Dim tempstr As String = ""
    Try
        'SerialPort2.Write("*")

        ioLCR.WriteString("FETC?" & Chr(10))
        tempstr = ioLCR.ReadString()
        txtCp.Text = Format(Convert.ToDouble(Mid(tempstr, 1, InStr(tempstr,
        ",") - 1)), "E")
        tempstr = Mid(tempstr, InStr(tempstr, ",") + 1, tempstr.Length -
        InStr(tempstr, ","))
        txtRp.Text = Format(Convert.ToDouble(Mid(tempstr, 1, InStr(tempstr,
        ",") - 1)), "E")

        ioDMM.WriteString("READ?" & Chr(10))
        txtCapV.Text = Format(Convert.ToDouble(ioDMM.ReadString()),
        "##.0000")
        txtCapnm.Text = Format((Convert.ToDouble(txtCapV.Text) - voltzero)
        / 0.0004, "#.00")

        ioDMM2.WriteString("READ?" & Chr(10))
        txtbtmv.Text = Format(Convert.ToDouble(ioDMM2.ReadString()),
        "##.0000")
    End Try
End Function

```

```

        txtbtmm.Text = Format((Convert.ToDouble(txtbtmv.Text) - voltzero)
/ 0.0004, "#.00")

        Return True
    Catch ex As Exception
        'MessageBox.Show("GPIB Error: " + ex.Message)
        'the exception message should be written somewhere
        Return False
    End Try
End Function

'#####
Private Sub HongDaq_FormClosing(ByVal sender As System.Object, ByVal e As
System.Windows.Forms.FormClosingEventArgs) Handles MyBase.FormClosing
    If SerialPort2.IsOpen Then
        SerialPort2.Close()
    End If
    If SerialPort3.IsOpen Then
        SerialPort3.Close()
    End If
End Sub

'#####
Private Sub txtLogfilename_TextChanged(ByVal sender As System.Object, ByVal e
As System.EventArgs) Handles txtLogfilename.TextChanged
    Dim filenumber As Integer = 0
    Dim fullfilename As String

    Do
        filenumber = filenumber + 1
        txtLogfileExt.Text = Format$(filenumber, "000")
        fullfilename = txtLogfilename.Text & "." & txtLogfileExt.Text
    Loop While My.Computer.FileSystem.FileExists(fullfilename) = True

End Sub

'#####
Private Sub Timer1_Tick(ByVal sender As System.Object, ByVal e As
System.EventArgs) Handles Timer1.Tick
    SerialPort3.Write("1TP" + Chr(13) + Chr(10))
    If samplestate = 0 Then 'State = normal run mode
        If GPIBenabled Then
            If getdata() = True Then
                If recording Then
                    My.Computer.FileSystem.WriteAllText(txtLogfilename.Text
& "." & txtLogfileExt.Text, _
                    Format((Now() - starttime).TotalSeconds, "#.000") + ","
+ txtFreq.Text + "," + _
                    txtCp.Text + "," + txtRp.Text + "," + txtCapnm.Text +
                    "," + txtCapV.Text + "," + _
                    txtServoPos.Text + "," + txtbtmv.Text + "," +
                    txtbtmm.Text + "," + _
                    txtbiasmv.Text + "," + txtTemp1.Text + "," +
                    txtTemp2.Text + "," + _
                    txtTemp3.Text + "," + txtTemp4.Text + "," + txtmv.Text
                    + Chr(10), True)
                End If
            End If
            getdata()
        End If
    ElseIf samplestate = 1 Then 'State = Send new servo position
        If Abs(Val(txtServoPos.Text) - Val(txtGoServoPos.Text)) <=
Val(txtIncrementalAmount.Text) Then

```

```

        desiredposition = Val(txtGoServoPos.Text)
        onestep(desiredposition)
    Else
        desiredposition = Sign(Val(txtGoServoPos.Text) -
Val(txtServoPos.Text)) * Val(txtIncrementalAmount.Text) + Val(txtServoPos.Text)
        onestep(desiredposition)
    End If
    samplestate = 2
    ElseIf samplestate = 2 Then 'State = Wait for new position to be
reached
        If ((Abs(desiredposition - Val(txtServoPos.Text)) < 0.00001) Or
(Val(txtCp.Text) > mincap)) Then
            samplestate = 3
            settletime = Val(txtWaitTime.Text)
        End If
        ElseIf samplestate = 3 Then 'State = wait for new position to settle
            settletime = settletime - 1
            If settletime = 0 Then
                samplestate = 4
            End If

        ElseIf samplestate = 4 Then 'State = get new data
            If recording Then
                If getdata() = True Then
                    My.Computer.FileSystem.WriteAllText(txtLogfilename.Text &
"." & txtLogfileExt.Text, _
                        Format((Now() - starttime).TotalSeconds, "#.000") + ","
+ txtFreq.Text + "," + _
                        txtCp.Text + "," + txtRp.Text + "," + txtCapnm.Text +
                        "," + txtCapV.Text + "," + _
                        txtServoPos.Text + "," + txtbtmv.Text + "," +
txtbtmmn.Text + "," + _
                        txtbiasmv.Text + "," + txtTemp1.Text + "," +
txtTemp2.Text + "," + _
                        txtTemp3.Text + "," + txtTemp4.Text + "," + txtmv.Text
+ Chr(10), True)
                End If
            End If
            aftertime = Val(txtwaittime2.Text)
            samplestate = 5

        ElseIf samplestate = 5 Then 'State = wait after data collection
            aftertime = aftertime - 1
            If aftertime = 0 Then
                If ((Abs(Val(txtServoPos.Text) - Val(txtGoServoPos.Text)) <=
0.00001) Or (Val(txtCp.Text) > mincap)) Then
                    samplestate = 0
                Else
                    samplestate = 1
                End If
            End If
        End If
    End Sub

'#####
Private Sub btnZero_Click(ByVal sender As System.Object, ByVal e As
System.EventArgs) Handles btnZero.Click
    'ioDMM.WriteString("READ?" & Chr(10))
    'voltzero = Convert.ToDouble(ioDMM.ReadString())
    'picoposition = 0
End Sub

'#####

```

```

Private Sub btnRecord_Click(ByVal sender As System.Object, ByVal e As
System.EventArgs) Handles btnRecord.Click
    If btnRecord.Text = "Record to Log File" Then
        txtLogfilename_TextChanged(sender, e)
        txtLogfilename.Enabled = False
        recording = True
        btnRecord.Text = "Stop Recording"
        My.Computer.FileSystem.WriteAllText(txtLogfilename.Text & "." &
txtLogfileExt.Text, _
        "//Time, Freq, Cp, Rp, Capnm, CapV, Servomm, btmV, btmm, Bias-
mV, Temp1, Temp2, Temp3, Temp4, Notes, Log file started at " _
        & Now.ToString & Chr(10), True)
        starttime = Now()
    ElseIf btnRecord.Text = "Stop Recording" Then
        recording = False
        My.Computer.FileSystem.WriteAllText(txtLogfilename.Text & "." &
txtLogfileExt.Text, _
        "//Log file ended at " & Now.ToString & Chr(10), True)
        txtLogfilename.Enabled = True
        btnRecord.Text = "Record to Log File"
        spectrumactive = False
        btnGetSpectrum.Enabled = True
        btnSetFreq.Enabled = True
    End If
End Sub

'#####
Private Sub chkGPIBenable_Click(ByVal sender As System.Object, ByVal e As
System.EventArgs) Handles chkGPIBenable.Click
    If chkGPIBenable.Checked Then
        ini_GPIB()
    Else
        GPIBenabled = False
    End If
End Sub

'#####
Private Sub btnSetFreq_Click(ByVal sender As System.Object, ByVal e As
System.EventArgs) Handles btnSetFreq.Click
    Dim freq As Integer = Val(txtFreq.Text)
    If GPIBenabled Then
        If freq < 20 Then
            freq = 20
        End If
        If freq > 800000 Then
            freq = 800000
        End If
        If 5000000.0 / freq > 1000 Then
            Timer1.Interval = 500000.0 / freq
        Else
            Timer1.Interval = 1000
        End If
        ioLCR.WriteString("FREQ " + txtFreq.Text + "Hz" + Chr(10))
    End If
End Sub

'#####
Private Sub btnGoPico_Click(ByVal sender As System.Object, ByVal e As
System.EventArgs) Handles btnGoPico.Click
    If down.Checked Then
        'Call runpicocmd("r", Val(txtPicoDelta.Text))
    Else
        'Call runpicocmd("l", Val(txtPicoDelta.Text))
    End If
End Sub

```

```

        End If
        txtPicoDelta.Enabled = False
End Sub

'#####
Private Sub SerialPort3_DataReceived(ByVal sender As System.Object, ByVal e As
System.IO.Ports.SerialDataReceivedEventArgs) Handles SerialPort3.DataReceived
    Dim buf As String
    buf = SerialPort3.ReadExisting()
    If Mid(buf, 1, 3) = "1TP" Then
        txtServoPos.Text = Mid(buf, 4, InStr(buf, Chr(13)) - 4)
    End If
End Sub

'#####
Private Sub btn50000_Click(ByVal sender As System.Object, ByVal e As
System.EventArgs) Handles btn50000.Click
    txtPicoDelta.Text = 50000
    btnGoPico_Click(sender, e)
End Sub

'#####
Private Sub btn10000_Click(ByVal sender As System.Object, ByVal e As
System.EventArgs) Handles btn10000.Click
    txtPicoDelta.Text = 10000
    btnGoPico_Click(sender, e)
End Sub

'#####
Private Sub btn5000_Click(ByVal sender As System.Object, ByVal e As
System.EventArgs) Handles btn5000.Click
    txtPicoDelta.Text = 5000
    btnGoPico_Click(sender, e)
End Sub

'#####
Private Sub btn1000_Click(ByVal sender As System.Object, ByVal e As
System.EventArgs) Handles btn1000.Click
    txtPicoDelta.Text = 1000
    btnGoPico_Click(sender, e)
End Sub

'#####
Private Sub btn500_Click(ByVal sender As System.Object, ByVal e As
System.EventArgs) Handles btn500.Click
    txtPicoDelta.Text = 500
    btnGoPico_Click(sender, e)
End Sub

'#####
Private Sub btn100_Click(ByVal sender As System.Object, ByVal e As
System.EventArgs) Handles btn100.Click
    txtPicoDelta.Text = 100
    btnGoPico_Click(sender, e)
End Sub

'#####
Private Sub btn10_Click(ByVal sender As System.Object, ByVal e As
System.EventArgs) Handles btn10.Click
    txtPicoDelta.Text = 10
    btnGoPico_Click(sender, e)
End Sub

```

```

#####
Private Sub btnGetSpectrum_Click(ByVal sender As System.Object, ByVal e As
System.EventArgs) Handles btnGetSpectrum.Click
    If btnRecord.Text = "Record to Log File" Then
        'btnRecord_Click(sender, e)
    ElseIf btnRecord.Text = "Stop Recording" Then
        'do nothing
        'btnRecord_Click(sender, e)
        'btnRecord_Click(sender, e)
    End If
    Try
        freqstr = My.Computer.FileSystem.ReadAllText(txtFreqFilename.Text)
        spectrumactive = True
        btnGetSpectrum.Enabled = False
        btnSetFreq.Enabled = False
    Catch ex As Exception
        MessageBox.Show(ex.Message)
        spectrumactive = False
        btnGetSpectrum.Enabled = True
        btnSetFreq.Enabled = True
    End Try
End Sub

#####
Private Sub btnExecuteScript_Click(ByVal sender As System.Object, ByVal e As
System.EventArgs) Handles btnExecuteScript.Click
    If btnExecuteScript.Text = "Execute Script" Then
        Try
            scriptstr =
My.Computer.FileSystem.ReadAllText(txtScriptFilename.Text)
            btnExecuteScript.Text = "Stop Script"
            btnSkiptoNext.Enabled = True
            If btnRecord.Text = "Record to Log File" Then
                btnRecord_Click(sender, e)
            End If
        Catch ex As Exception
            MessageBox.Show(ex.Message)
            btnExecuteScript.Text = "Execute Script"
            btnSkiptoNext.Enabled = False
        End Try
    Else
        scriptstr = ""
        btnExecuteScript.Text = "Execute Script"
        txtScriptCurrent.Text = "Script Stopped"
        txtScriptNext.Text = ""
    End If
End Sub

#####
Private Sub btnSkiptoNext_Click(ByVal sender As System.Object, ByVal e As
System.EventArgs) Handles btnSkiptoNext.Click
    If Not txtScriptNext.Text = "" Then
        scriptstr = Mid(scriptstr, InStr(1, scriptstr, Chr(13)) + 2,
Len(scriptstr))
    End If
End Sub

#####
Private Sub btnGoServo_Click(ByVal sender As System.Object, ByVal e As
System.EventArgs) Handles btnGoServo.Click
    If (Val(txtGoServoPos.Text) < 26 And Val(txtGoServoPos.Text) > 0) Then
        SerialPort3.Write("1PA" + txtGoServoPos.Text + Chr(13) + Chr(10))
    End If

```

```

End Sub

'#####
Private Sub btnServo10_Click(ByVal sender As System.Object, ByVal e As
System.EventArgs) Handles btnServo10.Click
    If optServoDown.Checked = True Then
        txtGoServoPos.Text = Format(Val(txtServoPos.Text) + 0.00001,
"#.00000")
    Else
        txtGoServoPos.Text = Format(Val(txtServoPos.Text) - 0.00001,
"#.00000")
    End If
    btnGoServo_Click(sender, e)
End Sub
Private Sub btnServo20_Click(ByVal sender As System.Object, ByVal e As
System.EventArgs) Handles btnServo20.Click
    If optServoDown.Checked = True Then
        txtGoServoPos.Text = Format(Val(txtServoPos.Text) + 0.00002,
"#.00000")
    Else
        txtGoServoPos.Text = Format(Val(txtServoPos.Text) - 0.00002,
"#.00000")
    End If
    btnGoServo_Click(sender, e)
End Sub

'#####
Private Sub btnServo50_Click(ByVal sender As System.Object, ByVal e As
System.EventArgs) Handles btnServo50.Click
    If optServoDown.Checked = True Then
        txtGoServoPos.Text = Format(Val(txtServoPos.Text) + 0.00005,
"#.00000")
    Else
        txtGoServoPos.Text = Format(Val(txtServoPos.Text) - 0.00005,
"#.00000")
    End If
    btnGoServo_Click(sender, e)
End Sub

'#####
Private Sub btnServo100_Click(ByVal sender As System.Object, ByVal e As
System.EventArgs) Handles btnServo100.Click
    If optServoDown.Checked = True Then
        txtGoServoPos.Text = Format(Val(txtServoPos.Text) + 0.0001,
"#.00000")
    Else
        txtGoServoPos.Text = Format(Val(txtServoPos.Text) - 0.0001,
"#.00000")
    End If
    btnGoServo_Click(sender, e)
End Sub

'#####
Private Sub btnServo500_Click(ByVal sender As System.Object, ByVal e As
System.EventArgs) Handles btnServo500.Click
    If optServoDown.Checked = True Then
        txtGoServoPos.Text = Format(Val(txtServoPos.Text) + 0.0005,
"#.00000")
    Else
        txtGoServoPos.Text = Format(Val(txtServoPos.Text) - 0.0005,
"#.00000")
    End If
    btnGoServo_Click(sender, e)

```



```

End Sub

'#####
Private Sub btnServo1000_Click(ByVal sender As System.Object, ByVal e As
System.EventArgs) Handles btnServo1000.Click
    If optServoDown.Checked = True Then
        txtGoServoPos.Text = Format(Val(txtServoPos.Text) + 0.001,
"#.00000")
    Else
        txtGoServoPos.Text = Format(Val(txtServoPos.Text) - 0.001,
"#.00000")
    End If
    btnGoServo_Click(sender, e)
End Sub

'#####
Private Sub btnServo5000_Click(ByVal sender As System.Object, ByVal e As
System.EventArgs) Handles btnServo5000.Click
    If optServoDown.Checked = True Then
        txtGoServoPos.Text = Format(Val(txtServoPos.Text) + 0.005,
"#.00000")
    Else
        txtGoServoPos.Text = Format(Val(txtServoPos.Text) - 0.005,
"#.00000")
    End If
    btnGoServo_Click(sender, e)
End Sub

'#####
Private Sub btnServo10000_Click(ByVal sender As System.Object, ByVal e As
System.EventArgs) Handles btnServo10000.Click
    If optServoDown.Checked = True Then
        txtGoServoPos.Text = Format(Val(txtServoPos.Text) + 0.01,
"#.00000")
    Else
        txtGoServoPos.Text = Format(Val(txtServoPos.Text) - 0.01,
"#.00000")
    End If
    btnGoServo_Click(sender, e)
End Sub

'#####
Private Sub btnIncrementalApproach_Click(ByVal sender As System.Object, ByVal e
As System.EventArgs) Handles btnIncrementalApproach.Click
    If btnIncrementalApproach.Text = "Approach Target Incrementally" Then
        samplestate = 1
        btnGoServo.Enabled = False
        btnIncrementalApproach.Text = "Stop Incremental Approach"
    Else
        samplestate = 0
        btnGoServo.Enabled = True
        btnIncrementalApproach.Text = "Approach Target Incrementally"
    End If
End Sub

'#####
Private Sub onestep(ByVal newposition)
    SerialPort3.Write("1PA" + Format(newposition, "#.00000") + Chr(13) +
Chr(10))
End Sub

'#####

```

```

Private Sub SerialPort2_DataReceived(ByVal sender As System.Object, ByVal e As
System.IO.Ports.SerialDataReceivedEventArgs) Handles SerialPort2.DataReceived
    'capdata1 = SerialPort2.ReadByte() * 65536
    'capdata1 = capdata1 + SerialPort2.ReadByte() * 256
    'capdata1 = capdata1 + SerialPort2.ReadByte()
    'capdata2 = SerialPort2.ReadByte() * 65536
    'capdata2 = capdata2 + SerialPort2.ReadByte() * 256
    'capdata2 = capdata2 + SerialPort2.ReadByte()
    'pcbtemp = SerialPort2.ReadByte() * 256
    'pcbtemp = pcbtemp + SerialPort2.ReadByte()

    SerialPort2.ReadExisting()

    'txttopv.Text = Str(5 * capdata1 / 2 ^ 23 - 5)
    'txbtmv.Text = Str(5 * capdata2 / 2 ^ 23 - 5)
    'txttopnm.Text = Str(Convert.ToDouble(txttopv.Text) / 0.0004)
    'txbtmmn.Text = Str(Convert.ToDouble(txbtmv.Text) / 0.0004)

End Sub

'#####
Private Sub btnSetVolt_Click(ByVal sender As System.Object, ByVal e As
System.EventArgs) Handles btnSetVolt.Click
    ioLCR.WriteString("VOLT " & txtmv.Text & "mV" + Chr(10))
End Sub

'#####
Private Sub btnGetSpectraSet_Click(ByVal sender As System.Object, ByVal e As
System.EventArgs) Handles btnGetSpectraSet.Click
    If btnGetSpectraSet.Text = "Start Automated Spectrum Collection" Then
        getspectraSet = True
        btnGoServo.Enabled = False
        'btnGetSpectrum.Enabled = False
        btnGetSpectraSet.Text = "Stop Automated Spectrum Collection"
    Else
        getspectraSet = False
        btnGoServo.Enabled = True
        'btnGetSpectrum.Enabled = True
        btnGetSpectraSet.Text = "Start Automated Spectrum Collection"
    End If
End Sub

End Sub

'#####
Private Sub btnServoReset_Click(ByVal sender As System.Object, ByVal e As
System.EventArgs) Handles btnServoReset.Click
    SerialPort3.Write("1RS" + txtGoServoPos.Text + Chr(13) + Chr(10))
End Sub

'#####
Private Sub btnServoHome_Click(ByVal sender As System.Object, ByVal e As
System.EventArgs) Handles btnServoHome.Click
    SerialPort3.Write("1OR" + txtGoServoPos.Text + Chr(13) + Chr(10))
End Sub

'#####
Private Sub btnServoCmd_Click(ByVal sender As System.Object, ByVal e As
System.EventArgs) Handles btnServoCmd.Click
    SerialPort3.Write(txtServoCmd.Text + txtGoServoPos.Text + Chr(13) +
Chr(10))
End Sub

'#####

```

```

Private Sub btnGetSet1_Click(ByVal sender As System.Object, ByVal e As
System.EventArgs) Handles btnGetSet1.Click
    If btnGetSet1.Text = "Get Repeat Data Set" Then
        btnGetFreqSet.Enabled = False
        btnGetSet1.Text = "Stop Repetitive Data Collection"
        If Val(txtDataSetTotal.Text) < 1 Then
            txtDataSetTotal.Text = "1"
        End If
        txtDataSetRemaining.Text = txtDataSetTotal.Text
        txtGoServoPos.Text = txtRetraction.Text
        btnGoServo_Click(sender, e)
        repeatgetstate = 1
    ElseIf btnGetSet1.Text = "Stop Repetitive Data Collection" Then
        btnGetFreqSet.Enabled = True
        btnGetSet1.Text = "Get Repeat Data Set"
        repeatgetstate = 0
    End If
End Sub

'#####
Private Sub Timer2_Tick(ByVal sender As System.Object, ByVal e As
System.EventArgs) Handles Timer2.Tick
    Dim rt As Double
    Dim tempraw As Double
    digitalwriter.WriteSingleSamplePort(True, 0)
    tempraw = analogreader.ReadSingleSample()
    rt = (-7584.8 * tempraw - 125571.9528) / (1.8962 * tempraw - 25.846)
    txtTemp1.Text = Format$(1 / (0.00113 + 0.0002339 * Log(rt) +
0.00000008863 * (Log(rt)) ^ 3) - 273.15, "##.0")

    digitalwriter.WriteSingleSamplePort(True, 2)
    tempraw = analogreader.ReadSingleSample()
    rt = (-7584.8 * tempraw - 125571.9528) / (1.8962 * tempraw - 25.846)
    txtTemp2.Text = Format$(1 / (0.00113 + 0.0002339 * Log(rt) +
0.00000008863 * (Log(rt)) ^ 3) - 273.15, "##.0")

    digitalwriter.WriteSingleSamplePort(True, 4)
    tempraw = analogreader.ReadSingleSample()
    rt = (-7584.8 * tempraw - 125571.9528) / (1.8962 * tempraw - 25.846)
    txtTemp3.Text = Format$(1 / (0.00113 + 0.0002339 * Log(rt) +
0.00000008863 * (Log(rt)) ^ 3) - 273.15, "##.0")

    digitalwriter.WriteSingleSamplePort(True, 6)
    tempraw = analogreader.ReadSingleSample()
    rt = (-7584.8 * tempraw - 125571.9528) / (1.8962 * tempraw - 25.846)
    txtTemp4.Text = Format$(1 / (0.00113 + 0.0002339 * Log(rt) +
0.00000008863 * (Log(rt)) ^ 3) - 273.15, "##.0")

    If repeatgetstate > 0 Then
        If repeatgetstate = 1 And Val(txtServoPos.Text) =
Val(txtRetraction.Text) Then
            txtGoServoPos.Text = txtStart.Text
            btnGoServo_Click(sender, e)
            repeatgetstate = 2
        End If
        If repeatgetstate = 2 And Val(txtServoPos.Text) =
Val(txtStart.Text) Then
            btnRecord_Click(sender, e)
            txtGoServoPos.Text = txtEnd.Text
            btnIncrementalApproach_Click(sender, e)
            repeatgetstate = 3
        End If
    End If

```

```

        If repeatgetstate = 3 And (Val(txtServoPos.Text) = Val(txtEnd.Text)
Or (Val(txtCp.Text) > mincap)) Then
        btnIncrementalApproach_Click(sender, e)
        btnRecord_Click(sender, e)
        txtDataSetRemaining.Text = Str(Val(txtDataSetRemaining.Text) -
1)

        If Val(txtDataSetRemaining.Text) = 0 Then
            repeatgetstate = 0
            btnGetSet1_Click(sender, e)
        Else
            repeatgetstate = 1
        End If
        txtGoServoPos.Text = txtRetraction.Text
        btnGoServo_Click(sender, e)
    End If
End If
If freqgetstate > 0 Then
    If freqgetstate = 1 And Val(txtServoPos.Text) =
Val(txtRetraction.Text) Then
        txtGoServoPos.Text = txtStart.Text
        btnGoServo_Click(sender, e)
        freqgetstate = 2
    End If
    If freqgetstate = 2 And Val(txtServoPos.Text) = Val(txtStart.Text)
Then
        btnRecord_Click(sender, e)
        txtGoServoPos.Text = txtEnd.Text
        btnIncrementalApproach_Click(sender, e)
        freqgetstate = 3
    End If
    If freqgetstate = 3 And Val(txtServoPos.Text) = Val(txtEnd.Text)
Then
        btnIncrementalApproach_Click(sender, e)
        btnRecord_Click(sender, e)
        If Len(freqstr) > 1 Then
            txtFreq.Text = Mid(freqstr, 1, InStr(1, freqstr, Chr(13)) -
1)
            freqstr = Mid(freqstr, InStr(1, freqstr, Chr(13)) + 2,
Len(freqstr))
            btnSetFreq_Click(sender, e)
            freqgetstate = 1
            txtDataSetRemaining.Text = ">=1"
        Else
            freqgetstate = 0
            txtDataSetRemaining.Text = "0"
        End If
        txtGoServoPos.Text = txtRetraction.Text
        btnGoServo_Click(sender, e)
    End If
End If

    If ampgetstate > 0 Then
        If ampgetstate = 1 And Val(txtServoPos.Text) =
Val(txtRetraction.Text) Then
            txtGoServoPos.Text = txtStart.Text
            btnGoServo_Click(sender, e)
            ampgetstate = 2
        End If
        If ampgetstate = 2 And Val(txtServoPos.Text) = Val(txtStart.Text)
Then
            btnRecord_Click(sender, e)
            txtGoServoPos.Text = txtEnd.Text
            btnIncrementalApproach_Click(sender, e)

```

```

        ampgetstate = 3
    End If
    If ampgetstate = 3 And Val(txtServoPos.Text) = Val(txtEnd.Text)
Then
        btnIncrementalApproach_Click(sender, e)
        btnRecord_Click(sender, e)
        If Len(ampstr) > 1 Then
            txtmv.Text = Mid(ampstr, 1, InStr(1, ampstr, Chr(13)) - 1)
            ampstr = Mid(ampstr, InStr(1, ampstr, Chr(13)) + 2,
Len(ampstr))

            btnSetVolt_Click(sender, e)
            ampgetstate = 1
            txtDataSetRemaining.Text = ">=1"
        Else
            ampgetstate = 0
            txtDataSetRemaining.Text = "0"
        End If
        txtGoServoPos.Text = txtRetraction.Text
        btnGoServo_Click(sender, e)
    End If
End If

    If biasgetstate > 0 Then
        If biasgetstate = 1 And Val(txtServoPos.Text) =
Val(txtRetraction.Text) Then
            txtGoServoPos.Text = txtStart.Text
            btnGoServo_Click(sender, e)
            biasgetstate = 2
        End If
        If biasgetstate = 2 And Val(txtServoPos.Text) = Val(txtStart.Text)
Then
            btnRecord_Click(sender, e)
            txtGoServoPos.Text = txtEnd.Text
            btnIncrementalApproach_Click(sender, e)
            biasgetstate = 3
        End If
        If biasgetstate = 3 And Val(txtServoPos.Text) = Val(txtEnd.Text)
Then
            btnIncrementalApproach_Click(sender, e)
            btnRecord_Click(sender, e)
            If Len(biasstr) > 1 Then
                txtbiasmv.Text = Mid(biasstr, 1, InStr(1, biasstr, Chr(13))
- 1)
                biasstr = Mid(biasstr, InStr(1, biasstr, Chr(13)) + 2,
Len(biasstr))

                btnsetbias_Click(sender, e)
                biasgetstate = 1
                txtDataSetRemaining.Text = ">=1"
            Else
                biasgetstate = 0
                txtDataSetRemaining.Text = "0"
            End If
            txtGoServoPos.Text = txtRetraction.Text
            btnGoServo_Click(sender, e)
        End If
    End If
End Sub

'#####
Private Sub btnGetFreqSet_Click(ByVal sender As System.Object, ByVal e As
System.EventArgs) Handles btnGetFreqSet.Click
    If btnGetFreqSet.Text = "Get Frequency Data Set" Then
        btnGetSet1.Enabled = False
    End If
End Sub

```

```

        btnGetFreqSet.Text = "Stop Frequency Data Collection"
    Try
        freqstr =
My.Computer.FileSystem.ReadAllText(txtFreqFilename.Text)
        freqgetstate = 1
    Catch ex As Exception
        MessageBox.Show(ex.Message)
        freqgetstate = 0
    End Try
    If freqgetstate Then
        txtFreq.Text = Mid(freqstr, 1, InStr(1, freqstr, Chr(13)) - 1)
        freqstr = Mid(freqstr, InStr(1, freqstr, Chr(13)) + 2,
Len(freqstr))
        btnSetFreq_Click(sender, e)
    End If
ElseIf btnGetfreqSet.Text = "Stop Frequency Data Collection" Then
    btnGetSet1.Enabled = True
    btnGetFreqSet.Text = "Get Frequency Data Set"
    freqgetstate = 0
End If

End Sub

'#####
Private Sub btnGetAmpSet_Click(ByVal sender As System.Object, ByVal e As
System.EventArgs) Handles btnGetAmpSet.Click
    If btnGetAmpSet.Text = "Get Amplitude Data Set" Then
        btnGetSet1.Enabled = False
        btnGetFreqSet.Enabled = False
        btnGetAmpSet.Text = "Stop Amplitude Data Collection"
    Try
        ampstr =
My.Computer.FileSystem.ReadAllText(txtFreqFilename.Text)
        ampgetstate = 1
    Catch ex As Exception
        MessageBox.Show(ex.Message)
        ampgetstate = 0
    End Try
    If ampgetstate Then
        txtmv.Text = Mid(ampstr, 1, InStr(1, ampstr, Chr(13)) - 1)
        ampstr = Mid(ampstr, InStr(1, ampstr, Chr(13)) + 2,
Len(ampstr))
        btnSetVolt_Click(sender, e)
    End If
ElseIf btnGetAmpSet.Text = "Stop Amplitude Data Collection" Then
    btnGetSet1.Enabled = True
    btnGetFreqSet.Enabled = True
    btnGetAmpSet.Text = "Get Amplitude Data Set"
    ampgetstate = 0
End If

End Sub

'#####
Private Sub btnsetbias_Click(ByVal sender As System.Object, ByVal e As
System.EventArgs) Handles btnsetbias.Click
    If Val(txtbiasmv.Text) = 0 Then
        ioLCR.WriteString("BIAS:VOLT 0mv" & Chr(10))
        ioLCR.WriteString("BIAS:STATE off" & Chr(10))
    Else
        ioLCR.WriteString("BIAS:VOLT " & txtbiasmv.Text & "mV" + Chr(10))
        ioLCR.WriteString("BIAS:STATE on" & Chr(10))
    End If

End Sub

```

```

'#####
Private Sub btnGetBiasSet_Click(ByVal sender As System.Object, ByVal e As
System.EventArgs) Handles btnGetBiasSet.Click
    If btnGetBiasSet.Text = "Get Bias Data Set" Then
        btnGetSet1.Enabled = False
        btnGetFreqSet.Enabled = False
        btnGetAmpSet.Enabled = False
        btnGetBiasSet.Text = "Stop Bias Data Collection"
        Try
            biasstr =
My.Computer.FileSystem.ReadAllText(txtFreqFilename.Text)
            biasgetstate = 1
        Catch ex As Exception
            MessageBox.Show(ex.Message)
            biasgetstate = 0
        End Try
        If biasgetstate Then
            txtbiasmv.Text = Mid(biasstr, 1, InStr(1, biasstr, Chr(13)) -
1)
            biasstr = Mid(biasstr, InStr(1, biasstr, Chr(13)) + 2,
Len(biasstr))
            btnsetbias_Click(sender, e)
        End If
    ElseIf btnGetBiasSet.Text = "Stop Bias Data Collection" Then
        btnGetSet1.Enabled = True
        btnGetFreqSet.Enabled = True
        btnGetAmpSet.Enabled = True
        btnGetBiasSet.Text = "Get Bias Data Set"
        biasgetstate = 0
    End If
End Sub
End Class

```